1-1-2014

Assembly, Structure, and Reactivity of Cu_4S and Cu_3S Models for the Nitrous Oxide Reductase Active Site, Cu_Z*

Brittany J. Johnson
University of Illinois at Chicago

Sergey V. Lindeman
Marquette University, sergey.lindeman@marquette.edu

Neal P. Mankad
University of Illinois at Chicago

Accepted version. *Inorganic Chemistry,* Vol. 53, No. 19 (2014): 10611-10619. DOI.

Assembly, Structure, and Reactivity of Cu_4S and Cu_3S Models for the Nitrous Oxide Reductase Active Site, Cu_Z*

Brittany J. Johnson
Department of Chemistry, University of Illinois at Chicago, Chicago, IL
Sergey V. Lindeman
Department of Chemistry, Marquette University, Milwaukee, WI
Neal P. Mankad
Department of Chemistry, University of Illinois at Chicago, Chicago, IL

Synopsis: The properties of bioinspired copper sulfide clusters were tuned using bridging diphosphines.

Inorganic Chemistry, Vol 53, No. 19 (2014): pg. 10611-10619. DOI.

Abstract

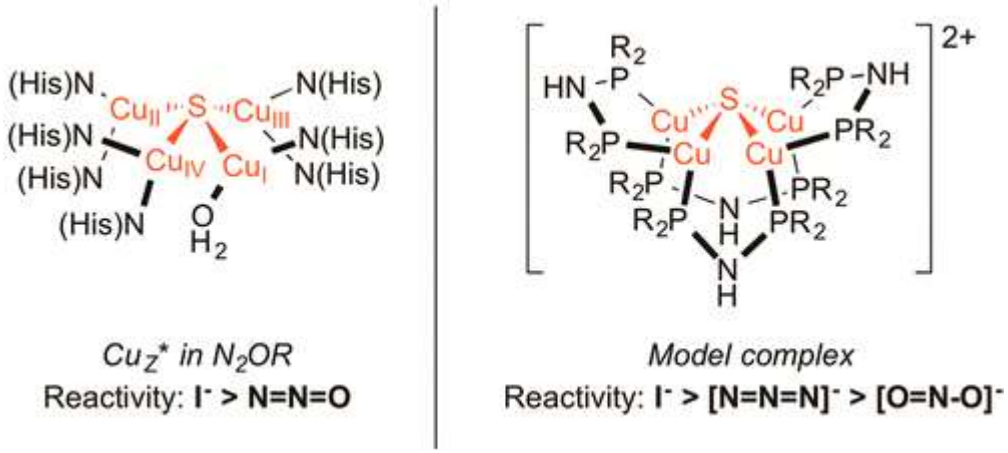

Bridging diphosphine ligands were used to facilitate the assembly of copper clusters with single sulfur atom bridges that model the structure of the Cu_Z* active site of nitrous oxide reductase. Using bis(diphenylphosphino)amine (dppa), a [Cu^I_4(μ_4-S)] cluster with N–H hydrogen bond donors in the secondary coordination sphere was assembled. Solvent and anion guests were found docking to the N–H sites in the solid state and in the solution phase, highlighting a kinetically viable pathway for substrate introduction to the inorganic core. Using bis(dicyclohexylphosphino)methane (dcpm), a [Cu^I_3(μ_3-S)] cluster was assembled preferentially. Both complexes exhibited reversible oxidation events in their cyclic voltammograms, making them functionally relevant to the Cu_Z* active site that is capable of catalyzing a multielectron redox transformation, unlike the previously known [Cu^I_4(μ_4-S)] complex from Yam and co-workers supported by bis(diphenylphosphino)methane (dppm). The dppa-supported [Cu^I_4(μ_4-S)] cluster reacted with N_3^-, a linear triatomic substrate isoelectronic to N_2O, in preference to NO_2^-, a bent triatomic. This [Cu^I_4(μ_4-S)] cluster also bound I^-, a known inhibitor of Cu_Z*. Consistent with previous observations for nitrous oxide reductase, the tetracopper model complex bound the I^- inhibitor much more strongly and rapidly than the substrate isoelectronic to N_2O, producing unreactive μ_3-iodide clusters including a [Cu_3(μ_3-S)(μ_3-I)] complex related to the [Cu_4(μ_4-S)(μ_2-I)] form of the inhibited enzyme.

Introduction

Nitrous oxide (N_2O), a potent greenhouse gas and ozone layer depletion agent, is consumed in nature by nitrous oxide reductase (N_2OR) during bacterial denitrification.[1] N_2O activation and reduction occurs at a tetracopper sulfide active site within N_2OR, whose workings remain unclear. Two forms of this cluster have been characterized (Scheme 1a): one with a [Cu_4(μ_4-S)] stoichiometry called Cu_Z*[2] and

Inorganic Chemistry, Vol 53, No. 19 (2014): pg. 10611-10619. DOI.

one with a $[Cu_4(\mu_4\text{-}S)(\mu_2\text{-}S)]$ stoichiometry called Cu_Z.[3] Although both Cu_Z* and Cu_Z have been proposed as the active form in nature, recent studies indicate that only Cu_Z* in its Cu^I_4 oxidation state is kinetically competent to mediate the two-electron reduction of N_2O under catalytically relevant conditions.[4] However, little is known about the intimate workings of Cu_Z* outside of computational studies,[5] and studies on the enzyme itself are complicated by the fact that purified N_2OR invariably contains mixtures of Cu_Z and Cu_Z*.[4] As a result, spectroscopic data on the active, fully reduced Cu_Z* are largely absent despite copious available data on other Cu_Z* oxidation states.[1,4] Inorganic model studies could, in principle, lend further understanding from experimental data related to cluster assembly, redox behavior, spectroscopic features, and chemical reactivity and mechanism. However, such studies are hindered by the fact that the structural motif present in Cu_Z* is unique in synthetic coordination chemistry. The only $[Cu_xS_y]$ cluster ever reported to exhibit N_2O reactivity does not reproduce the $[Cu_4S_1]$ stoichiometry in Cu_Z*,[6] limiting the insight that can be gained. In fact, not only do complexes with $[Cu_4(\mu_4\text{-}S)]$ cores have almost no precedent, but more generally the rational construction of copper-containing clusters with *single* sulfur atom bridges remains a synthetic challenge.[7] Much more common is the construction of copper clusters bridged by *multiple* sulfur atoms, for example, with $[Cu_3S_2]$, $[Cu_{12}S_6]$, $[Cu_{13}S_2]$, or $[Cu_{20}S_{10}]$ cores, that bear little resemblance to Cu_Z* or other bioinorganic active sites.[8,9]

Inorganic Chemistry, Vol 53, No. 19 (2014): pg. 10611-10619. DOI.

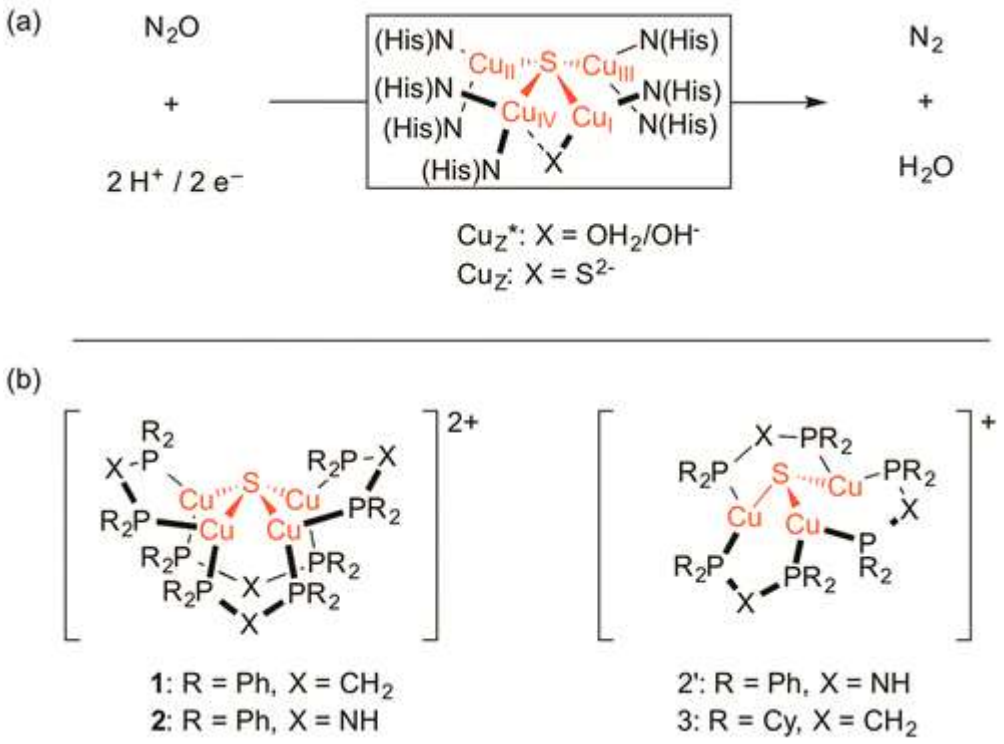

Scheme 1. (a) N_2O Reduction by Bioinorganic Copper Sulfide Clusters Cu_Z* and/or Cu_Z (His = Histidine) and (b) Synthetic Copper Sulfide Clusters Discussed in This Report

The complex $[(\mu_2\text{-dppm})_4Cu_4(\mu_4\text{-S})]^{2+}$ [**1**; dppm = bis(diphenylphosphino)methane; see Scheme 1] represents the only known example of a synthetic $[Cu_4(\mu_4\text{-S})]$ cluster prior to this report.[10] This complex has been studied in great detail for its optical properties but is limited in its ability to serve as a functional model for Cu_Z*.[11] Not only is air-stable **1** relatively inert in nature, but also it does not exhibit the reversible electrochemistry necessary to model a bioinorganic active site, such as Cu_Z*, that mediates a multielectron redox transformation. Some of these drawbacks in the ability of **1** to model Cu_Z* may stem from its use of phosphorus donors, as opposed to the nitrogen donors of Cu_Z*, to stabilize the $[Cu_4(\mu_4\text{-S})]$ core. However, spectroscopic and computational analyses of Cu_Z* indicate that its redox-active molecular orbital is largely localized (83%) on the four copper centers and the bridging sulfur,[12] implying that the supporting nitrogen donors are limited in their orbital contributions to chemically relevant frontier orbitals. Computational analysis of **1** has similarly indicated that its redox-active molecular orbital is largely localized (84%) on the four copper centers and bridging sulfur.[13]

Inorganic Chemistry, Vol 53, No. 19 (2014): pg. 10611-10619. DOI.

Because of these similar electronic structures as well as the demonstrated, unique ability of dppm to control the Cu:S stoichiometry, we deemed that derivatives of complex **1** merited further examination.

Fortunately, the bridging diphosphine ligands in use for constructing **1** are readily tuned to overcome these kinetic and thermodynamic shortcomings. In this contribution, we report the synthesis and characterization of new copper monosulfide clusters ($[(\mu_2\text{-dppa})_4Cu_4(\mu_4\text{-S})][PF_6]_2$ (**2**) and $[(\mu_2\text{-dcpm})_3Cu_3(\mu_3\text{-S})][PF_6]\cdot OCMe_2$ (**3**); see Scheme 1) that assemble to model structural features relevant to the $[Cu_4S]$ core of Cu_Z*, including the presence of hydrogen-bond donors in the secondary coordination sphere. These complexes also exhibit reversible electrochemistry, and one (**2**) also presents chemical reactivity toward a substrate that is isoelectronic to N_2O, azide (N_3^-), and toward a known inhibitor of the N_2OR enzyme, iodide (I^-). Competition experiments reveal that the linear triatomic, N_3^-, binds more rapidly than a bent triatomic, nitrite (NO_2^-), but much less rapidly than the enzyme inhibitor, I^-.

Results and Discussion

Cluster Assembly and Structure

One design strategy we chose to pursue involved modifying dppm-supported **1** to include hydrogen-bond donors in the secondary coordination sphere. It is well recognized that secondary-sphere hydrogen-bonding interactions are crucial to the design of functional models of metalloenzymes.[14] Building such a model for Cu_Z* could, in principle, provide kinetically viable pathways for the introduction of substrates to the inorganic $[Cu_4(\mu_4\text{-S})]$ core. Indeed, for N_2OR itself, it is thought that hydrogen bonding from the N–H groups of lysine and histidine residues located nearby to the Cu_Z* cluster may assist in N_2O binding and subsequent N_2 extrusion.[5,15] In order to construct a copper sulfide cluster with hydrogen-bond donors, we targeted the use of bis(diphenylphosphino)amine (dppa) in place of dppm. The second strategy we chose to pursue involved modifying **1** to render the copper sulfide core more electron-rich, with the goal of stabilizing higher oxidation states and thereby obtaining reversible electrochemistry. In

Inorganic Chemistry, Vol 53, No. 19 (2014): pg. 10611-10619. DOI.

order to construct a more electron-rich copper sulfide cluster, we targeted the use of bis(dicyclohexylphosphino)methane (dcpm) in place of dppm.

The slow addition of a methanolic solution of Na_2S (0.5 equiv) to an acetone solution of colorless $[(\mu_2\text{-dppa})_2Cu_2(NCCH_3)_2][PF_6]_2$[16] produced a rapid color change to bright orange. Slow diffusion of diethyl ether vapors into the acetone solution produced **2** as pale-orange plates. Combustion analysis of these plates, upon crushing and drying, was consistent with the dicationic tetracopper formulation. X-ray diffraction analysis of one of the plates confirmed the assembly of a $[Cu_4(\mu_4\text{-S})]$ core stabilized by four bridging dppa ligands, along with the presence of two PF_6^- counterions per tetracopper cluster. Additionally, we believe that a minor fraction of the product mixture was the tricopper species $[(\mu_2\text{-dppa})_3Cu_3(\mu_3\text{-S})][PF_6]$ (**2'**) because a single crystal of that species also was identified among the sample and analyzed by X-ray diffraction (see Figures S44 and S45 in the Supporting Information, SI). However, no spectroscopic evidence for the formation of **2'** was obtained, indicating that it is formed only in trace amounts under these reaction conditions.

The core structure of **2** is shown in Figure 1a. Unlike **1**, which features a relatively symmetric $[Cu_4(\mu_4\text{-S})]$ core [neighboring Cu···Cu distances of 2.869(1)–3.129(1) Å],[10] the inorganic core of **2** is asymmetric. While three of the copper centers in **2** are close together [Cu(1)···Cu(2), 2.6571(7) Å; Cu(2)···Cu(3), 2.7184(4) Å], a fourth copper center is significantly displaced from the others [Cu(4)···Cu(1), 3.1005(5) Å; Cu(4)···Cu(3), 3.5365(6) Å]. Two acetone solvent molecules and a PF_6^- anion engage in hydrogen bonding with N–H groups in the secondary coordination sphere. The two acetone molecules are associated with the N–H residues of the two bridging dppa ligands directly bound to Cu(4), in essence "pulling" Cu(4) away from the rest of the cluster (Figure 1a). Such a phenomenon is impossible for **1**, which lacks any hydrogen-bond donors. Similar hydrogen-bonding motifs have been noted for $[(\mu_2\text{-dppa})_3Cu_3(\mu_3\text{-SH})_2][BF_4]$.[17] The environment of the sulfur center in **2** is best described as a seesaw shape (τ_4 = 0.64).[18]

Inorganic Chemistry, Vol 53, No. 19 (2014): pg. 10611-10619. DOI.

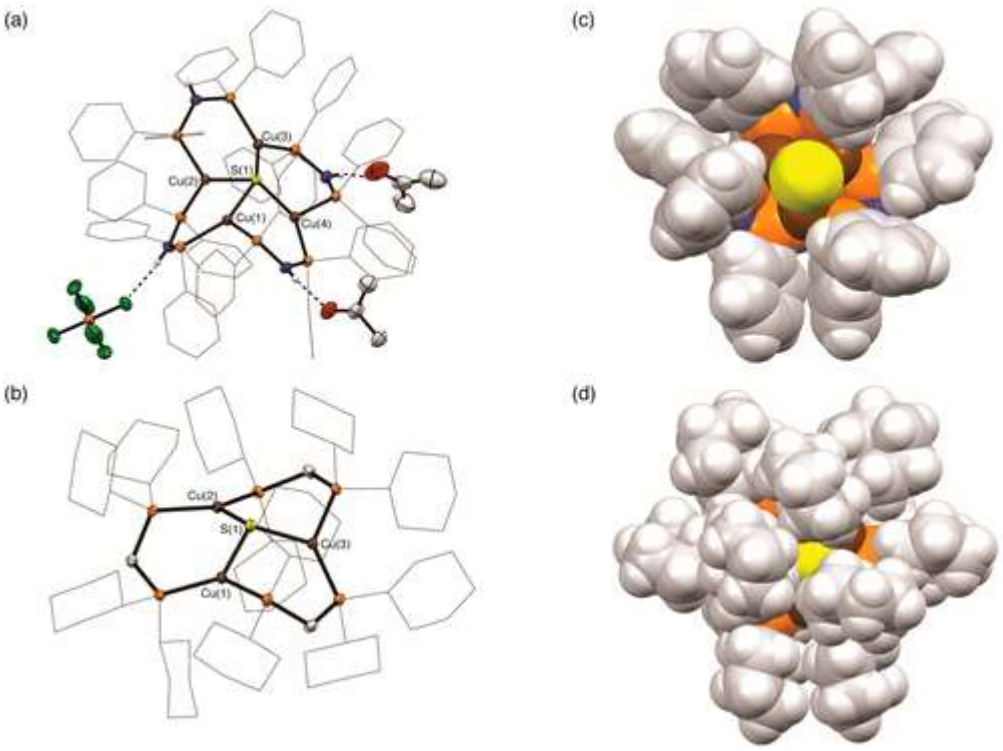

Figure 1. Solid-state structures of (a) **2**·2OCMe$_2$ and (b) **3** determined by X-ray crystallography. Core atoms are shown as 50% probability ellipsoids, phosphine substituents are shown as wireframes, and C–H hydrogen atoms have been omitted for clarity. Cocrystallized anions and solvent molecules are shown only if engaged in hydrogen bonding to the cationic unit. N–H hydrogen atoms are shown in calculated positions. Space-filling models of the cationic portions of (c) **2'** and (d) **3**, both based on crystallographically determined coordinates and viewed down the sulfur (pseudo-)C_3 axis, with all hydrogen atoms shown in calculated positions. Atom colors: C, gray; H, white; Cu, brown; F, green; N, blue; O, red; P, orange; S, yellow.

The structural parameters within the [Cu$_4$(μ_4-S)] cores of Cu$_Z$*, Cu$_Z$, **1**, and **2** are compared in Table 1. The distorted core in **2** accesses a relatively large span of Cu···Cu distances, making it the most accurate model of the distorted core in Cu$_Z$* reported to date. As judged by τ_4 values, the μ_4-sulfide ligands in all of the tetracopper clusters have seesaw geometries, with the τ_4 values for **1** and **2** more closely matching Cu$_Z$* than Cu$_Z$. These τ_4 values further confirm that **2** contains a more structurally faithful inorganic core model of Cu$_Z$* at the sulfur bridge, which may play an important role in N_2O docking in N_2OR.[5]

Inorganic Chemistry, Vol 53, No. 19 (2014): pg. 10611-10619. DOI.

Table 1. Structural Comparisons of Cu_Z*, Cu_Z, **1**, and **2**

parameter	Cu_Z*[a]	Cu_Z[b]	1[c]	2
Cu···Cu (Å)	2.54[d]	2.83[d]	2.869(2)[d]	2.6571(7)[d]
	2.56[d]	2.84[d]	2.869(2)[d]	2.7184(4)[d]
	3.00[d]	2.95[d]	3.128(1)[d]	3.1005(5)[d]
	3.33[d]	3.38[d]	3.128(1)[d]	3.5365(6)[d]
	3.36[e]	3.41[e]	4.169(2)[e]	3.9697(6)[e]
	4.43[e]	4.60[e]	4.303(1)[e]	4.2857(6)[e]
Cu–μ_4-S (Å)	2.09	2.19	2.267(1)	2.2452(6)
	2.16	2.22	2.267(1)	2.2619(8)
	2.21	2.35	2.269(2)	2.2418(7)
	2.25	2.44	2.269(2)	2.2217(8)
τ_4[f]	0.66	0.71	0.59	0.64

[a]From analysis of the coordinates from PDB accession code 1QNI. See ref 2.
[b]From analysis of the coordinates from PDB accession code 3SBR. See ref 3.
[c]Duplicate values from crystallographic symmetry equivalence. See ref 10.
[d]Neighboring Cu···Cu distance.
[e]Cross-cluster Cu···Cu distance.
[f]τ_4 value of the μ_4-sulfur. See ref 18.

In addition to the hydrogen-bonding interactions observed in the solid-state structure of **2**, they appear to be present in the solution phase, as well. First, solutions of **2** are air-sensitive, unlike solutions of **1**, which may imply that the N–H groups play a role in transporting O_2 from air to the [Cu_4(μ_4-S)] core of **2**.[19] Second, the ^{31}P NMR spectra of **2** were highly solvent-dependent. A sample of **2** that had been synthesized in and crystallized from acetone, and therefore was expected to have acetone guests docked to the ligand periphery, exhibited a single broad ^{31}P NMR resonance in acetone-d_6 at 36.6 ppm. Dissolving the same sample in acetonitrile-d_3 resulted in two sharper ^{31}P NMR resonances at 36.8 and 36.5 ppm, respectively. Thinking that the 36.8-ppm signal corresponded to a species where acetone guest molecules had been displaced by acetonitrile guest molecules, we then conducted the synthesis and precipitation of **2** in acetonitrile. Analyzing this sample in acetonitrile-d_3 revealed a single sharp ^{31}P NMR resonance at 36.8 ppm. A similar phenomenon was observed with dimethyl sulfoxide-d_6. Collectively, these data (Figure 2) provide clear evidence that the docking of solvent molecules to the periphery of **2** via hydrogen bonding is a phenomenon that exists in the solution phase and that exchange of the guest molecules can occur at ambient conditions.

Inorganic Chemistry, Vol 53, No. 19 (2014): pg. 10611-10619. DOI.

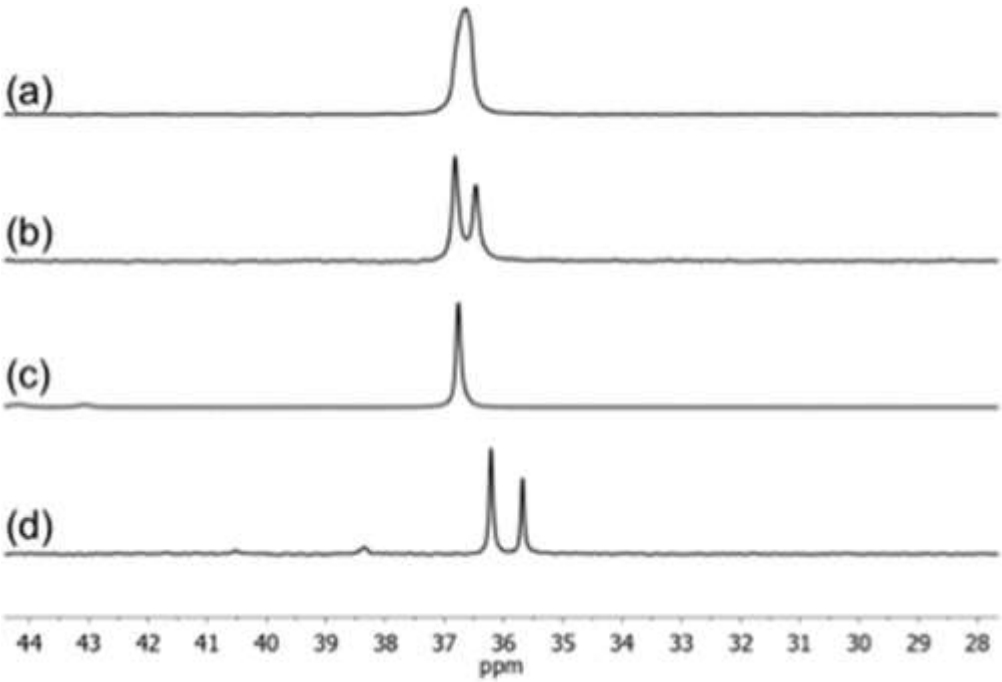

Figure 2. ^{31}P NMR spectra of **2** in (a) acetone-d_6 after preparation in acetone, (b) acetonitrile-d_3 after preparation in acetone, (c) acetonitrile-d_3 after preparation in acetonitrile, and (d) dimethyl sulfoxide-d_6 after preparation in acetone.

The addition of Na_2S (0.5 equiv) to $[(\mu_2\text{-dcpm})_2Cu_2][PF_6]_2$[20] resulted in incomplete conversion to a new species, as judged by NMR spectroscopy. Complete conversion to the new species only was attained when 0.67 equiv of Na_2S was used. Consistent with this stoichiometry, crystallization of the product by slow diffusion of diethyl ether vapors into an acetone solution provided pale-yellow crystals of **3**. X-ray diffraction analysis confirmed the monocationic tricopper formulation and revealed a $[Cu_3(\mu_3\text{-S})]$ core that has limited precedent in the literature (Figure 1b).[7a,7b] Presumably, the bulkier cyclohexyl substituents preclude the formation of a tetracopper cluster and preferentially direct the assembly of a tricopper core in order to ease steric congestion. Accordingly, the Cu···Cu distances in **3** [3.5684(3)–3.6753(3) Å] are significantly longer than those in **1** and **2**. Parts c and d of Figure 1 compare space-filling models of $[Cu_3S]$ complexes **2'** and **3**, further highlighting the increased steric congestion imparted by dcpm. The geometry of the sulfur center in **3** is trigonal-pyramidal with approximate C_3 symmetry [Cu–S–Cu angles: 107.61(2)–111.78(2)°]. Complex **3** complements the recent characterization of a $[Cu_3(\mu_3\text{-S})]$ cluster by Murray and co-workers,[7a] which features a planar rather than pyramidal S^{2-} ligand and was characterized in

Inorganic Chemistry, Vol 53, No. 19 (2014): pg. 10611-10619. DOI.

higher oxidation states ($Cu^{II}Cu^{II}Cu^{I}$ and $Cu^{II}Cu^{I}Cu^{I}$) than **3** ($Cu^{I}Cu^{I}Cu^{I}$), possibly because of the use of hard nitrogen ligands instead of soft phosphorus ligands to support the cluster.

Electrochemical and Photophysical Characterization

The N_2OR enzyme catalyzes a multielectron redox transformation, implying that the Cu_Z* active site can stabilize multiple redox states. Accordingly, any functional model of Cu_Z* should exhibit reversible electrochemical behavior. The dppm complex, **1**, was reported previously to have three ill-defined, irreversible oxidation events with onset at 0.27 V versus $[FeCp_2]^{+/0}$.[10] Analysis of the dppa analogue, **2**, instead revealed a reversible oxidation event by cyclic voltammetry (CV), cathodically shifted to −0.12 V (Figure 3a), followed by three ill-defined, irreversible oxidation events (Table 2 and Figure S1 in the SI). The significant cathodic shift resulting from substituting dppm with the more strongly donating dppa is well precedented in various coordination complexes.[21] The dcpm analogue, **3**, also exhibited a fully reversible oxidation event in its CV, further cathodically shifted to −0.35 V (Figure 3b), followed by three irreversible oxidations (Table 2 and Figure S4 in the SI). Assuming that each copper center can access the Cu^{I} and Cu^{II} states only, the presence of four oxidation events for the tricopper complex, **3**, implies that the μ_3-S^{2-} ligand also participates in oxidation chemistry. Such noninnocent behavior of bridging sulfur atoms is well documented through spectroscopic and computational analyses of dicopper complexes with bridging $[(S)_2]^{n-}$ units.[22] For comparison to the data reported here, a lower limit can be placed on the $Cu^{II}Cu^{I}_3/Cu^{I}_4$ potential of Cu_Z* based on the fact that methyl viologen is required to access the fully reduced state.[4] Using the reduction potential of methyl viologen[23] as a lower limit and converting from the SCE scale to the $[FeCp_2]^{+/0}$ scale using the method of Pavlishchuk and Addison,[24] we estimated the reduction potential of Cu_Z* as $E^0 > -0.78$ V versus $[FeCp_2]^{+/0}$.[25] While the precise reduction potential for Cu_Z* is not known, the model complexes in this work also fall above this lower limit.

Inorganic Chemistry, Vol 53, No. 19 (2014): pg. 10611-10619. DOI.

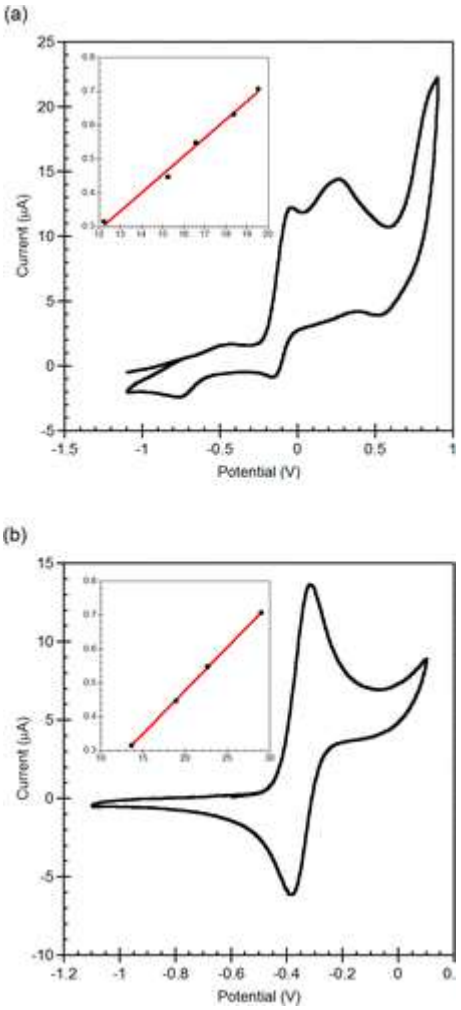

Figure 3. Cyclic voltammograms of (a) **2** and (b) **3** in CH_3CN (0.1 M Bu_4NPF_6, 100 mV s^{-1} scan rate, Pt working electrode). Potentials are referenced to $[FeCp_2]^{+/0}$. Insets: Plots of the square root of the scan rate (V s^{-1}) versus current (μA) in the forward direction for the first oxidations. The linear dependence indicates reversible electrochemical behavior (R^2 = 0.99614 and 0.99993, respectively).

Table 2. Electrochemical and Photophysical Properties of **1**–**3**

property	1[a]	2	3
$E_{oxidation}$ (V)[b]	0.27, 1.25, 1.39	–0.12 (rev.),[c] 0.27, 0.88, 1.55	–0.35 (rev.),[c] 0.29, 0.86, 1.58
$\lambda_{emission}$ (nm)[d]	618	704	642
Φ[e]	0.22	0.067	0.0007

[a]From ref 10.
[b]Referenced to $[FeCp_2]^{+/0}$, from CV in CH_3CN (0.1 M $[Bu_4N][PF_6]$, Pt working electrode, and 100 mV s^{-1} scan rate).
[c]Reversible.
[d]Emission measured with an excitation wavelength of 415 nm in CH_3CN at room temperature.

Inorganic Chemistry, Vol 53, No. 19 (2014): pg. 10611-10619. DOI.

[e]Quantum yield measured with an excitation wavelength of 415 nm in CH_3CN at room temperature for all compounds.

In light of the noteworthy photophysical properties previously noted for **1**,[10] we examined the photophysical characteristics of **2** and **3** for comparison. The lowest-energy absorption of **1** is at 285 nm, a feature that shifts to 284 nm for **2** and 279 nm for **3**.[26] As expected, these fully reduced complexes lack any low-energy absorption in the 450–550 nm range observed for the resting, one-hole states of Cu_Z* and Cu_Z.[1] Like **1**, both **2** and **3** are luminescent and glow orange upon excitation. The emission wavelengths and quantum yields were ligand-dependent (Table 2). The quantum yield measured for **3** was significantly lower than those of **1** and **2**, indicating a special ability of the [$Cu_4(\mu_4$-S)] motif to support efficient excited-state chemistry and bright emission.

Reactivity toward N_3^- and I^-

N_2O is notoriously inert toward inorganic systems. Very few transition-metal coordination complexes react with gaseous N_2O,[27] and fewer still of these systems also contain copper, a metal of low azo- and oxophilicity.[6,28] Accordingly, we have not observed any evidence by spectroscopic methods for reactivity between N_2O and **1**, **2**, or **3** under the reaction conditions we have screened thus far. However, we hypothesized that relevant reactivity would be observed with other triatomic substrates that, while closely related to N_2O in electronic structure, possess overall anionic charge. Particularly fascinating to us were azide (N_3^-), which is a linear triatomic anion, and nitrite (NO_2^-), which is a bent triatomic anion. Although N_2O is a linear triatomic molecule in its ground state, computational studies have suggested that significant N–N–O bending is observed during its binding to the Cu_Z* cluster in N_2OR.[5] In this regard, N_3^- resembles the ground-state geometry of N_2O, while NO_2^- resembles the transition state structure proposed for N_2O binding to Cu_Z*. We also chose to examine the chemistry of our model system **2** with iodide (I^-), a known inhibitor of N_2OR.[29]

Complex **2** reacted readily with excess NaN_3 at room temperature, producing a mixture of two complexes that were both identified crystallographically (Scheme 2). One of the products was the

Inorganic Chemistry, Vol 53, No. 19 (2014): pg. 10611-10619. DOI.

$[Cu_3(\mu_3\text{-}S)]$ complex, **2'**, and the second product was $[(\mu_2\text{-}dppa)_3Cu_3(\mu_3\text{-}N_3)_2][PF_6]$ (**4**). Because of their similar solubility properties, we were not able to separate **2'** and **4**, which were produced in a ratio of 2.7:1 in the crude reaction mixture (Figures S22 and S23 in the SI). However, **4** was produced as the major copper-containing product from the reaction between **2** and N_3SiMe_3; this method provided us with pure samples of **4** for full characterization (Figures S24–S26 in the SI). The IR spectrum of **4** featured a characteristic azide vibration at 2046 cm^{-1}, shifted from 2103 cm^{-1} in NaN_3. The solid-state structure of **4** (Figure 4) featured three tetrahydrofuran (THF) molecules (the solvent of crystallization) bound to each of the three N–H groups in the secondary coordination sphere. The cationic portion of **4** possessed approximate C_3 symmetry, with the N_3 units deviating slightly from the C_3 axis. The end-on, μ_3 binding of N_3^- to the multicopper cluster contrasts with the proposed side-on binding of N_2O to Cu_Z*.[5] Under the same reaction conditions, $NaNO_2$ did not react with **2**.

Inorganic Chemistry, Vol 53, No. 19 (2014): pg. 10611-10619. DOI.

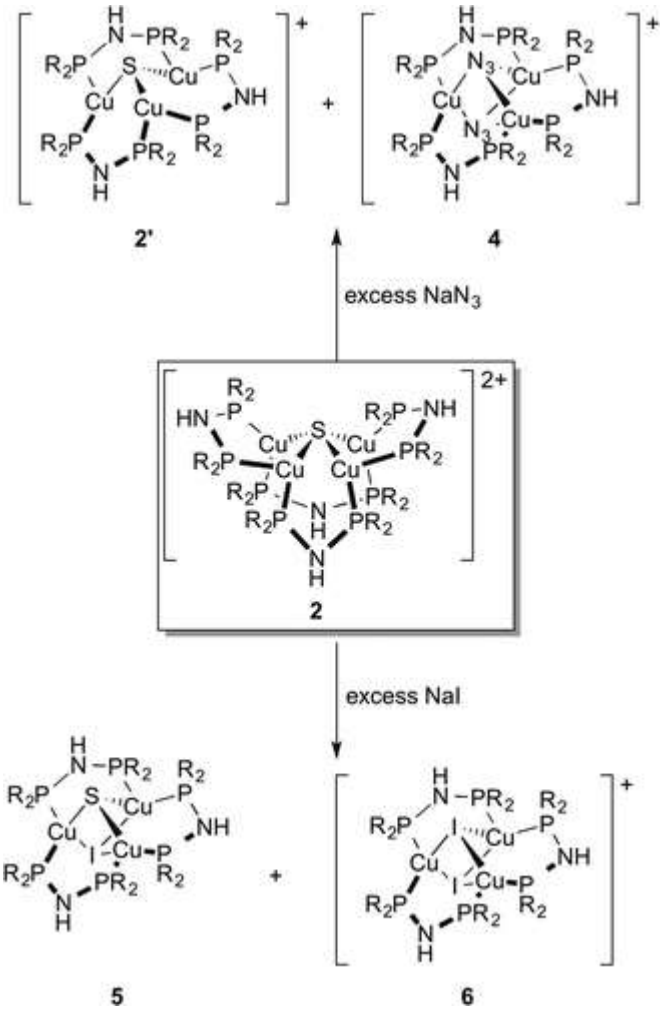

Scheme 2. Reactivity of the $[Cu^{I}_4(\mu_4\text{-}S)]$ Cluster **2** with NaN_3 and NaI

Inorganic Chemistry, Vol 53, No. 19 (2014): pg. 10611-10619. DOI.

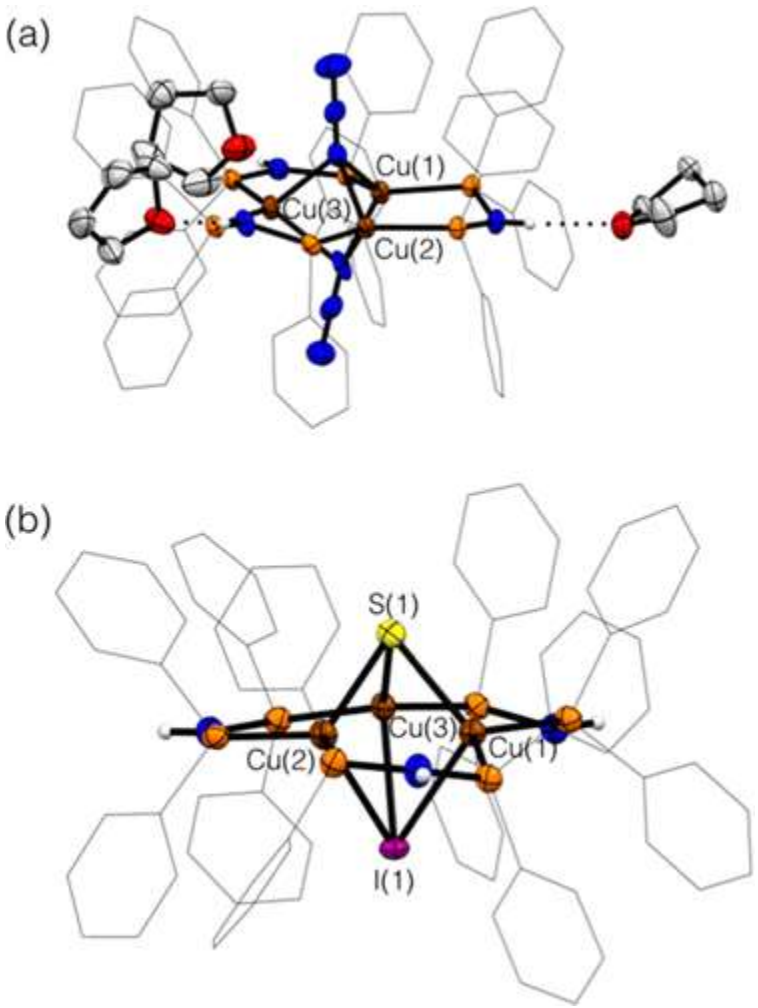

Figure 4. Solid-state structures of (a) **4**·3THF and (b) **5** determined by X-ray crystallography. Core atoms are shown as 50% probability ellipsoids, phosphine substituents are shown as wireframes, and C–H hydrogen atoms have been omitted for clarity. Cocrystallized anions and solvent molecules are shown only if engaged in hydrogen bonding to the cationic unit. N–H hydrogen atoms are shown in calculated positions. Atom colors: C, gray; H, white; Cu, brown; F, green; I, purple; N, blue; O, red; P, orange; S, yellow.

Complex **2** also reacted readily with excess NaI at room temperature, producing a mixture of two new complexes that were each identified crystallographically (Scheme 2). One of the products was $[(\mu_2\text{-dppa})_3Cu_3(\mu_3\text{-S})(\mu_3\text{-I})]$ (**5**; Figure 4), and the second product was $[(\mu_2\text{-dppa})_3Cu_3(\mu_3\text{-I})_2][PF_6]$ (**6**; Figure S46 in the SI). A toluene extraction was used to separate neutral **5** from cationic **6**, which were produced in a ratio of 1:5.8 in the crude reaction mixture (Figures S27–S31 in the SI). We suspect that Na_2S was a byproduct of this reaction, accounting for the displaced sulfide equivalents. The solid-

state structures of both **5** and **6** featured roughly C_3-symmetric tricopper clusters. In the case of **6**, one THF molecule was found hydrogen bonding to a N–H group in the secondary coordination sphere. In the case of **5**, no such interactions were detected (Figure 4). Presumably, the N–H groups in **5** are less acidic because of the neutral charge of the complex and therefore do not engage as readily in hydrogen-bonding interactions. The crystal structure of N_2OR under iodide inhibition features an iodide-bound Cu_Z* cluster with a [$Cu_4(\mu_4$-S)(μ_2-I)] core that is related to the [$Cu_3(\mu_3$-S)(μ_3-I)] core found in **5**, although the Cu···μ_2-I distances observed in the enzyme are shorter (2.5 and 2.8 Å) than the Cu···μ_3-I distances observed in **5** [2.8632(12), 2.9390(14), and 2.9481(12) Å].[29] For comparison, the Cu···μ_3-I distances in **6** ranged from 2.7152(9) to 2.7608(8) Å.

In N_2OR, the Cu_Z* cluster is inhibited from reacting with its normal substrate, N_2O, when I^- is present. Similarly, model complex **2** is inhibited from reacting with N_3^- by the presence of I^-. Several experiments were used to establish this behavior. First of all, the reaction of **2** with a 1:1 mixture of NaI/NaN_3 produced **5** and **6** with no evidence for the formation of **2'** or **4** by ^{31}P NMR (Figures S33–S35 in the SI), indicating the strong kinetic preference for the I^- reaction with the [$Cu_4(\mu_4$-S)] core over the N_3^- reaction. The reaction of **4** with excess NaI cleanly produced **6** (Figures S36–S38 in the SI), while no reaction was observed between NaN_3 and either **5** or **6** (Scheme 3 and Figures S39–S41 in the SI). This set of experiments provides further indication that I^- binds strongly to the multicopper clusters and inhibits a reaction with an otherwise competent substrate, N_3^-, in analogy to Cu_Z* inhibition.

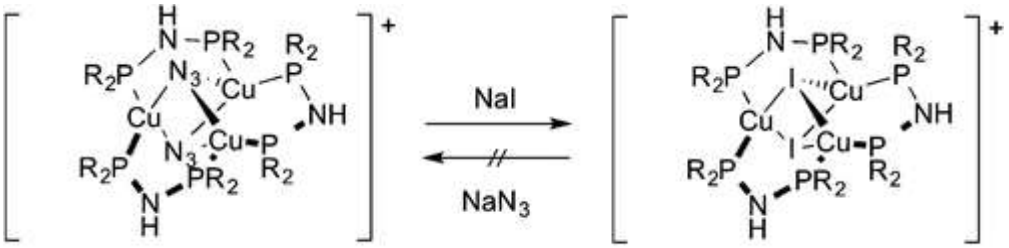

4 **6**

Scheme 3. Competitive Binding of I^- over N_3^-

Inorganic Chemistry, Vol 53, No. 19 (2014): pg. 10611-10619. DOI.

Conclusions

In conclusion, the self-assembly of [$Cu_n(\mu_n$-S)] clusters structurally related to the Cu_Z* site of N_2OR was observed using bridging diphosphine supporting ligands. The identity of the diphosphine unit controlled the nature of the cluster that assembled, enabled tuning of thermodynamic reduction potentials of the clusters, and was used to introduce hydrogen-bond donors to the secondary coordination sphere of one model. Reactivity studies of this [$Cu^I_4(\mu_4$-S)] model with various anions provided information related to the different binding preferences of such copper–sulfur clusters. Specifically, the reactivity data presented here indicate that the [$Cu^I_4(\mu_4$-S)] model complex **2** binds anions in the following order of preference: $I^- > N_3^- > NO_2^-$. These reactions resulted in a breakdown of the tetracopper cluster to generate various tricopper clusters, in some cases with displacement of the sulfide unit. Such loss of nuclearity and stoichiometry is likely prevented for Cu_Z* by the rigid secondary structure provided by N_2OR,[1,5] highlighting an important challenge in modeling this fascinating active site. Further tuning of these clusters through the design of bridging diphosphine units will be pursued with emphasis on enabling reactivity with N_2O itself.

Experimental Section

General Considerations

Unless otherwise specified, all reactions and manipulations were performed under purified N_2 in a glovebox or using standard Schlenk-line techniques. Glassware was oven-dried prior to use. Acetone and methanol were degassed with N_2, dried over K_2CO_3, and then distilled and stored over activated 3-Å molecular sieves. Other reaction solvents (diethyl ether, toluene, tetrahydrofuran, and dichloromethane) were sparged with argon and dried using a Glass Contour Solvent System built by Pure Process Technology, LLC. Unless otherwise specified, all chemicals were purchased from commercial sources and used without further purification.

Inorganic Chemistry, Vol 53, No. 19 (2014): pg. 10611-10619. DOI.

Physical Measurements

NMR spectra were recorded at ambient temperatures using a Bruker Avance DPX-400 or a Bruker Avance DRX-500 MHz spectrometer. ^{1}H NMR chemical shifts were referenced to residual solvent peaks. ^{31}P NMR chemical shifts were referenced to external H_3PO_4 (δ = 0). The following data acquisition parameters were used for quantative ^{31}P NMR spectroscopy: single pulse, 8.00 μs; power level, −3.00 dB; frequency offset of the third nucleus, −748516.887 ppm; recycle delay, 10 s; number of scans, 128. The signal-to-noise ratio calculated for ^{31}P NMR using these parameters was 0.8%. Fourier transform infrared (FT-IR) spectra were recorded on solid samples in a glovebox using a Bruker ALPHA spectrometer fitted with a diamond-ATR detection unit. Elemental analyses were performed by the Midwest Microlab, LLC, Indianapolis, IN. Deuterated solvents were degassed by repeated freeze–pump–thaw cycles and then stored over 3-Å molecular sieves. UV–vis absorbance spectra were taken at room temperature using a Cary 300 Bio UV–vis spectrophotometer. Fluorescence emission spectra were taken at room temperature using a customized Fluorolog (Horiba Jobin Yvon) modular spectrofluorometer. Luminescence quantum yields were determined based on eq 1, where *A* is the measured absorbance at the excitation wavelength and *I* is the integrated emission intensity when samples were excited at 415 nm. A 7.10 × 10^{-4} M solution of compound **1** (Φ = 0.22;[10] excitation wavelength = 415 nm) in MeCN was used as the standard reference solution. Samples for emission measurements were prepared as solutions of compounds **2** and **3**, in MeCN, at concentrations of 5.66 × 10^{-4} and 3.14 × 10^{-3} M, respectively.

$$\phi_{\text{sample}} = \phi_{\text{reference}} \frac{A_{\text{reference}}}{A_{\text{sample}}} \frac{I_{\text{sample}}}{I_{\text{reference}}} \quad (1)$$

Electrochemical data were measured at room temperature using a WaveNow USB potentiostat from Pine Research Instrumentation. In a classic three-electrode system, a platinum working electrode, a platinum counter electrode, and a $Ag/AgNO_3$ (0.01 M $AgNO_3$/0.1 M Bu_4NPF_6 in MeCN) reference electrode were used. Compounds **2** and **3** were dissolved in a 0.1 M solution of Bu_4NPF_6 in MeCN at 1.88 × 10^{-3} M concentration. Electrochemical measurements were referenced to a

Inorganic Chemistry, Vol 53, No. 19 (2014): pg. 10611-10619. DOI.

1.88 × 10^{-3} M solution of $FeCp_2^{+/0}$ in the same MeCN electrolyte solution.

X-ray Crystallography

X-ray crystallography data were collected at the X-ray Structural Laboratory at Marquette University (Milwaukee, WI) for complexes **2**, **2'**, **3**, **4**, and **5**. Single-crystal X-ray diffraction data were collected at 100 K with an Oxford Diffraction SuperNova κ diffractometer equipped with dual microfocus Cu/Mo X-ray sources, X-ray mirror optics, an Atlas CCD detector, and a low-temperature Cryojet device. The data were processed with the *CrysAlisPro* program package (Oxford Diffraction Ltd., 2010) typically using a numerical Gaussian absorption correction (based on the real shape of the crystal) followed by an empirical multiscan correction using the *SCALE3 ABSPACK* routine. The structures were solved using the *SHELXS* program and refined with the *SHELXL* program[30] within the *Olex2* crystallographic package.[31] All computations were performed on an Intel PC computer under Windows 7 OS. X-ray crystallography data were collected at the University of Illinois at Chicago for complex **6**. Single-crystal X-ray diffraction data were collected at 200 K with a Bruker SMART X2S benchtop diffractometer fitted with an Oxford Cryostreams Desktop Cooler. The structure was solved using *SHELXS* and refined with *SHELXL*.[30]

Most of the structures contain a certain degree of disorder, which was detected in difference Fourier syntheses of the electron density and was taken care of using the capabilities of the *SHELX* package. In most cases, hydrogen atoms were localized in difference syntheses of the electron density but were refined using appropriate geometric restrictions on the corresponding bond lengths and bond angles within a riding/rotating model (torsion angles of the Me hydrogen atoms were optimized to better fit the residual electron density). The particular nonstandard details of the structure solution and refinement are as indicated in the figure captions included as SI.

Preparation of Bis(diphenylphosphino)amine (dppa)

A literature procedure was adapted for the isolation of dppa.[32] Toluene (30 mL), chlorodiphenylphosphine (3.30 mL, 18.4 mmol), and

Inorganic Chemistry, Vol 53, No. 19 (2014): pg. 10611-10619. DOI.

hexamethyldisilazane (1.92 mL, 9.23 mmol) were added sequentially to a 100 mL three-necked round-bottom flask inside a glovebox. Upon the addition of hexamethyldisilazane, a white precipitate began to form. The three necks were then equipped with a glass stopper, a reflux condenser fitted with a vacuum adaptor and a flow regulator, and a vacuum adaptor with a flow regulator, respectively. Once assembled and internally sealed, the flask was removed from the glovebox, connected to a Schlenk line, and refluxed at 125 °C for 3 h. During reflux, the solution appeared to turn pale yellow with no precipitate present. After reflux, the solution was cooled to room temperature and the reflux condenser was exchanged for a glass stopper. Volatiles were then removed by vacuum evaporation (evaporation removes not only the toluene but also the byproduct Me_3SiCl). The remaining solid after evaporation was white. While the flask was under vacuum, the solid was pumped back into the glovebox. It was then washed with diethyl ether (2 × 10 mL) and dried. Yield of dppa: 2.292 g, 64%. NMR spectroscopy of the isolated product matches that of the material purchased from a commercial vendor (Strem). ^{1}H NMR (500 MHz, CD_3CN): δ 4.33 (s, 1H, N–H), 7.33–7.38 (m, 20H, phenyls). $^{31}P\{^1H\}$ NMR (500 MHz, CD_3CN): δ 41.6 (s).

Preparation of Dicopper Precursor Complexes

Reported literature procedures for $[(\mu_2\text{-dppa})_2Cu_2(MeCN)_4][PF_6]_2$[16] and $[(\mu_2\text{-dcpm})_2Cu_2][PF_6]_2$[20] were used with the following modifications. In our hands, the reported procedure produced $[(\mu_2\text{-dppa})_2Cu_2(MeCN)_2][PF_6]_2$ with only two coordinated acetonitrile molecules rather than four, which was confirmed by ^{1}H NMR integration in DMSO-d_6. The molecular weight for $[(\mu_2\text{-dppa})_2Cu_2(MeCN)_2][PF_6]_2$ (1269.78 g mol^{-1}) was then used for all subsequent stoichiometric calculations. In the preparation of $[(\mu_2\text{-dcpm})_2Cu_2][PF_6]_2$, CH_2Cl_2 was used as the reaction solvent.

*Preparation of $[(\mu_2\text{-dppa})_4Cu_4(\mu_4\text{-S})][PF_6]_2$ (**2**)*

$[(\mu_2\text{-dppa})_2Cu_2(MeCN)_2][PF_6]_2$ (1.00 g, 0.787 mmol) was added to a flask charged with acetone (30 mL) and a magnetic stir bar. In a separate vessel, Na_2S (0.0307 g, 0.393 mmol) was stirred in methanol

Inorganic Chemistry, Vol 53, No. 19 (2014): pg. 10611-10619. DOI.

(10 mL) until completely dissolved. The methanol solution of Na_2S was then added to the $[(\mu_2\text{-dppa})_2Cu_2(MeCN)_2][PF_6]_2$ solution dropwise, with stirring, at room temperature. Once all of the Na_2S solution had been added, the resulting deep-orange reaction mixture was stirred at room temperature for 3 h. The volume was reduced to 20 mL by vacuum evaporation, and then the solution was pipet-filtered through Celite to remove $NaPF_6$. The filtered solution was then completely evaporated and reconstituted in acetone (4 mL). Diethyl ether (approximately 10–12 mL) was slowly added, causing a bright-yellow precipitate to form. The yellow precipitate was collected by vacuum filtration and dried under vacuum. Yield of **2**: 0.593 g, 71%. Orange crystals may be obtained by dissolving yellow **2** in a minimum amount in acetone and allowing diethyl ether vapors to diffuse in through a pin-sized hole. ^{1}H NMR (500 MHz, acetone-d_6): δ 2.08 (s, coordinated acetone), 6.06 (s, N–H), 7.12–7.39 (m, 80H, phenyls). Note: Integration values for the N–H and coordinated solvent resonances were consistently lower than expected, possibly because of exchange processes with free solvent. $^{31}P\{^1H\}$ NMR (500 MHz, acetone-d_6): δ 36.6 (s, dppa), −145.8 (sept, J = 707.5 Hz, PF_6^-). FT-IR (cm^{-1}): 3297 (N–H), 3052, 1481, 1434, 1098, 832, 734, 688, 555, 521, 481. Anal. Calcd for $C_{96}H_{84}Cu_4F_{12}N_4P_{10}S$: C, 54.57; H, 3.97; N, 2.64. Found: C, 54.44; H, 4.08; N, 2.75. Note: The sample submitted for elemental analysis was dissolved in THF and then evaporated by vacuum three times to remove coordinated acetone molecules. Such a treatment was also used to prepare samples of **2** for further reactivity studies described below.

*Preparation of $[(\mu_2\text{-dcpm})_3Cu_3(\mu_3\text{-S})][PF_6]$ (**3**)*

$[(\mu_2\text{-dcpm})_2Cu_2][PF_6]_2$ (1.00 g, 0.810 mmol) was dissolved acetone (30 mL) while stirring with a magnetic stir bar. In a separate vessel, Na_2S (0.042 g, 0.54 mmol) was stirred in methanol (7.5 mL) until completely dissolved. The Na_2S solution was then added dropwise at room temperature to the $[(\mu_2\text{-dcpm})_2Cu_2][PF_6]_2$ solution. Once the entire solution of Na_2S had been added, the resulting deep-amber reaction mixture was stirred at room temperature for 3 h. The solution was vacuum evaporated to approximately 5 mL and then pipet-filtered through Celite to remove $NaPF_6$. The resulting solution was then completely evaporated, and recrystallization was conducted using the

Inorganic Chemistry, Vol 53, No. 19 (2014): pg. 10611-10619. DOI.

same vapor diffusion method as that described for complex **2**. Yield of **3**: 0.472 g, 55%. ^{1}H NMR (400 MHz, DMSO-d_6): δ 1.12–1.40 (m, 60H, cyclohexyl), 1.62–1.98 (m, 72H, cyclohexyl). ^{31}P{^{1}H} NMR (500 MHz, acetone-d_6): δ −6.0 (s, dcpm), −146.8 (sept, J = 707.7 Hz, PF_6^-). FT-IR (cm^{-1}): 2920, 2846, 1444, 834, 754, 556, 513. Anal. Calcd for $C_{75}H_{138}Cu_3F_6P_7S$: C, 56.23; H, 8.73; N, 0.00. Found: C, 56.24; H, 8.47; N, 0.00.

*Reaction between **2** and NaN_3*

A solution of **2** (0.013 g, 0.0061 mmol) was prepared in THF (1 mL). In a separate vessel, NaN_3 (0.0039 g, 0.060 mmol) was dissolved in MeOH (1 mL). The NaN_3 solution was then added dropwise to the solution of **2** at room temperature with stirring. No immediate color change was observed. The solution appeared cloudy during initial drops of NaN_3 but was then completely clear once all NaN_3 had been added. Stirring was continued at room temperature for 16 h, during which time the reaction mixture became darker orange. The solution was then evaporated to dryness under vacuum, reconstituted in CD_2Cl_2, and then pipet-filtered through Celite to remove $NaPF_6$ and unreacted NaN_3. The column of Celite in the pipet was washed with a small amount of CD_2Cl_2 to capture as much product as possible. To the sample was added a solution of tri-*o*-tolylphosphine (200 μL of a 0.030 M solution in CD_2Cl_2, 0.0060 mmol) as a ^{31}P NMR internal standard. Yields based on quantitative ^{31}P NMR: **2′**, 51%; **4**: 19%; unreacted **2**, 8%. Crystals of **2′** and **4** were obtained by vapor diffusion of diethyl ether into a THF solution of the crude mixture in the same manner as that for complex **2**. ^{1}H NMR (400 MHz, CD_2Cl_2): δ 1.81 (m, 1.1H, coordinated THF), 2.37 (s, 8.8H, *o*-CH_3 in tri-*o*-tolylphosphine), 3.54 (s, 0.71H, N–H of **4**), 3.64 (s, integral not determined due to peak overlap, N–H of **2′**), 3.66 (m, integral not determined due to peak overlap, coordinated THF), 6.69–7.37 (m, 60H, phenyls). ^{31}P{^{1}H} NMR (400 MHz, CD_2Cl_2): δ 40.3 (s, dppa of **4**), 38.6 (s, unknown), 36.7 (s, unreacted **2**), 35.4 (s, dppa of **2′**), −31.83 (s, tri-*o*-tolylphosphine), −146.09 (sept, J = 710.4 Hz, PF_6^-).

Inorganic Chemistry, Vol 53, No. 19 (2014): pg. 10611-10619. DOI.

*Preparation of [(μ_2-dppa)$_3$Cu$_3$(μ_3-N$_3$)$_2$][PF$_6$] (**4**) from N$_3$SiMe$_3$*

To a solution of **2** (0.090 g, 0.042 mmol) in THF (3 mL) was added N_3SiMe_3 (56 μL, 0.42 mmol). No immediate color change or precipitate was observed. Stirring was continued at room temperature for 16 h, during which time the reaction color changed to dark red. The mixture was evaporated to dryness under vacuum. The red-brown residue was then reconstituted in THF (1 mL), and diethyl ether (1 mL) was added dropwise until a precipitate began to form. The tan precipitate was collected by vacuum filtration, washed with diethyl ether (2 × 3 mL), then dissolved in CH_2Cl_2 (2 mL), and pipet-filtered through Celite. The solution was then evaporated to dryness under vacuum. Crystals were obtained by vapor diffusion of diethyl ether into a THF solution in the same manner that as described for complex **2**. Yield of **4**: 0.0453 g, 68%. ^{1}H NMR (400 MHz, CD_2Cl_2): δ 3.61 (s, 3H, N–H), 7.09–7.33 (m, 63H, phenyls). ^{31}P{^{1}H} NMR (400 MHz, CD_2Cl_2): δ 40.30 (s, dppa), −146.12 (sept, J = 710.3 Hz, PF_6^-). FT-IR (cm^{-1}): 3274 (N–H), 3052, 2920, 2851, 2046 (N_3), 1481, 1434, 1303, 1099, 909, 833, 734, 691, 522, 481. Anal. Calcd for $C_{72}H_{63}Cu_3F_6N_9P_7$: C, 54.88; H, 4.03; N, 8.00. Found: C, 54.57; H, 4.07; N, 7.80.

*Reaction between **2** and NaI*

A solution of **2** (0.046 g, 0.0217 mmol) was prepared in THF (2 mL). In a separate vessel, NaI (0.0325 g, 0.218 mmol) was dissolved in MeOH (1 mL). The NaI solution was then added dropwise to the solution of **2** at room temperature with stirring. No immediate color change or precipitate was observed. The solution continued to stir at room temperature for 16 h, during which time the reaction mixture became darker orange after 16 h and was completely evaporated by vacuum. The solution was then evaporated to dryness under vacuum, reconstituted in CD_2Cl_2, and then pipet-filtered through Celite to remove $NaPF_6$ and unreacted NaI. The column of Celite in the pipet was washed with a small amount of CD_2Cl_2 to capture as much product as possible. To the sample was added a solution of tri-*o*-tolylphosphine (200 μL of a 0.216 M solution in CD_2Cl_2, 0.0216 mmol) as a ^{31}P NMR internal standard. Yields based on quantitative ^{31}P NMR: **6**, 75%; **5**, 13%. Crystals of **5** and **6** were obtained by vapor diffusion of diethyl

Inorganic Chemistry, Vol 53, No. 19 (2014): pg. 10611-10619. DOI.

ether into a THF solution of the crude mixture in the same manner as that for complex **2**. ^{1}H NMR (400 MHz, CD_2Cl_2): δ 1.81 (m, 2.1H, coordinated THF), 2.37 (s, 8.9H, *o*-CH_3 in tri-*o*-tolylphosphine), 3.65 (m, 2.1H, coordinated THF), 3.85 (s, 0.38H, N–H of **5**), 3.87 (s, 1.2H, N–H of **6**), 7.08–7.30 (m, 54.3H, phenyls). ^{31}P{^{1}H} NMR (400 MHz, CD_2Cl_2): δ 33.9 (s, dppa of **5**), 29.7 (s, dppa of **6**), −31.8 (s, tri-*o*-tolylphosphine), −146.1 (sept, J = 710.5 Hz, PF_6^-). Spectroscopic characterization was verified by toluene precipitation followed by washing of the solid with diethyl ether. The combined soluble fractions were predominantly **5**, while the solid fraction was predominantly **6**. Characterization of **6**. ^{1}H NMR (400 MHz, CD_2Cl_2): δ 1.81 (m, 2H, coordinated THF), 3.56 (s, 3H, N–H), 3.66 (m, 2H, coordinated THF), 7.08–7.30 (m, 60H, phenyls). ^{31}P{^{1}H} NMR (400 MHz, CD_2Cl_2): δ 29.6 (s, dppa), −146.1 (sept, J = 710.3 Hz, PF_6^-). FT-IR (cm^{-1}): 3281 (N–H), 3051, 2921, 2852, 2120, 1481, 1433, 1099, 927, 836, 734, 691, 523, 481.

Author Contributions

The manuscript was written through contributions of all authors. All authors have given approval to the final version of the manuscript.

The authors declare no competing financial interest.

Acknowledgment

Prof. Preston Snee and Armen Shamirian assisted with fluorescence measurements and quantum yield calculations. Dr. Dan McIlheny assisted with NMR measurements. We are grateful to the colleagues of Prof. Gregory Hillhouse for sharing an unpublished version of their manuscript in preparation. Start-up funds to N.P.M. were provided by the Department of Chemistry, University of Illinois at Chicago.

References

[1]Pauleta, S. R.; Dell'Acqua, S.; Moura, I. Coord. Chem. Rev. 2013, 257, 332–349

[2](a) Brown, K.; Tegoni, M.; Prudêncio, M.; Pereira, A. S.; Besson, S.; Moura, J. J.; Moura, I.; Cambillau, C. Nat. Struct. Biol. 2000, 7, 191– 195. (b) Rasmussen, T.; Berks, B. C.; Sanders-Loehr, J.; Dooley, D. M.; Zumft, W. G.; Thomson, A. J. Biochemistry 2000, 39, 12753– 12756

[3]Pomowski, A.; Zumft, W. G.; Kroneck, P. M. H.; Einsle, O. Nature 2011, 477, 234– 237

[4]Johnston, E. M.; Dell'Acqua, S.; Ramos, S.; Pauleta, S. R.; Moura, I.; Solomon, E. I. J. Am. Chem. Soc. 2014, 136, 614– 617

[5]Gorelsky, S. I.; Ghosh, S.; Solomon, E. I. J. Am. Chem. Soc. 2006, 128, 278– 290

[6]Bar-Nahum, I.; Gupta, A. K.; Huber, S. M.; Ertem, M. Z.; Cramer, C. J.; Tolman, W. B. J. Am. Chem. Soc. 2009, 131, 2812– 2814

[7](a) Di Francesco, G. N.; Gaillard, A.; Ghiviriga, I.; Abboud, K. A.; Murray, L. J. Inorg. Chem. 2014, 53, 4647– 4654. (b) Zhai, J.; Hillhouse, G. L. Manuscript in preparation. (c) Gourlay, C.; Nielsen, D. J.; White, J. M.; Knottenbelt, S. Z.; Kirk, M. L.; Young, C. G. J. Am. Chem. Soc. 2006, 128, 2164– 2165. (d) Liu, H.; Tan, A. L.; Mok, K. F.; Mak, T. C.; Batsanov, A. S.; Howard, J. A.; Hor, T. S. A. J. Am. Chem. Soc. 1997, 119, 11006– 11011. (e) Delgado, S.; Sanz Miguel, P. J.; Priego, J. L.; Jiménez-Aparicio, R.; Gómez-García, C. J.; Zamora, F. Inorg. Chem. 2008, 47, 9128– 9130

[8]Selected references featuring copper clusters with multiple μ_4-S ligands: (a) Khadka, C. B.; Najafabadi, B. K.; Hesari, M.; Workentin, M. S.; Corrigan, J. F. Inorg. Chem. 2013, 52, 6798– 6805. (b) Lee, Y.; Sarjeant, A. A. N.; Karlin, K. D. Chem. Commun. 2006, 621. (c) Dehnen, S.; Schäfer, A.; Fenske, D.; Ahlrichs, R. Angew. Chem., Int. Ed. Engl. 1994, 33, 746– 749

[9]Selected references featuring copper clusters with multiple μ_3-S ligands: (a) York, J. T.; Bar-Nahum, I.; Tolman, W. B. Inorg. Chem. 2007, 46, 8105– 8107. (b) Lang, J.-P.; Tatsumi, K. Inorg. Chem. 1998, 37, 160– 162. (c) Betz, P.; Krebs, B.; Henkel, G. Angew. Chem., Int. Ed. Engl. 1984, 23, 311– 312

[10]Selected references: (a) Yam, V. W.-W.; Lo, K. K.-W.; Fung, W. K.-M.; Wang, C.-R. Coord. Chem. Rev. 1998, 171, 17– 41. (b) Wang, C.-R.; Lo, K. K.-W.; Fung, W. K.-M.; Yam, V. W.-W. Chem. Phys. Lett. 1998, 296, 505– 514. (c) Yam, V. W.-W.; Lee, W.-K.; Lai, T.-F. J. Chem. Soc., Chem. Commun. 1993, 1571. (d) Yang, R. N.; Sun, Y. A.; Hou, Y. M.; Hu, X. Y.; Jin, D. M. Inorg. Chim. Acta 2000, 304, 1– 6

[11]York, J. T.; Bar-Nahum, I.; Tolman, W. B. Inorg. Chim. Acta 2008, 361, 885– 893

[12]Chen, P.; Cabrito, I.; Moura, J. J. G.; Moura, I.; Solomon, E. I. J. Am. Chem. Soc. 2002, 124, 10497– 10507

[13]Lam, W. H.; Cheng, E. C.-C.; Yam, V. W.-W. Inorg. Chem. 2006, 45, 9434– 9441

[14]Selected references: (a) Lacy, D. C.; Park, Y. J.; Ziller, J. W.; Yano, J.; Borovik, A. S. J. Am. Chem. Soc. 2012, 134, 17526– 17535. (b) Okamura, T.-A.; Ushijima, Y.; Omi, Y.; Onitsuka, K. Inorg. Chem.

2013, 52, 381– 394. (c) Tolman, W. B. Inorg. Chem. 2013, 52, 7307– 7310

[15]Haltia, T.; Brown, K.; Tegoni, M.; Cambillau, C.; Saraste, M.; Mattila, K.; Djinovic-Carugo, K. Biochem. J. 2003, 369, 77– 88

[16]Liu, H.; Calhorda, M. J.; Drew, M. G. B.; Felix, V.; Novosad, J.; Veiros, L. F.; de Biani, F. F.; Zanello, P. J. Chem. Soc., Dalton Trans. 2002, 4365– 4374

[17]Han, L.; Shi, L.-X.; Zhang, L.-Y.; Chen, Z.-N.; Hong, M.-C. Inorg. Chem. Commun. 2003, 6, 281– 283

[18]τ_4 is a geometry index for four-coordinate centers, calculated to be 0 for square-planar geometries and 1 for tetrahedral geometries. See: Yang, L.; Powell, D. R.; Houser, R. P. Dalton Trans. 2007, 955– 964

[19]Because both **1** and **2** are thermodynamically competent to reduce O_2 according to their redox potentials, we propose that kinetic binding of O_2 through the use of hydrogen bonds is the operative factor.

[20]Che, C.; Mao, Z.; Miskowski, V. M.; Tse, M. C.; Chan, C. K.; Cheung, K. K.; Phillips, D. L.; Leung, K. H. Angew. Chem., Int. Ed. 2000, 39, 4084– 4088

[21]Selected examples for comparison (cathodic shift of 0.47 V for dppa versus dppm when compared on the same potential scale): (a) Simón-Manso, E.; Kubiak, C. P. Organometallics 2005, 24, 96– 102. (b) DeLaet, D. L.; Del Rosario, R.; Fanwick, P. E.; Kubiak, C. P. J. Am. Chem. Soc. 2001, 109, 754– 758

[22](a) Berry, J. F. Chem.—Eur. J. 2010, 16, 2719– 2724. (b) Sarangi, R.; Yang, L.; Winikoff, S. G.; Gagliardi, L.; Cramer, C. J.; Tolman, W. B.; Solomon, E. I. J. Am. Chem. Soc. 2011, 133, 17180– 17191. (c) Sarangi, R.; York, J. T.; Helton, M. E.; Fujisawa, K.; Karlin, K. D.; Tolman, W. B.; Hodgson, K. O.; Hedman, B.; Solomon, E. I. J. Am. Chem. Soc. 2008, 130, 676– 686

[23]Bockman, T. M.; Kochi, J. K. J. Org. Chem. 1990, 55, 4127– 4135

[24]Pavlishchuk, V. V.; Addison, A. W. Inorg. Chim. Acta 2000, 298, 97– 102

[25]On the basis of the fact that fully reduced Cu_Z cannot be accessed by methyl viologen reduction, this also serves as an upper limit on the $Cu^{II}Cu^{I}_3/Cu^{I}_4$ potential of Cu_Z.

[26]The UV–vis spectrum of **3** also features a shoulder at 229 nm and a maximum at 216 nm.

[27]Recent examples: (a) Tskhovrebov, A. G.; Solari, E.; Scopelliti, R.; Severin, K. Organometallics 2012, 31, 7235– 7240. (b) Piro, N. A.; Lichterman, M. F.; Harman, W. H.; Chang, C. J. J. Am. Chem. Soc. 2011, 133, 2108– 2111. (c) Lee, J.-H.; Pink, M.; Tomaszewski, J.; Fan, H.; Caulton, K. G. J. Am. Chem. Soc. 2007, 129, 8706– 8707. (d) Pamplin, C. B.; Ma, E. S. F.; Safari, N.; Rettig, S. J.; James, B. R. J. Am. Chem. Soc. 2001, 123, 8596– 8597

Inorganic Chemistry, Vol 53, No. 19 (2014): pg. 10611-10619. DOI.

[28](a) Kiefer, G.; Jeanbourquin, L.; Severin, K. Angew. Chem., Int. Ed. 2013, 52, 6302– 6305. (b) Jayarathne, U.; Parmelee, S. R.; Mankad, N. P. Inorg. Chem. 2014, 53, 7730– 7737. (c) Esmieu, C.; Orio, M.; Torelli, S.; Le Pape, L.; Pécaut, J.; Lebrun, C.; Ménage, S. Chem. Sci. 2014, doi:, DOI: 10.1039/C4SC01487A .

[29]Paraskevopoulos, K.; Antonyuk, S. V.; Sawers, R. G.; Eady, R. R.; Hasnain, S. S. J. Mol. Biol. 2006, 362, 55– 65

[30]Sheldrick, G. M. Acta Crystallogr. 2008, A64, 112– 122

[31]Dolomanov, O. V.; Bourhis, L. J.; Gildea, R. J.; Howard, J. A. K.; Puschmann, H. J. Appl. Crystallogr. 2009, 42, 339– 341

[32]Magennis, S. W.; Parsons, S.; Pikramenou, Z. Chem.—Eur. J. 2002, 8, 5761– 5771

Assembly, Structure, and Reactivity of Cu_4S and Cu_3S Models for the Nitrous Oxide Reductase Active Site, Cu_Z*

*Brittany J. Johnson, Sergey V. Lindeman, Neal P. Mankad**

Supporting Information

Contents:

Figure S1. ^{1}H NMR of bis(diphenylphosphino)amine

Figure S2. ^{31}P NMR of bis(diphenylphosphino)amine

Figure S3. ^{1}H NMR of $[(\mu_2\text{-dppa})_2Cu_2(MeCN)_2][PF_6]_2$

Figure S4. ^{31}P NMR of $[(\mu_2\text{-dppa})_2Cu_2(MeCN)_2][PF_6]_2$

Figure S5. ^{1}H NMR of $[(\mu_2\text{-dcpm})_2Cu_2][PF_6]_2$

Figure S6. ^{31}P NMR of $[(\mu_2\text{-dcpm})_2Cu_2][PF_6]_2$

Figure S7. ^{1}H NMR of compound **2**

Figure S8. ^{31}P NMR of compound **2**

Figure S9. Infrared spectrum of compound **2**

Figure S10. Absorption spectrum of **2**

Figure S11. Cyclic voltammogram of **2**

Table S1. Cyclic voltammogram parameters for **2**

Figure S12. Cyclic voltammograms with scan rate dependence for **2**

Table S2. Cyclic voltammetry parameters used for scan rate dependence of **2**

Figure S13. Plot of square root of scan rate vs. current in the forward direction, demonstrating the reversibility of the first oxidation of **2**

Figure S14. ^{1}H NMR of compound **3**

Figure S15. ^{31}P NMR of compound **3**

Figure S16. Infrared spectrum of **3**

Figure S17. Absorption spectrum of **3**

Figure S18. Cyclic voltammogram of **3**

Table S3. Cyclic voltammogram parameters for **3**

Figure S19. Cyclic voltammograms with scan rate dependence for **3**

Table S4. Cyclic voltammetry parameters used for scan rate dependence of **3**

Figure S20. Plot of square root of scan rate vs. current in the forward direction, demonstrating the reversibility of the first oxidation of **3**

Figure S21. Normalized emission spectra for compounds **1**, **2** and **3**

Figure S22. ^{1}H NMR for the reaction between **2** and excess NaN_3

Figure S23. ^{31}P NMR for the reaction between **2** and excess NaN_3

Figure S24. ^{1}H NMR of compound **4** from N_3SiMe_3

Figure S25. ^{31}P NMR of compound **4** from N_3SiMe_3

Figure S26. Infrared spectrum of **4**

Figure S27. ^{1}H NMR for the reaction between **2** and excess NaI

Figure S28. ^{31}P NMR for the reaction between **2** and excess NaI

Figure S29. ^{1}H NMR of compound **6**

Figure S30. ^{31}P NMR of compound **6**

Figure S31. Infrared spectrum of **6**

Figure S32. Cyclic voltammogram of Bu_4NPF_6 in MeCN used as electrolyte solution in all CV experiments

Table S5. Cyclic voltammetry parameters used for Bu_4NPF_6 in MeCN

Experimental Conditions: Competition reaction of NaI/ NaN_3 and **2**

Figure S33. ^{1}H NMR of competition reaction between NaI/ NaN_3 and **2**

Figure S34. ^{31}P NMR of competition reaction between NaI/ NaN_3 and **2**

Figure S35. ^{31}P NMR comparison of Figure S28 and Figure S34

Figure S36. ^{1}H NMR **4** and excess NaI

Figure S37. ^{31}P NMR of **4** and excess NaI

Figure S38. ^{31}P NMR comparison of **4** and excess NaI with **4** starting material

Figure S39. ^{1}H NMR of mixture of **5** and **6** with excess NaN_3

Figure S40. ^{31}P NMR of mixture of **5** and **6** with excess NaN_3

Figure S41. ^{31}P NMR comparison of mixture of **5** and **6** with excess NaN_3 and **5** and **6** starting materials

Figure S42. Fully labeled ORTEP of the dicationic unit in complex **2**

Figure S43. Crystal packing diagram for **2**

Table S6. Crystal data and structure refinement for **2**

Figure S44. Fully labeled ORTEP of the cationic unit in complex **2'**

Figure S45. Crystal packing diagram for **2'**

Table S7. Crystal data and structure refinement for **2'**

Figure S46. Fully labeled ORTEP of the cationic unit in complex **3**

Figure S47. Crystal packing diagram for **3**

Table S8. Crystal data and structure refinement for **3**

Figure S48. Fully labeled ORTEP of complex **4**

Figure S49. Crystal packing diagram for **4**

Table S9. Crystal data and structure refinement for **4**

Figure S50. Fully labeled ORTEP of complex **5**

Figure S51. Crystal packing diagram for **5**

Table S10. Crystal data and structure refinement for **5**

Figure S52. Fully labeled ORTEP of complex **6**

Table S11. Crystal data and structure refinement for **6**

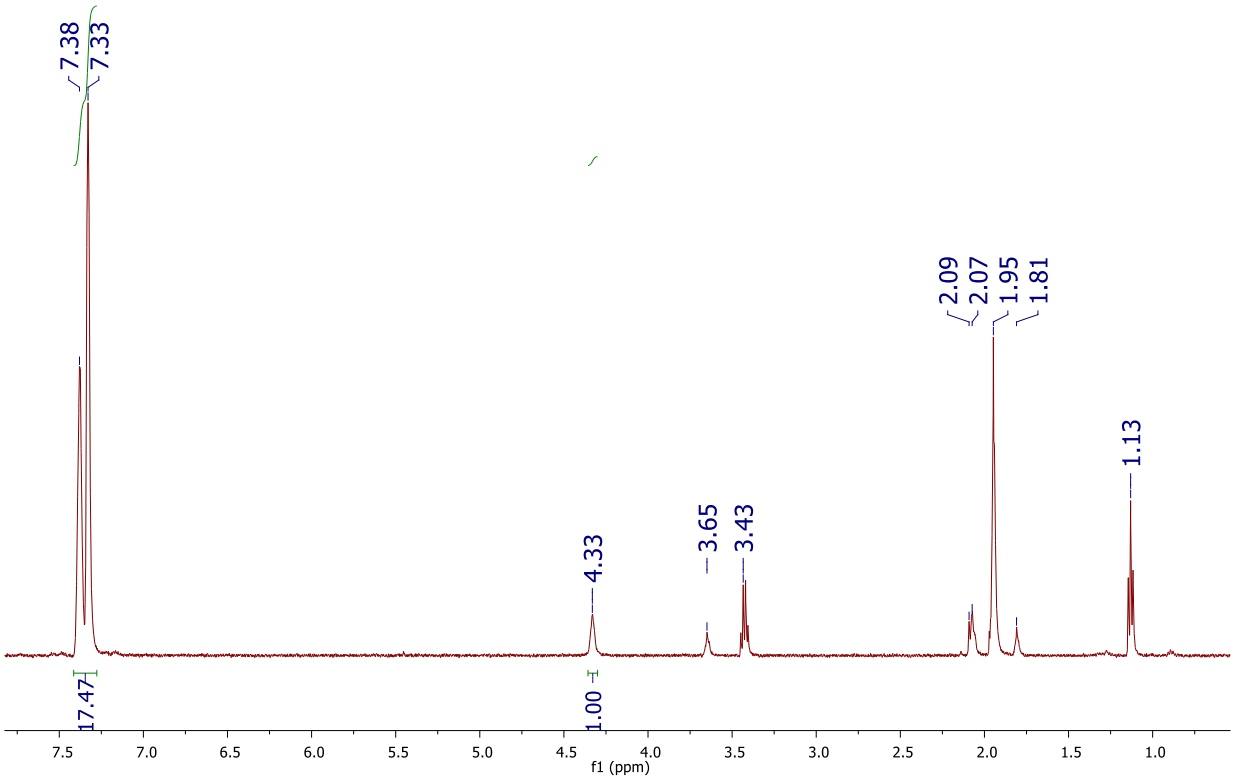

Figure S1. ^{1}H NMR (500 MHz) of bis(diphenylphosphino)amine ligand in CD_3CN synthesized from modified literature procedure[1]. Note: Integration values for solvent impurities were neglected from spectrum.

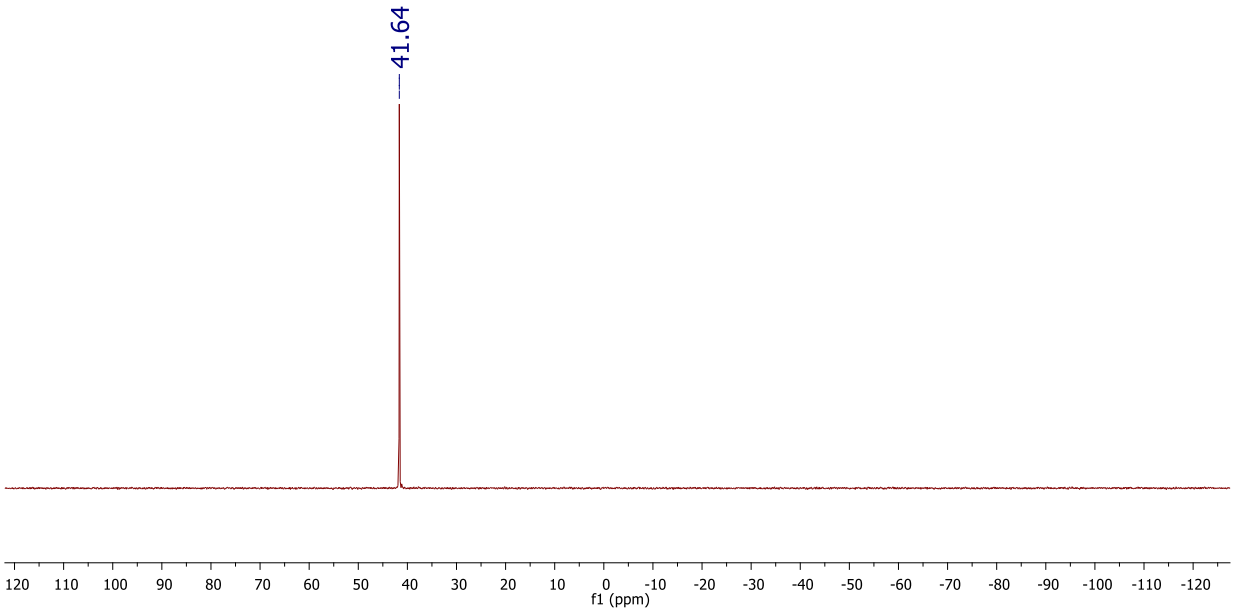

Figure S2. ^{31}P NMR (500 MHz) of bis(diphenylphosphino)amine ligand in CD_3CN synthesized from modified literature procedure[1].

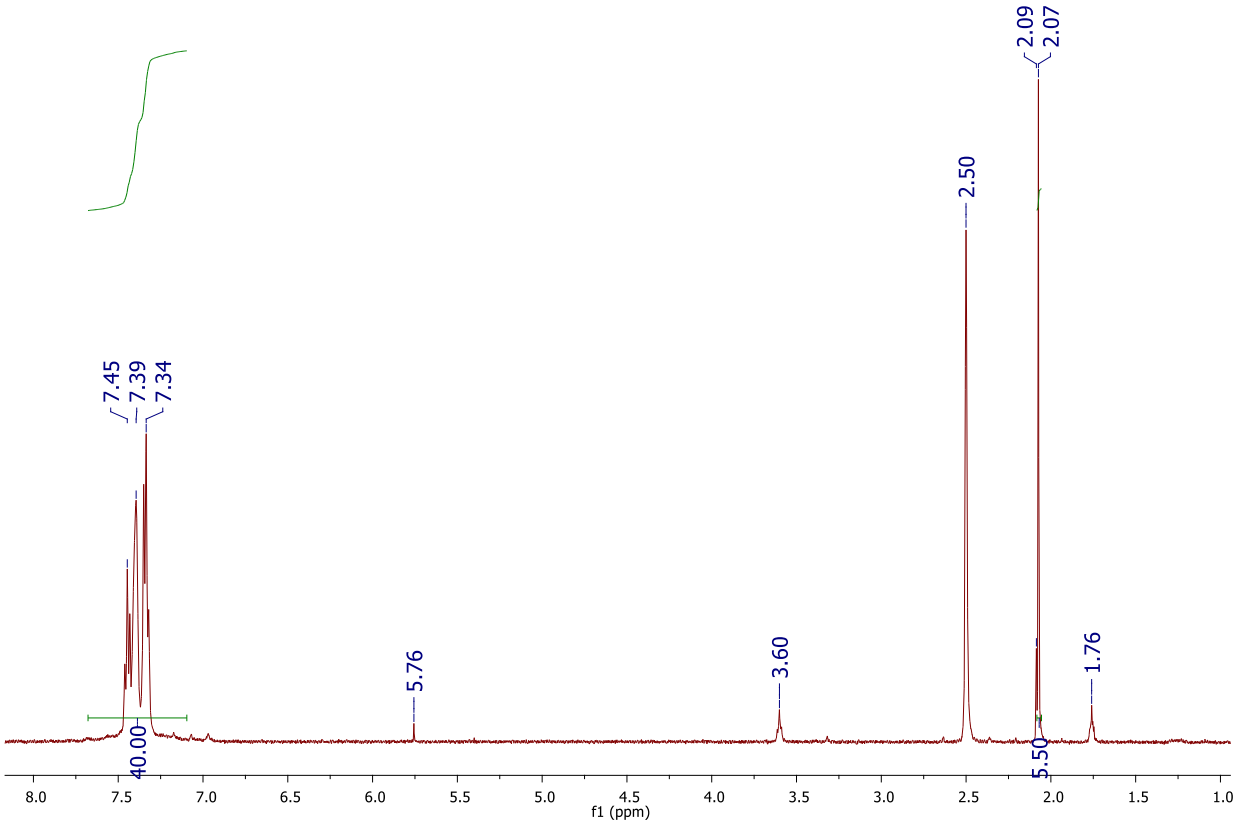

Figure S3. ^{1}H NMR (500 MHz) of $[(\mu_2\text{-dppa})_2Cu_2(MeCN)_2][PF_6]_2$ in DMSO-d_6 synthesized from literature procedure[2]. Calibration of integral for phenyl protons to 40.0 reveals only 2 acetonitrile molecules maximum coordinated to dicopper complex. Note: Integration values for solvent impurities were neglected from spectrum.

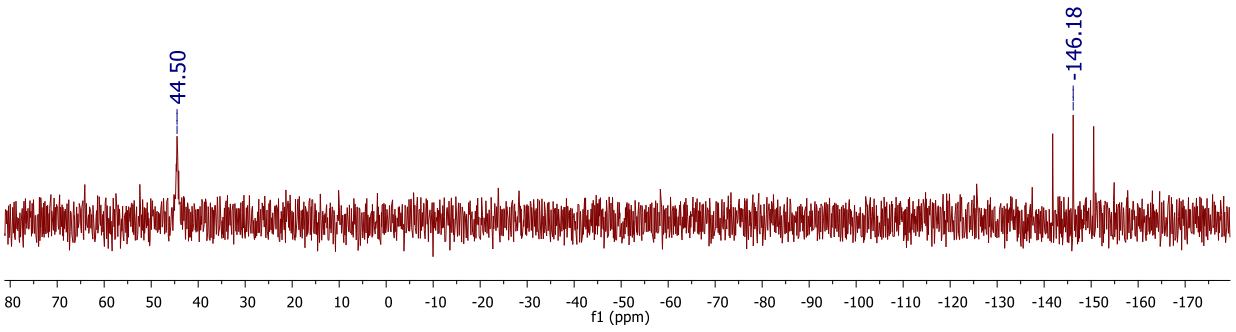

Figure S4. ^{31}P NMR (500 MHz) of $[(\mu_2\text{-dppa})_2Cu_2(MeCN)_2][PF_6]_2$ in CD_3CN synthesized from literature procedure[2].

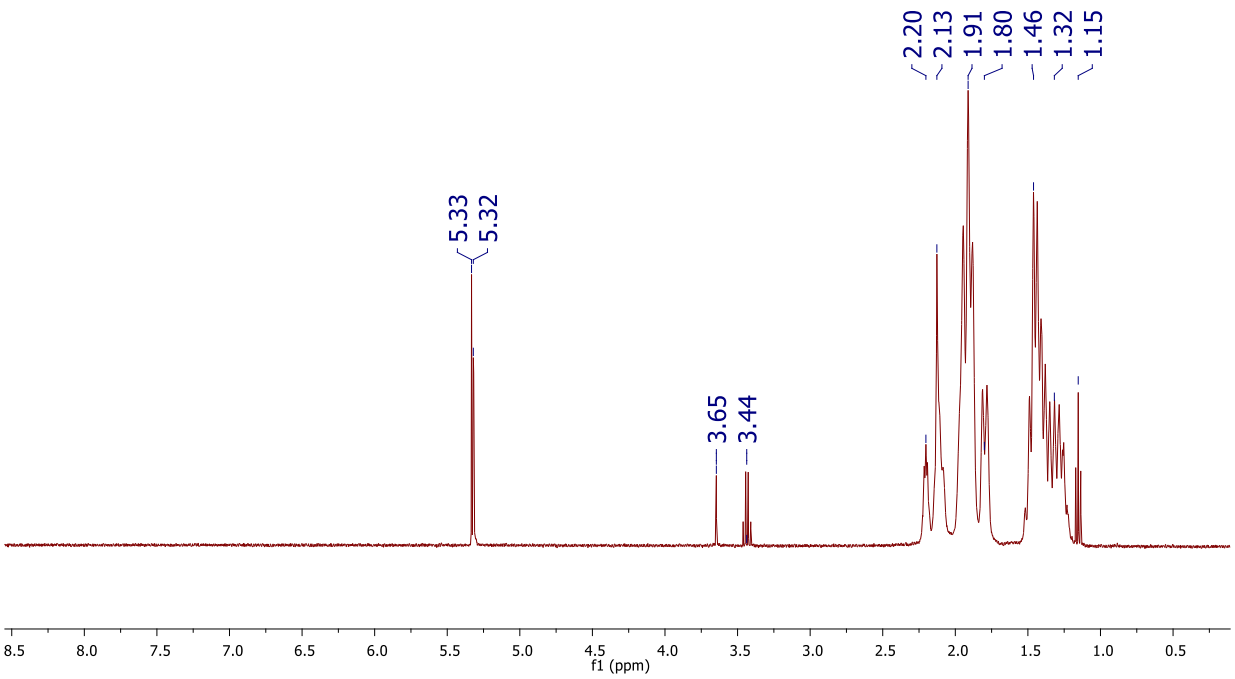

Figure S5. ^{1}H NMR (500 MHz) of $[(\mu_2\text{-dcpm})_2Cu_2][PF_6]_2$ in CD_2Cl_2 synthesized from literature procedure[3]. Note: Some peaks present in spectrum are solvent impurities.

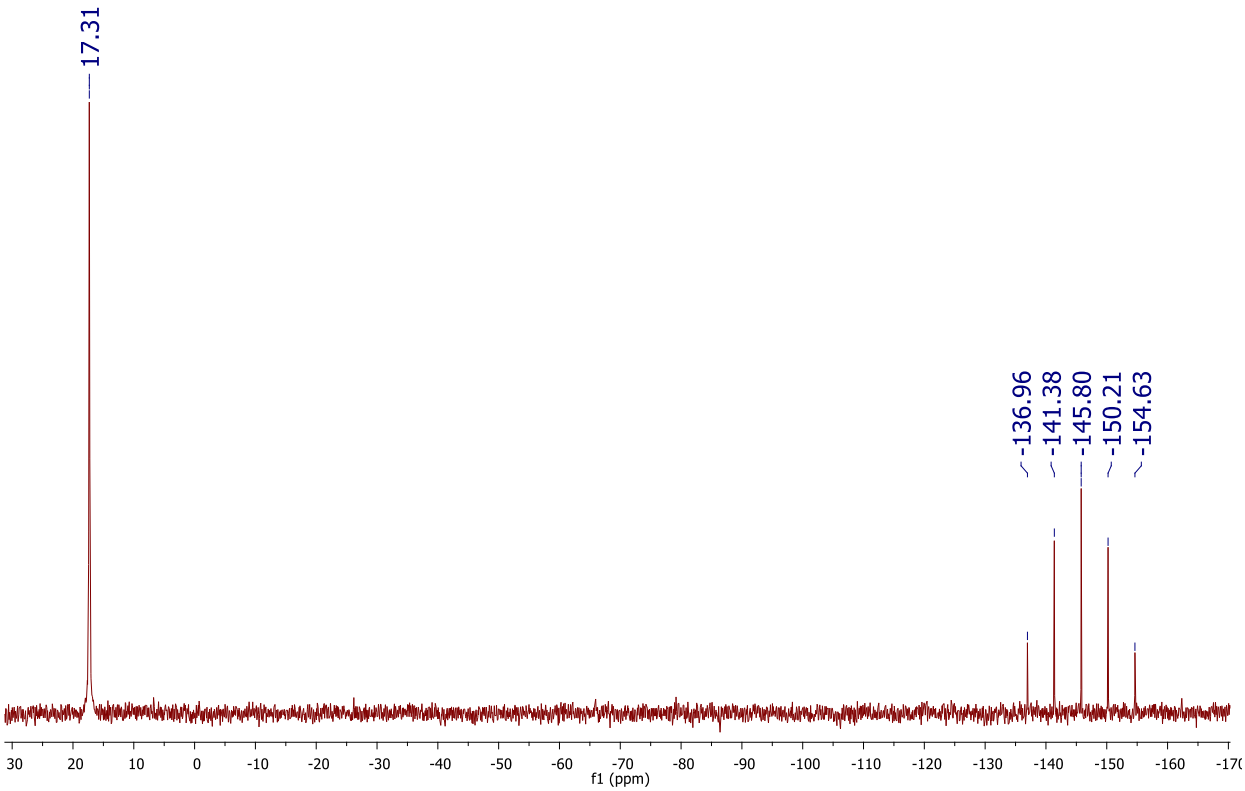

Figure S6. ^{31}P NMR (500 MHz) of $[(\mu_2\text{-dcpm})_2Cu_2][PF_6]_2$ in CD_2Cl_2 synthesized from literature procedure[3].

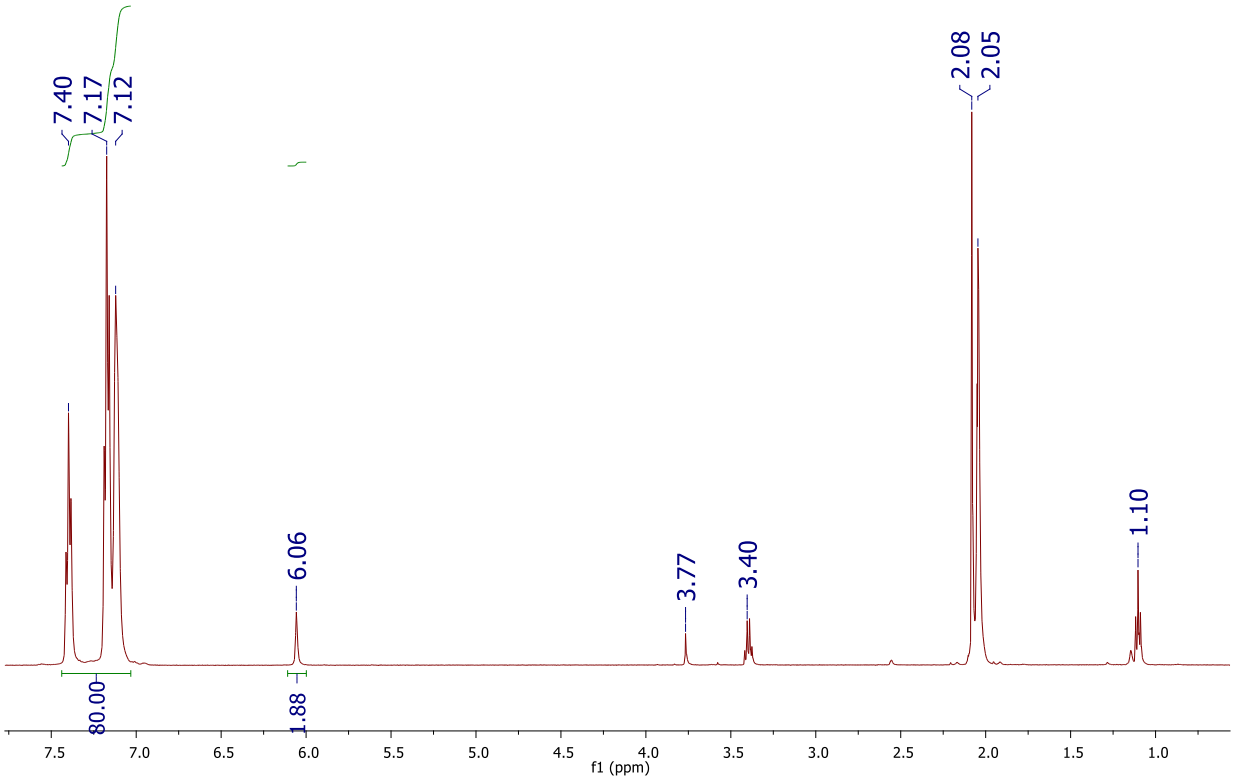

Figure S7. ^{1}H NMR (500 MHz) of **2** in $(CD_3)_2CO$. Note: Integration values for solvent impurities were neglected from spectrum. Peak at 3.77 ppm was not identified as a solvent impurity however it does appear in ^{1}H NMR spectrum of just $(CD_3)_2CO$.

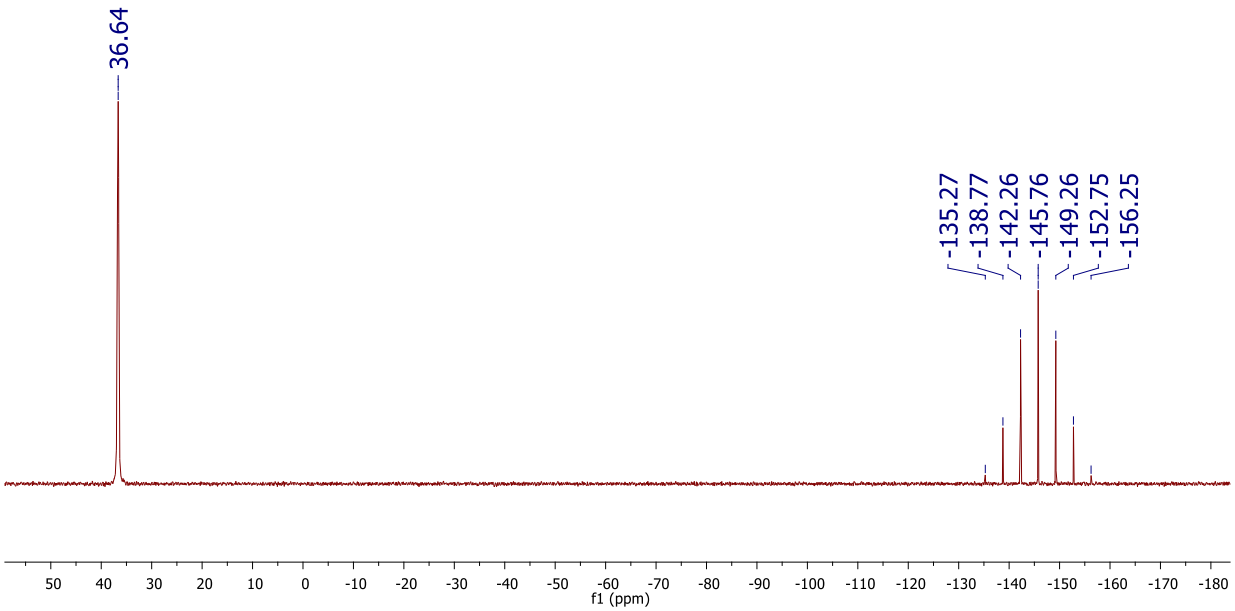

Figure S8. ^{31}P NMR (500 MHz) of **2** in $(CD_3)_2CO$.

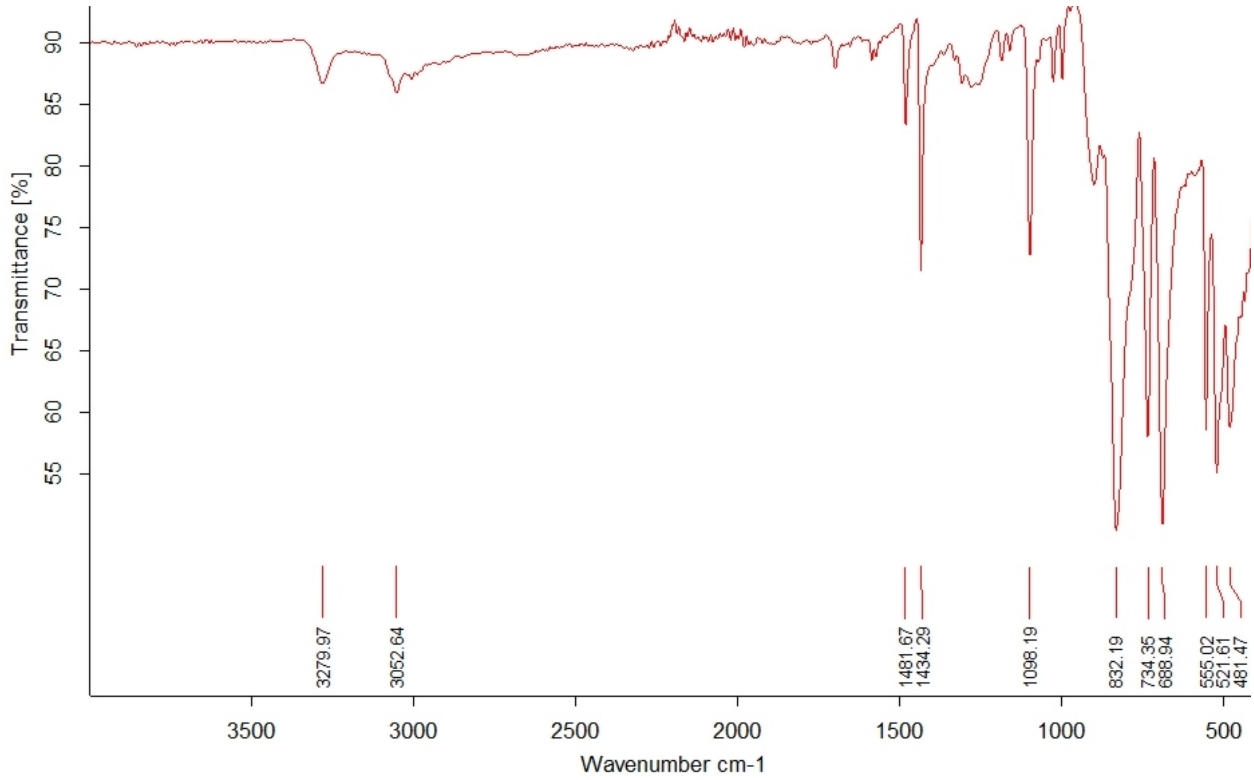

Figure S9. Infrared spectrum of **2**.

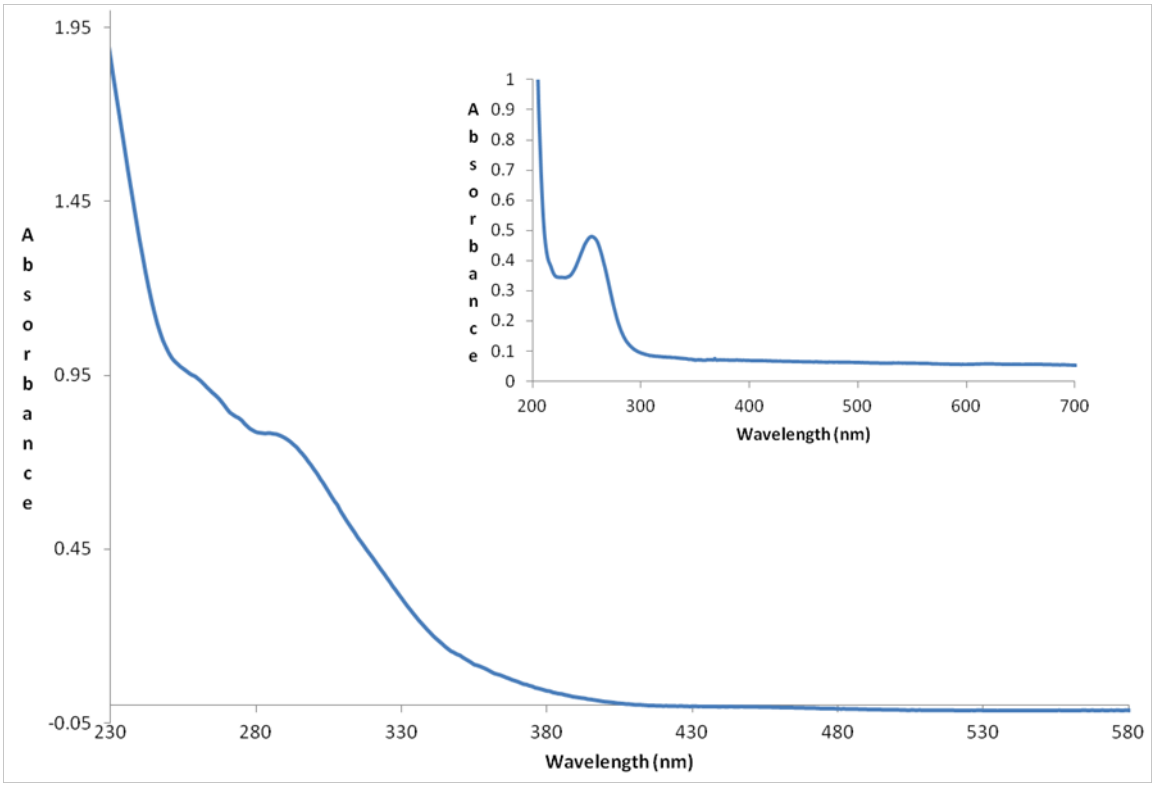

Figure S10. Absorption spectrum of **2** (2 x 10^{-5} M) in MeCN at room temperature. Shoulder appears at 284 nm. Note: Shoulder appearing at ~250 nm is from acetonitrile solvent and not a characteristic property of **2** (inset is MeCN solvent).

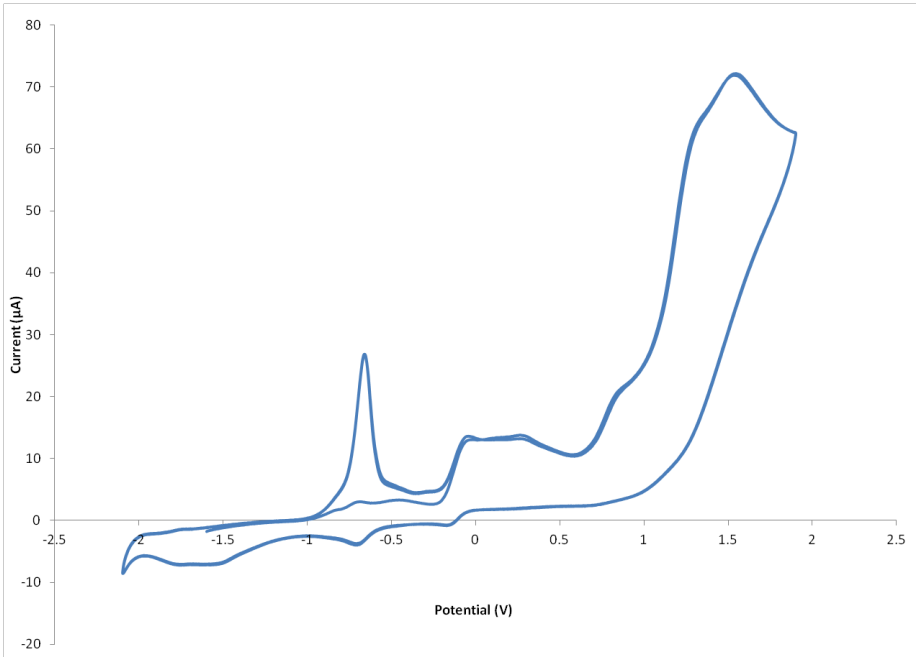

Figure S11. Cyclic voltammogram of **2** (1.88 x 10^{-3} M solution in 0.1 M Bu_4NPF_6/MeCN). Potentials referenced to $FeCp_2^{+/0}$. The large feature at approximately -0.7 V does not appear in the first scan, but only after a complete oxidative scan has been conducted.

Table S1. Cyclic voltammetry parameters used for obtaining CV in Figure S11.

Number of segments	Initial Potential (V)	Initial Direction	Upper Potential (V)	Lower Potential (V)	Final Potential (V)	Sweep Rate (V/s)
5	-1.5	Rising	2	-2	0	0.1

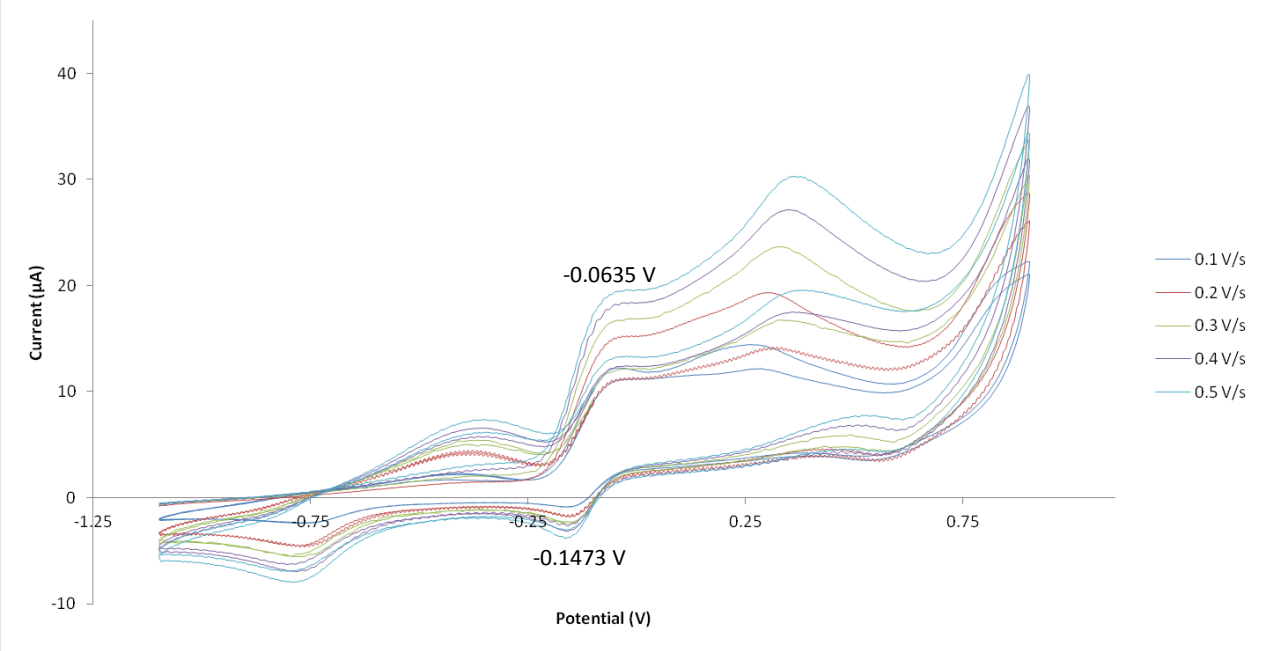

Figure S12. Cyclic votammograms with differing scan rates of **2** (1.88 x 10^{-3} M solution in 0.1 M Bu_4NPF_6/MeCN). Potentials referenced to $FeCp_2^{+/0}$.

Table S2. Cyclic voltammetry parameters used for acquiring CVs in Figure S12.

Number of segments	Initial Potential (V)	Initial Direction	Upper Potential (V)	Lower Potential (V)	Final Potential (V)	Sweep Rate (V/s)
5	-1	Rising	1	-1	0	0.1, 0.2, 0.3, 0.4, 0.5

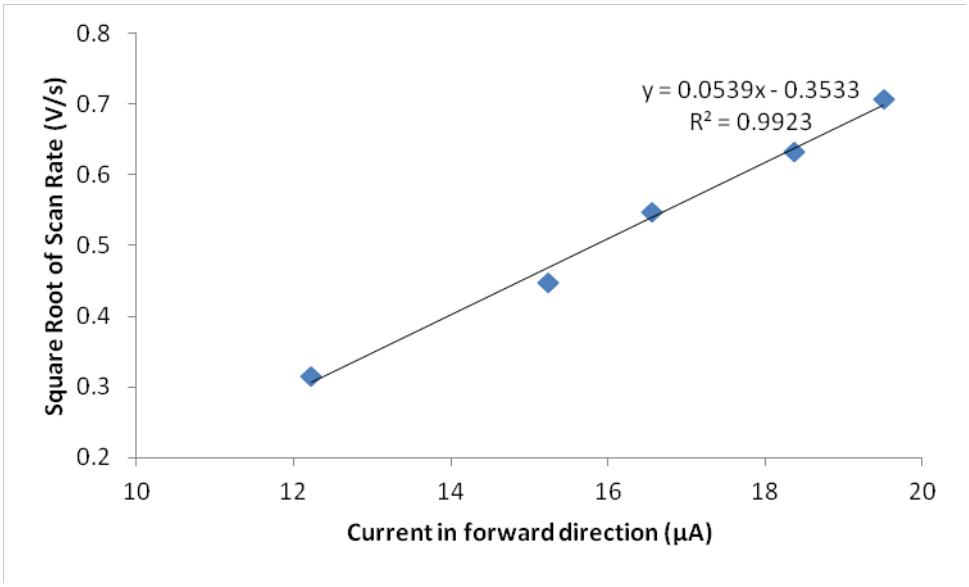

Figure S13. Plot of square root of scan rate vs. current in forward direction, demonstrating the reversibility of the first oxidation for **2**.

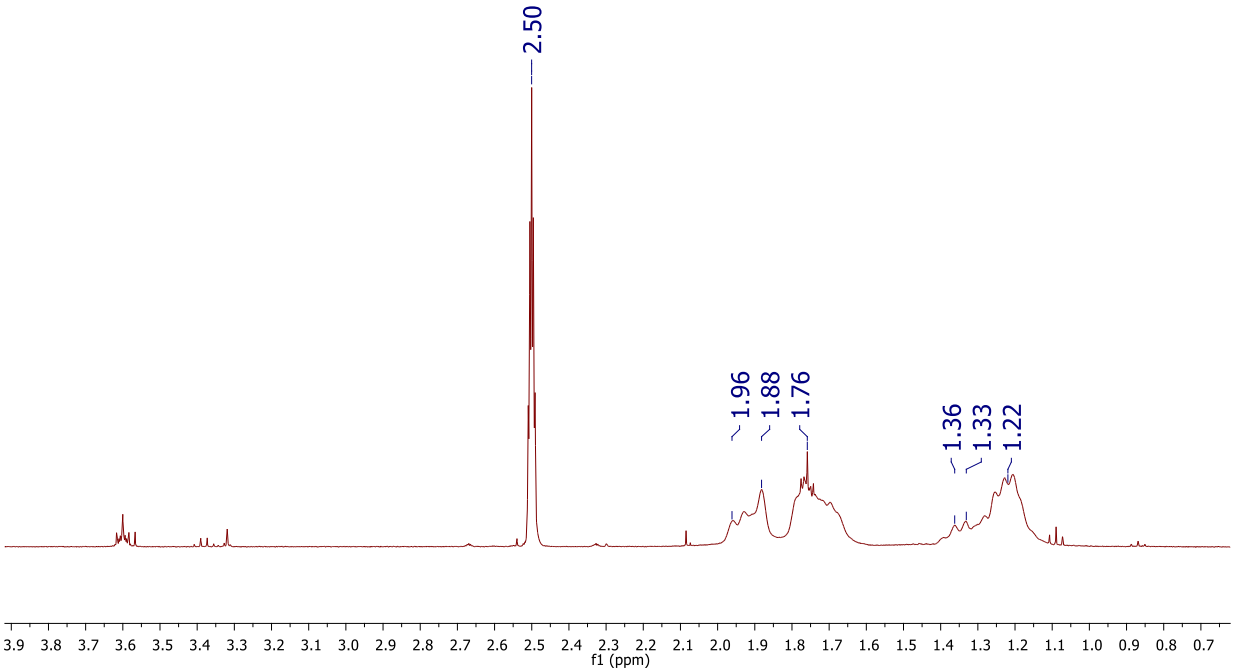

Figure S14. ^{1}H NMR (400 MHz) of **3** in DMSO-d_6. Note: Solvent impurities are not peak picked.

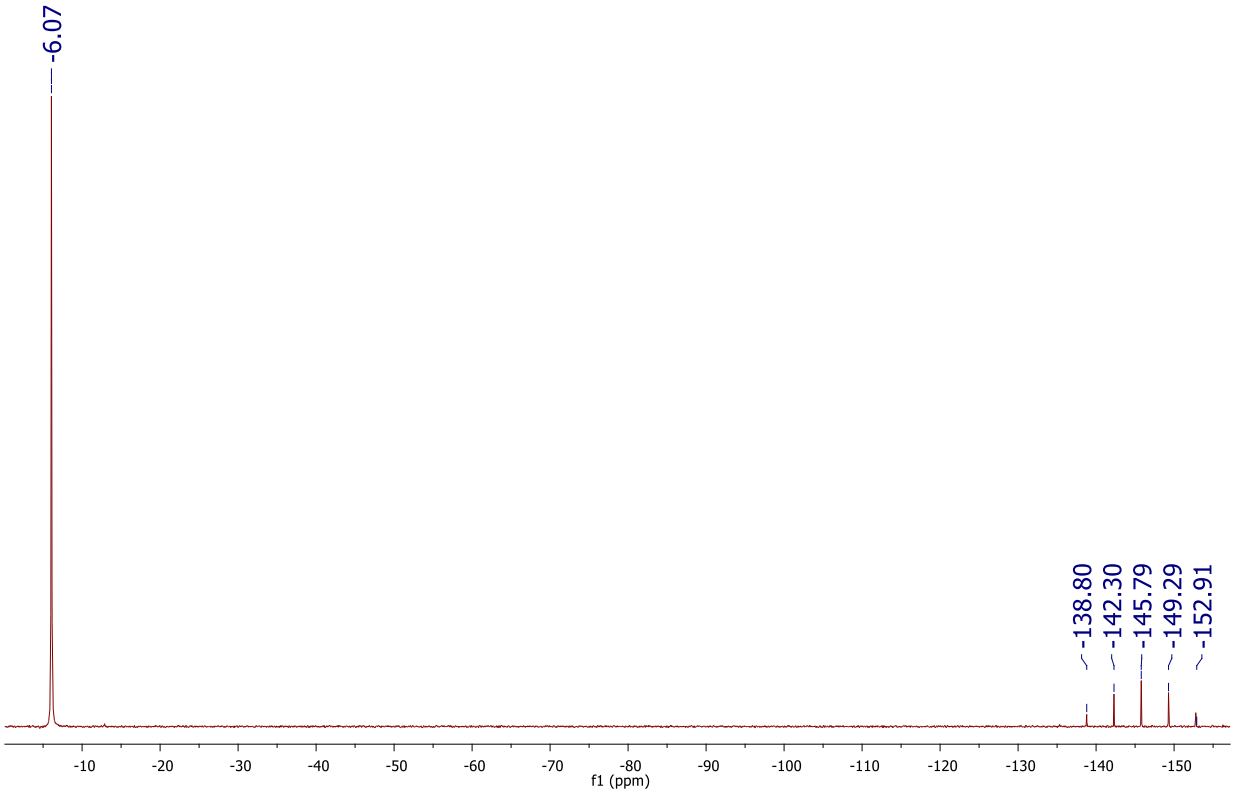

Figure S15. ^{31}P NMR (500 MHz) of **3** in $(CD_3)_2CO$.

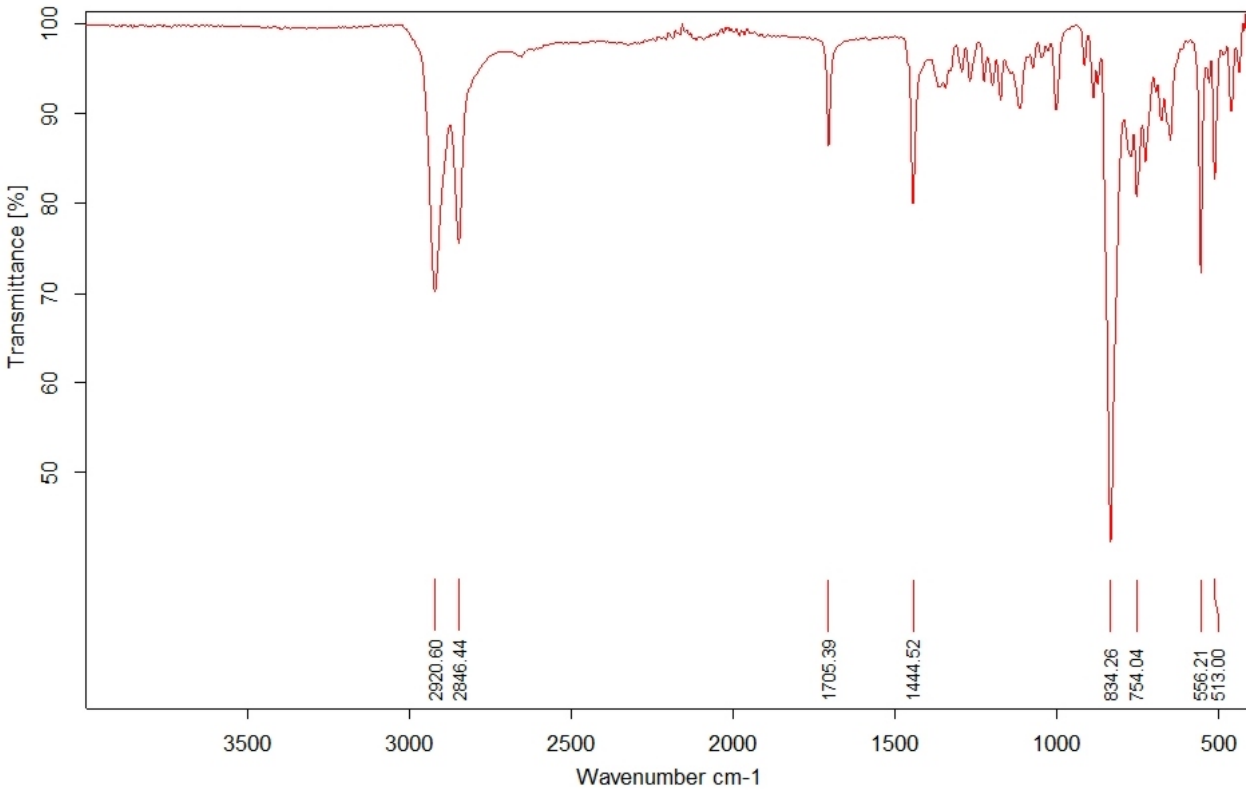

Figure S16. Infrared spectrum of **3**. The feature at 1705 cm^{-1} corresponds to trace acetone.

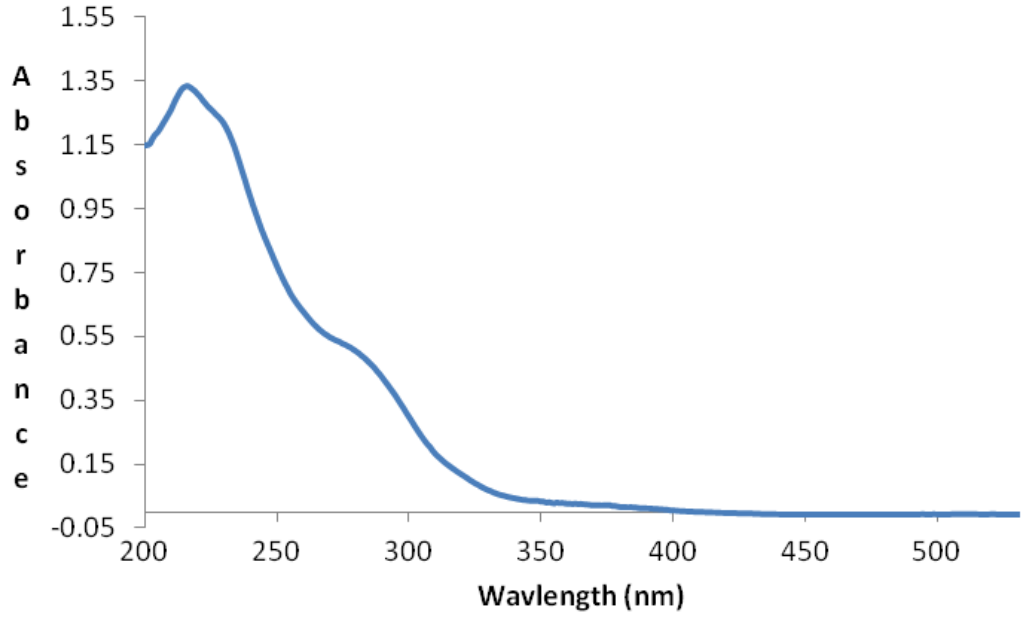

Figure S17. Absorption spectrum of **3** (4.0 x 10^{-5} M) in MeCN at room temperature. Shoulder appears at 279 nm, 229 nm and a peak appears at 216 nm.

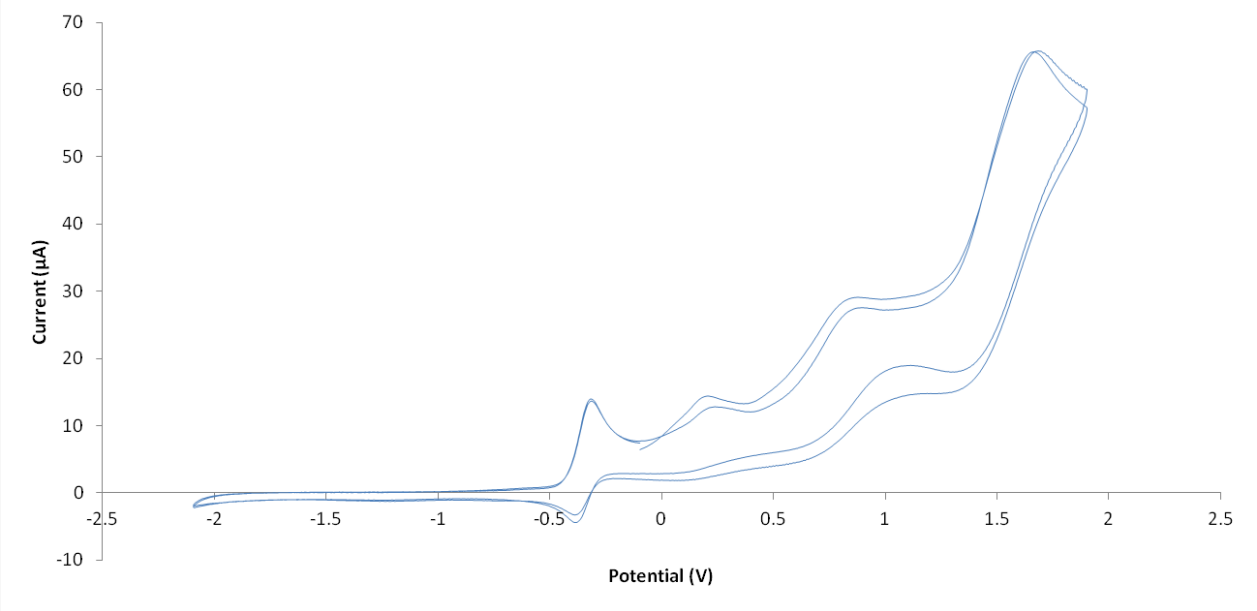

Figure S18. Cyclic voltammogram of **3** (1.88 x 10^{-3} M solution in 0.1 M Bu_4NPF_6/MeCN) solution. Potentials referenced to $FeCp_2^{+/0}$.

Table S3. Cyclic voltammetry parameters used for obtaining CV in Figure S18.

Number of segments	Initial Potential (V)	Initial Direction	Upper Potential (V)	Lower Potential (V)	Final Potential (V)	Sweep Rate (V/s)
5	0	Rising	2	-2	0	0.1

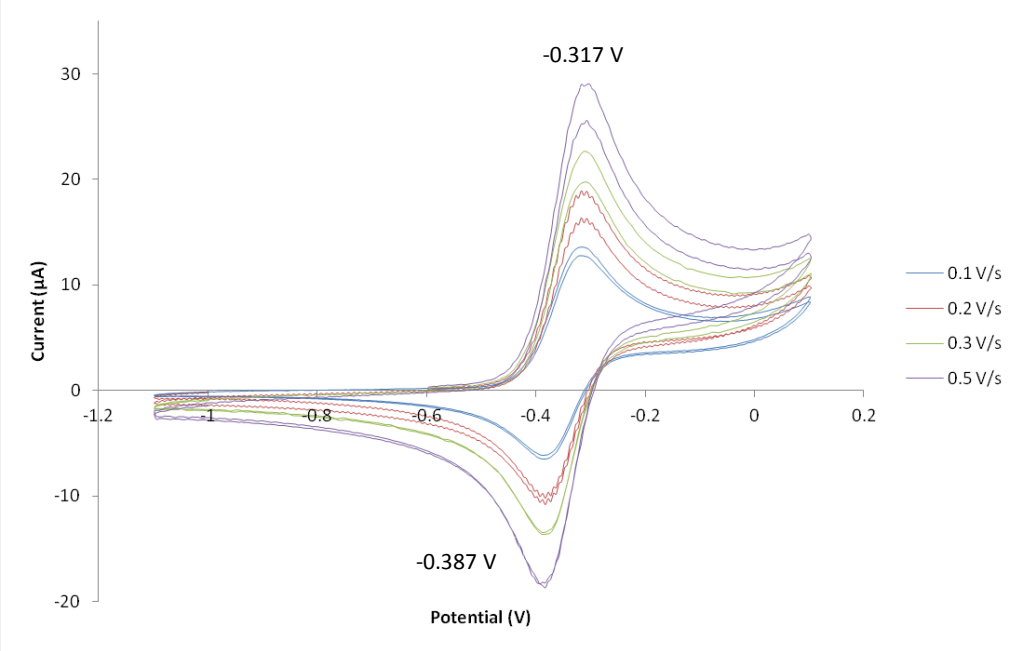

Figure S19. Cyclic votammograms with differing scan rates of **3** (1.88 x 10^{-3} M solution in 0.1 M Bu_4NPF_6/MeCN). Potentials referenced to $FeCp_2^{+/0}$.

Table S4. Cyclic voltammetry parameters for acquiring CVs in Figure S19.

Number of segments	Initial Potential (V)	Initial Direction	Upper Potential (V)	Lower Potential (V)	Final Potential (V)	Sweep Rate (V/s)
5	-0.5	Rising	0.2	-1	-0.9	0.1, 0.2, 0.3, 0.4, 0.5

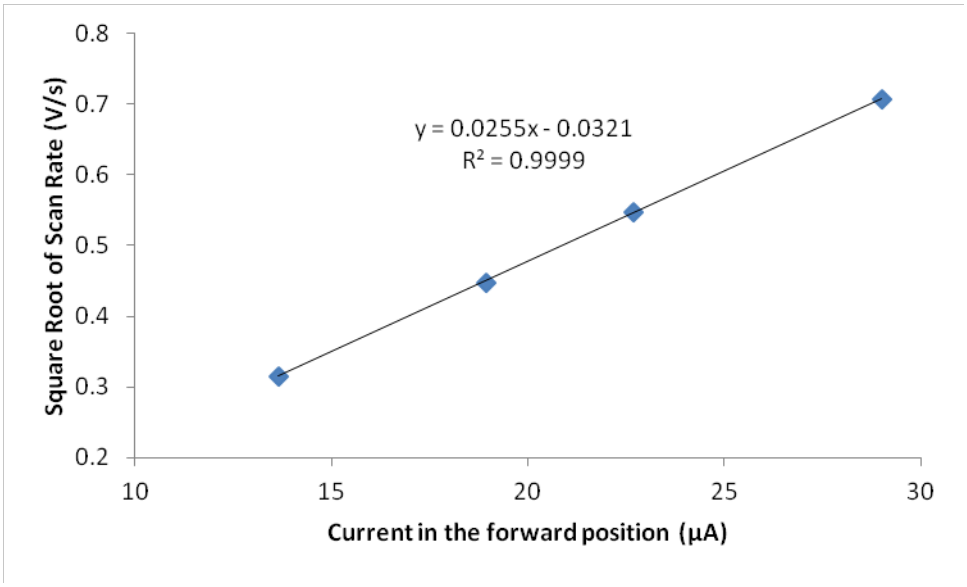

Figure S20. Plot of square root of scan rate vs. current in forward direction, demonstrating the reversibility of the first oxidation for **3**.

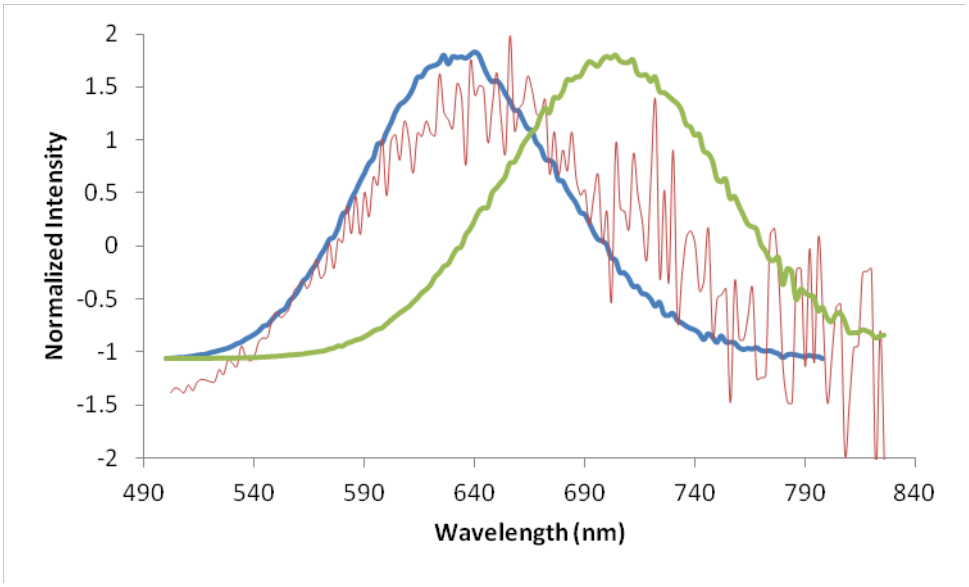

Figure S21. Normalized emission spectra for compounds **1** (blue trace), **2** (green trace) and **3** (red trace) using 415 nm as the excitation wavelength in all cases. Each plot was normalized independently, and the poor signal to noise ratio for **3** results for weak emission below the normal detection limit of the instrument.

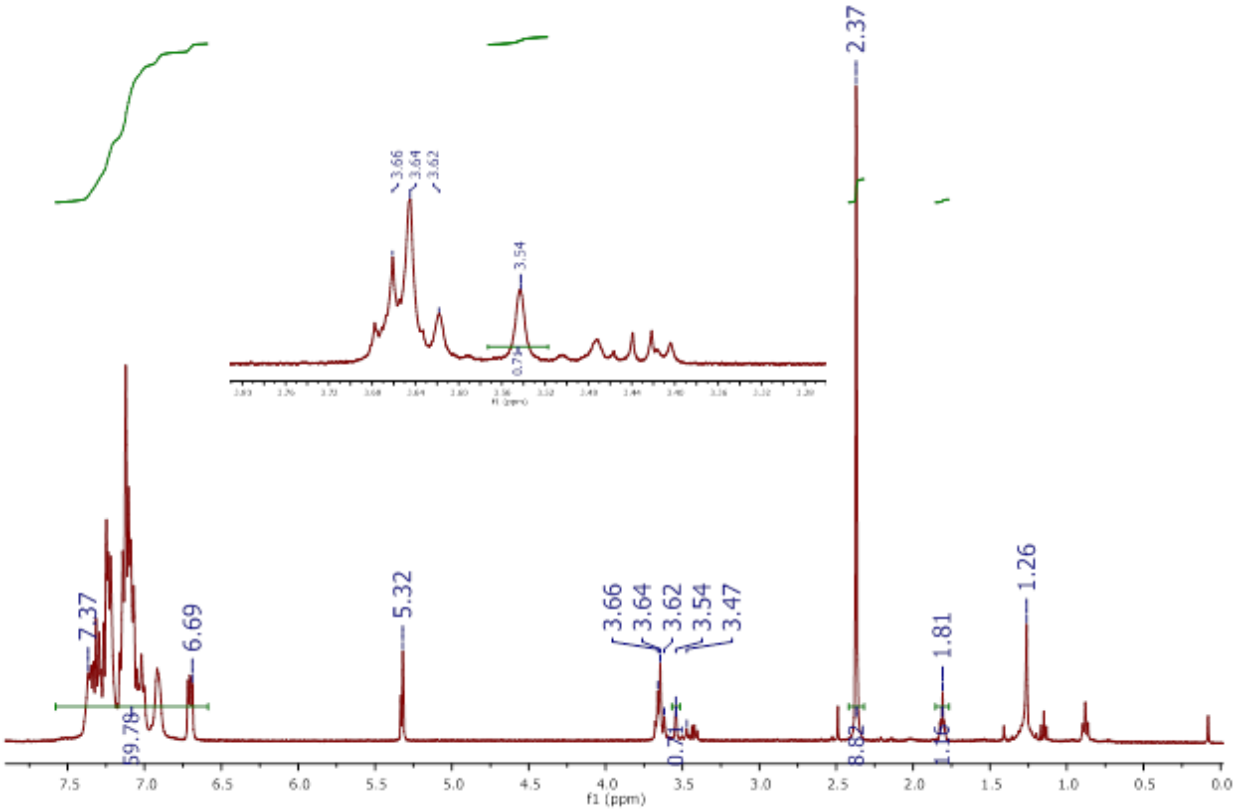

Figure S22. ^{1}H NMR (400 MHz) of reaction mixture of **2** and excess NaN_3 in CD_2Cl_2 with tri(*o*-tolyl)phosphine as the internal standard. Peak at 3.62 ppm is unreacted **2**. Integration values for **2, 2'** and coordinated THF molecules at 3.66 ppm could not be determined due to spectral peak overlap (see spectra inset).

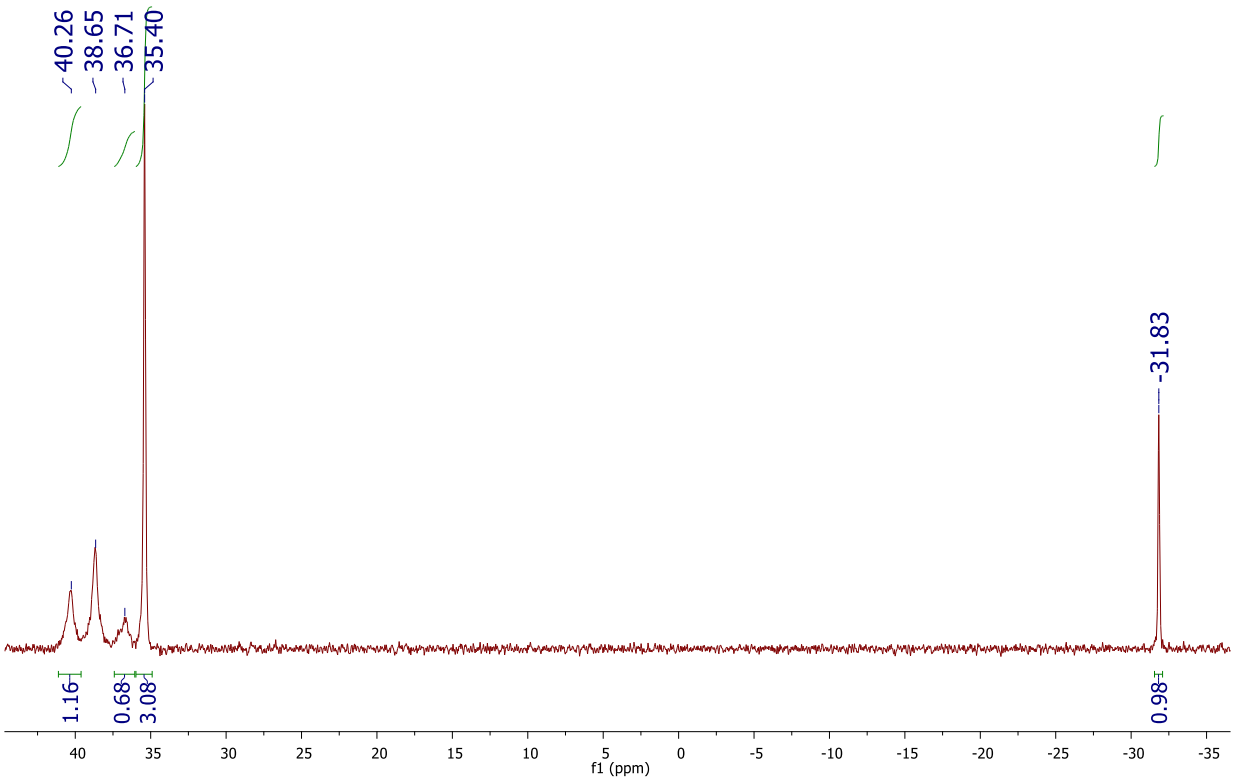

Figure S23. ^{31}P NMR (400 MHz) of reaction mixture of **2** and excess NaN_3 in CD_2Cl_2 with tri(*o*-tolyl)phosphine as the internal standard. Anion (PF_6^-) at -146.1 ppm is omitted from spectra.

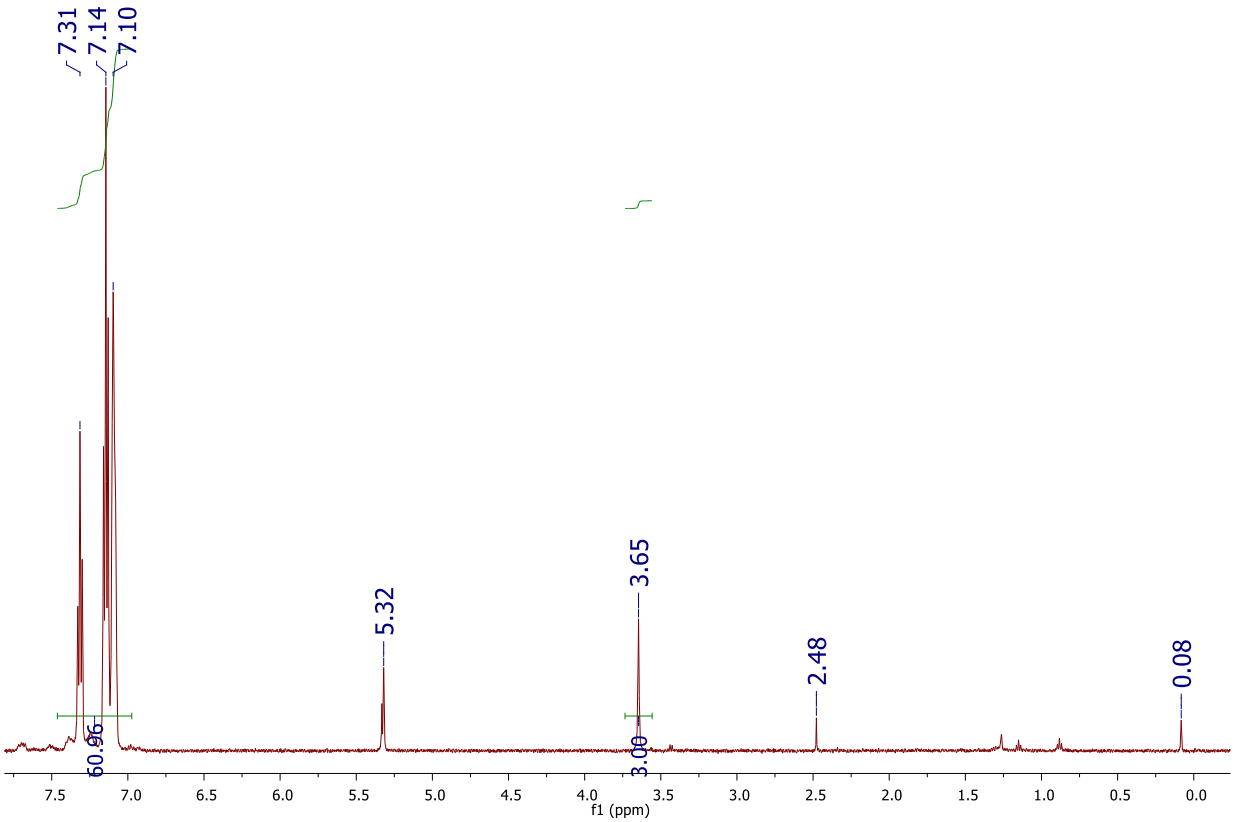

Figure S24. ^{1}H NMR (400 MHz) of **4** from N_3SiMe_3 in CD_2Cl_2. Note: Integration values for solvent impurities were neglected from spectrum. Peak at 2.48 ppm is unknown as a solvent but is predicted to be an impurity in NMR tube because of its reoccurrence in other, different experimental spectra.

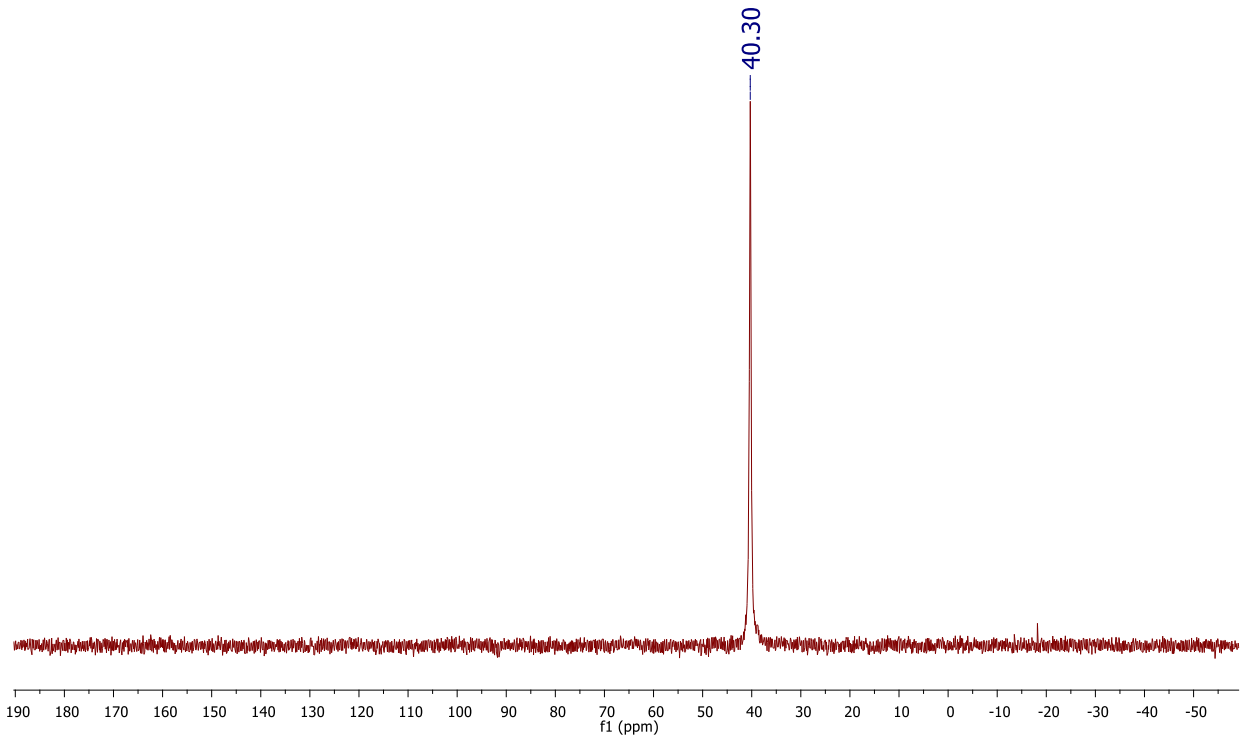

Figure S25. ^{31}P NMR (400 MHz) of **4** from N_3SiMe_3 in CD_2Cl_2. Anion (PF_6^-) at -146.1 ppm omitted from spectra.

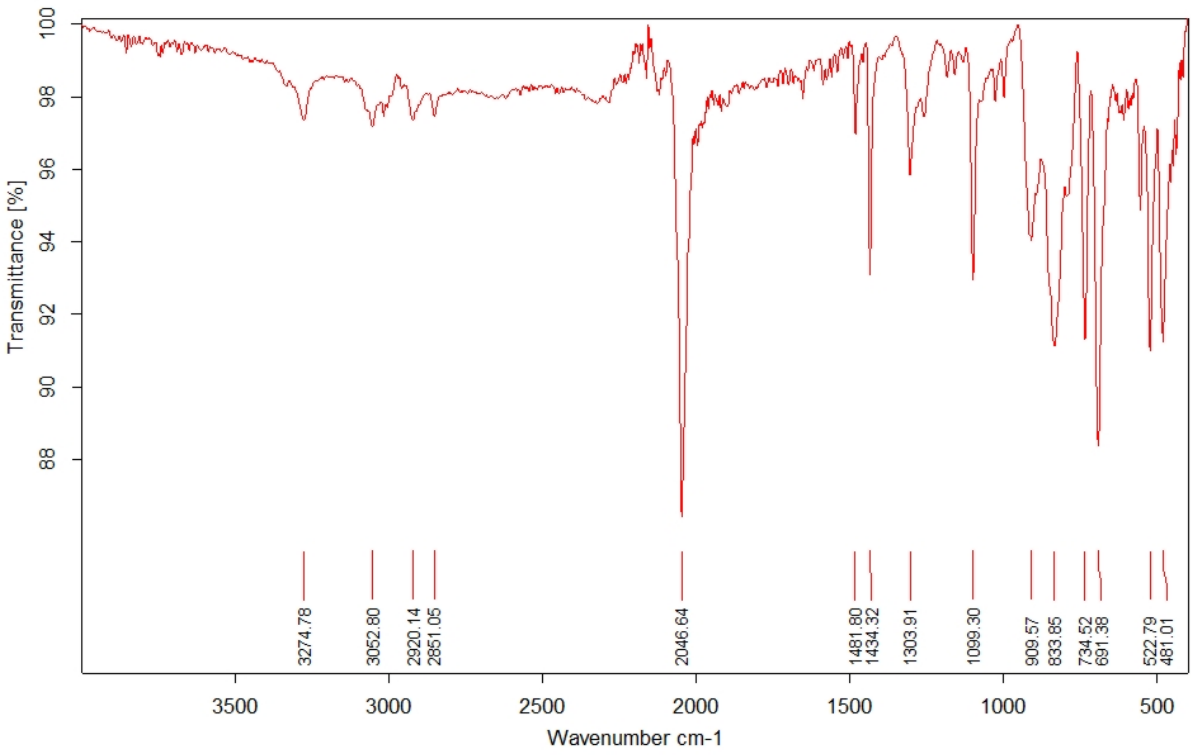

Figure S26. Infrared spectrum of **4**.

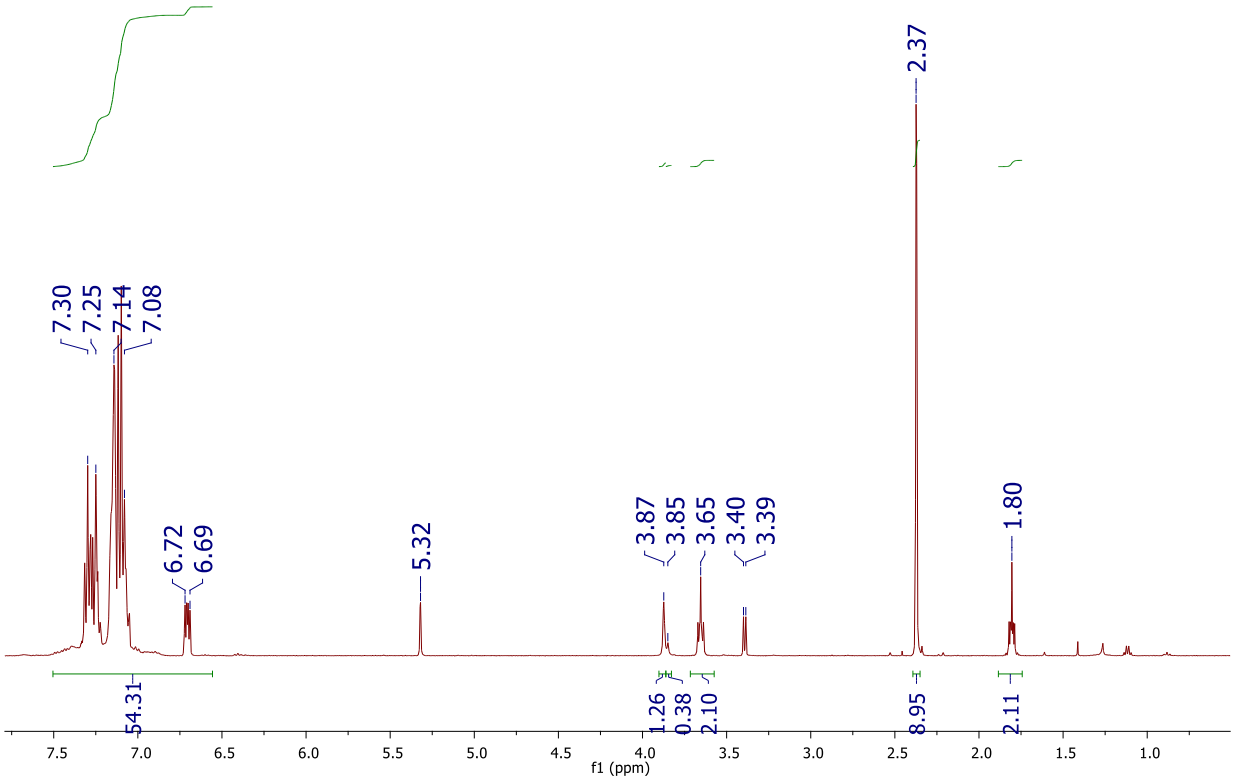

Figure S27. ^{1}H NMR (400 MHz) of reaction mixture of **2** and excess NaI in CD_2Cl_2 with tri(*o*-tolyl)phosphine as the internal standard. Doublet appearing at 3.40 ppm is unknown.

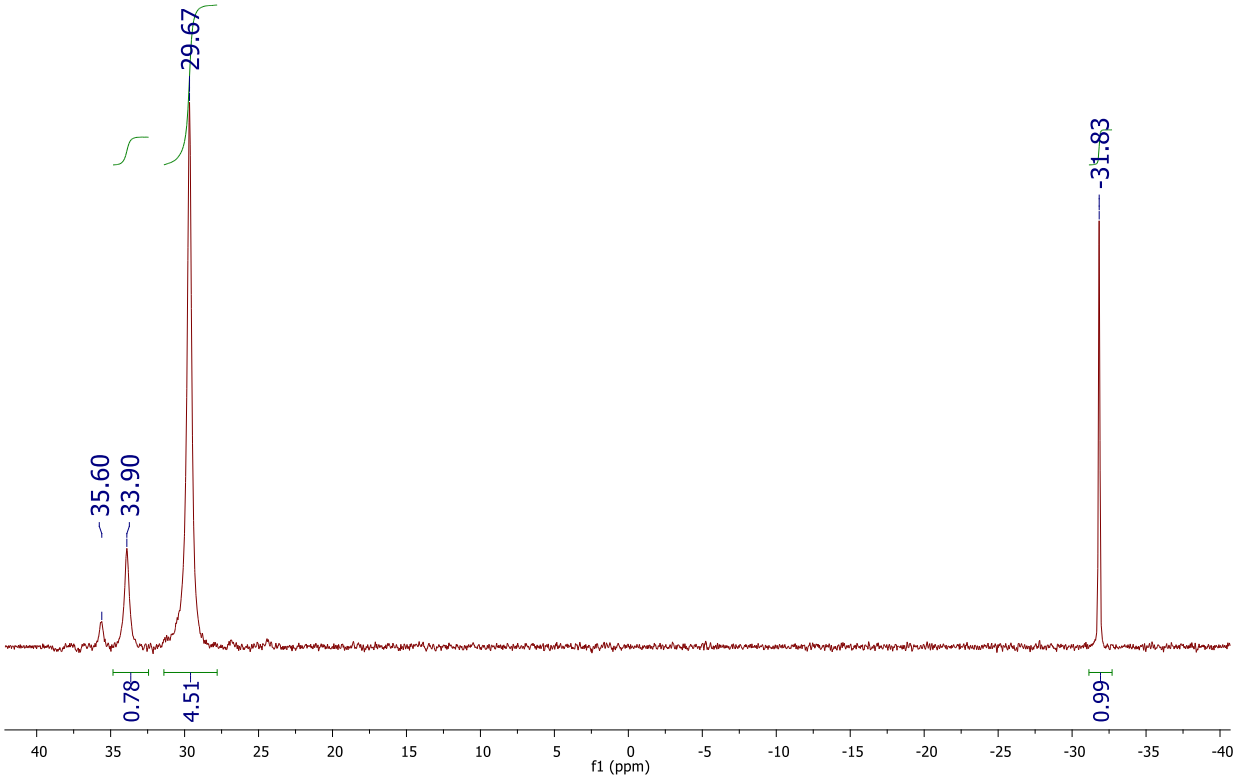

Figure S28. ^{31}P NMR (400 MHz) of reaction mixture of **2** and excess NaI in CD_2Cl_2 with tri(*o*-tolyl)phosphine as the internal standard.

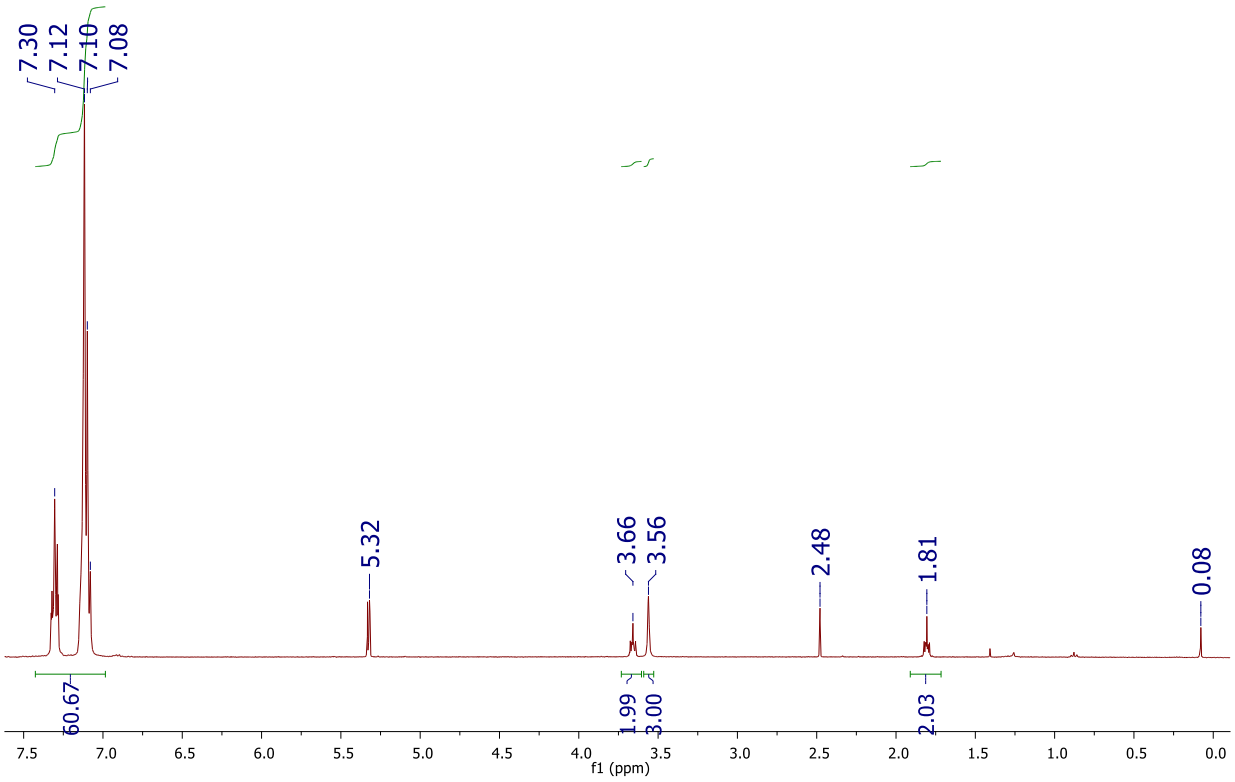

Figure S29. ^{1}H NMR (400 MHz) of isolated **6** in CD_2Cl_2. Peak at 2.48 ppm is unknown as a solvent impurity but is predicted to be an impurity in NMR tube because of its reoccurrence in other, different experimental spectra.

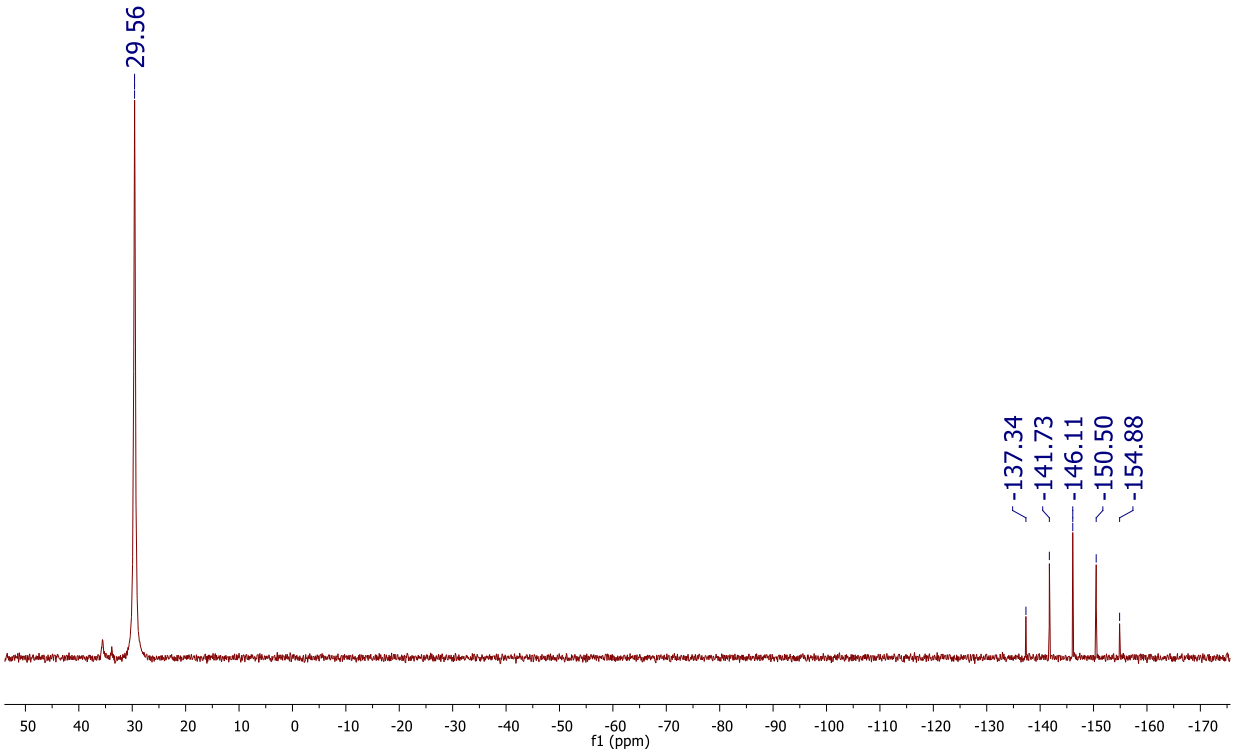

Figure S30. ^{31}P NMR (400 MHz) in CD_2Cl_2 of isolation of **6** by toluene extraction.

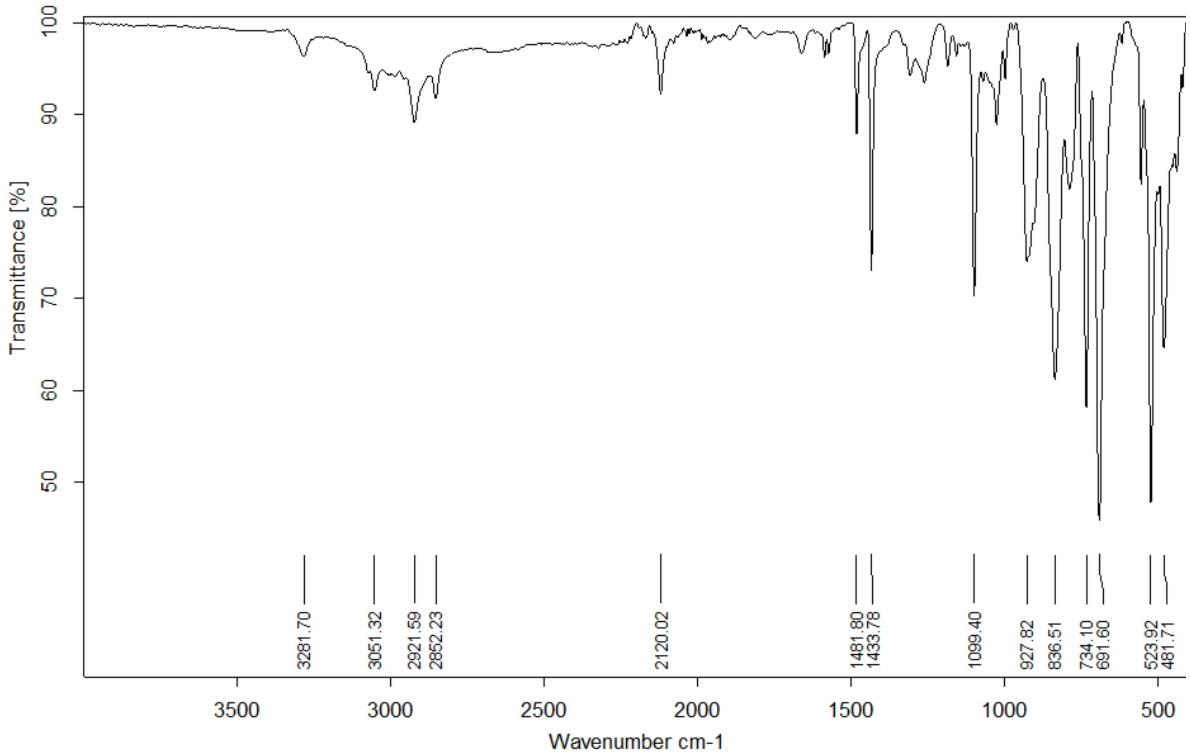

Figure S31. Infrared spectrum of **6**.

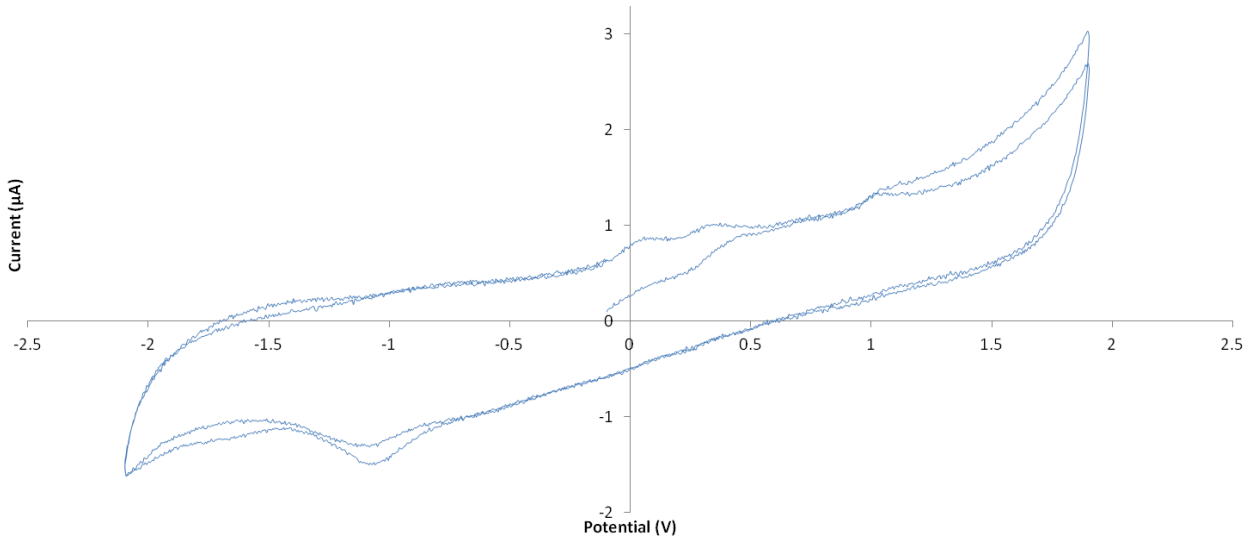

Figure S32. Cyclic voltammogram of 0.1 M Bu_4NPF_6/MeCN electrolyte solution used in CV measurements of **2** and **3**. Potentials referenced to $FeCp_2^{+/0}$. Irreversible oxidations occurring at 0.032 V, 0.33 V, 1.02 V and a irreversible reduction at -1.09 V.

Table S5. Cyclic voltammetry parameters for acquiring CVs in Figure S32.

Number of segments	Initial Potential (V)	Initial Direction	Upper Potential (V)	Lower Potential (V)	Final Potential (V)	Sweep Rate (V/s)
5	0	Rising	2	-2	0	0.1

Experimental conditions: Competition reaction between NaI/ NaN_3 with **2**

A solution of **2** (0.015 g, 0.0071 mmol) in THF (approximately 1 mL) was vacuum evaporated extensively to remove any coordinated acetone molecules. Once **2** appeared free of acetone by ^{1}H NMR, it was dissolved again in 1 mL of THF. In a separate vessel, NaI (0.0053 g, 0.035 mmol) was dissolved in MeOH (approximately 1 mL). Solution of NaI was then added to NaN_3 (0.0023 g, 0.035 mmol) and then added to **2** dropwise, at room temperature with stirring. Solution continued stirring overnight at room temperature and the resulting color was a darker orange with no obvious precipitate. Solution was completed evaporated by vacuum.

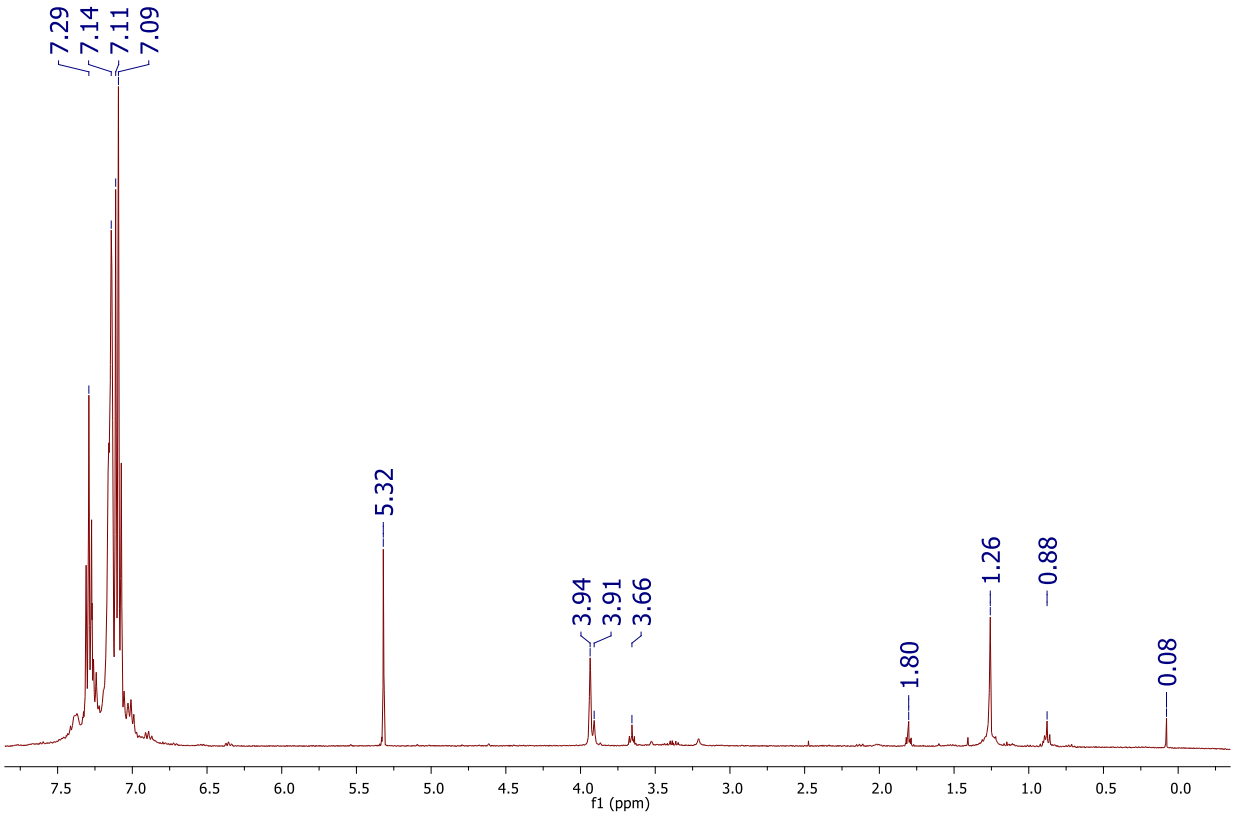

Figure S33: ^{1}H NMR (400 MHz) of products from competition experiment between NaI/NaN_3 and **2** in CD_2Cl_2.

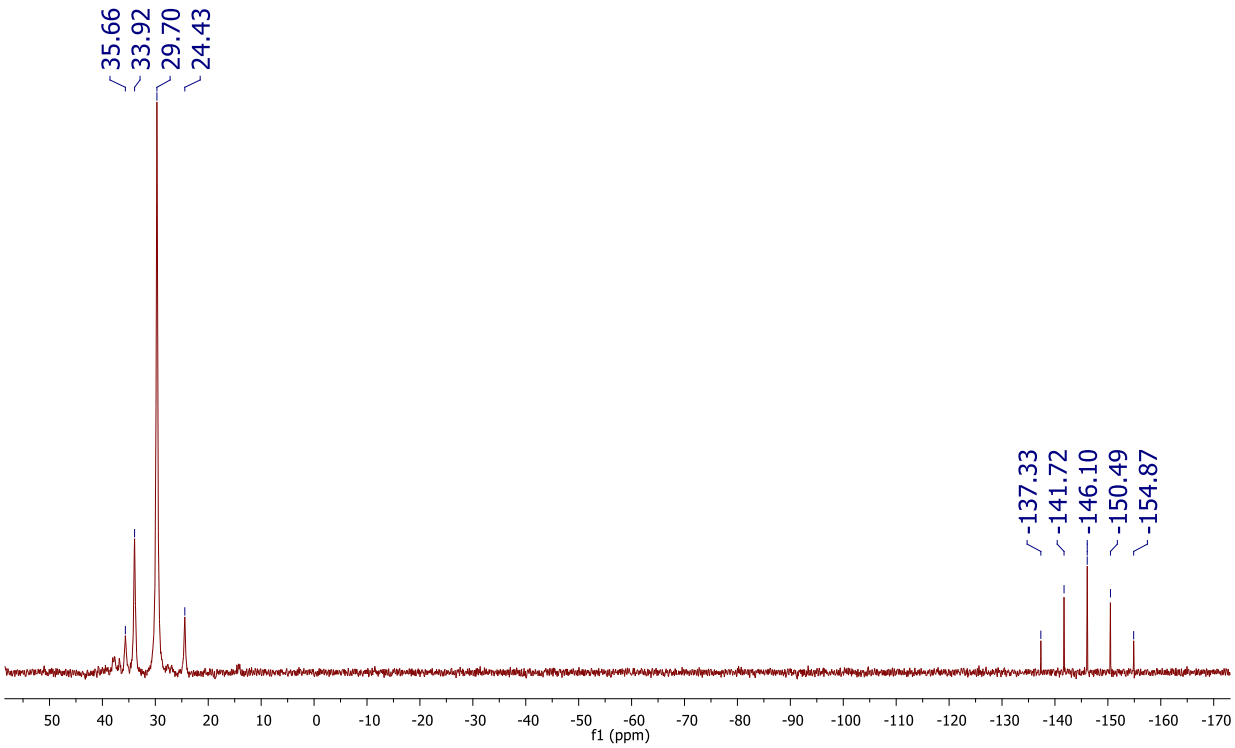

Figure S34: ^{31}P NMR (400 MHz) of products from competition experiment between NaI/NaN_3 and **2** in CD_2Cl_2.

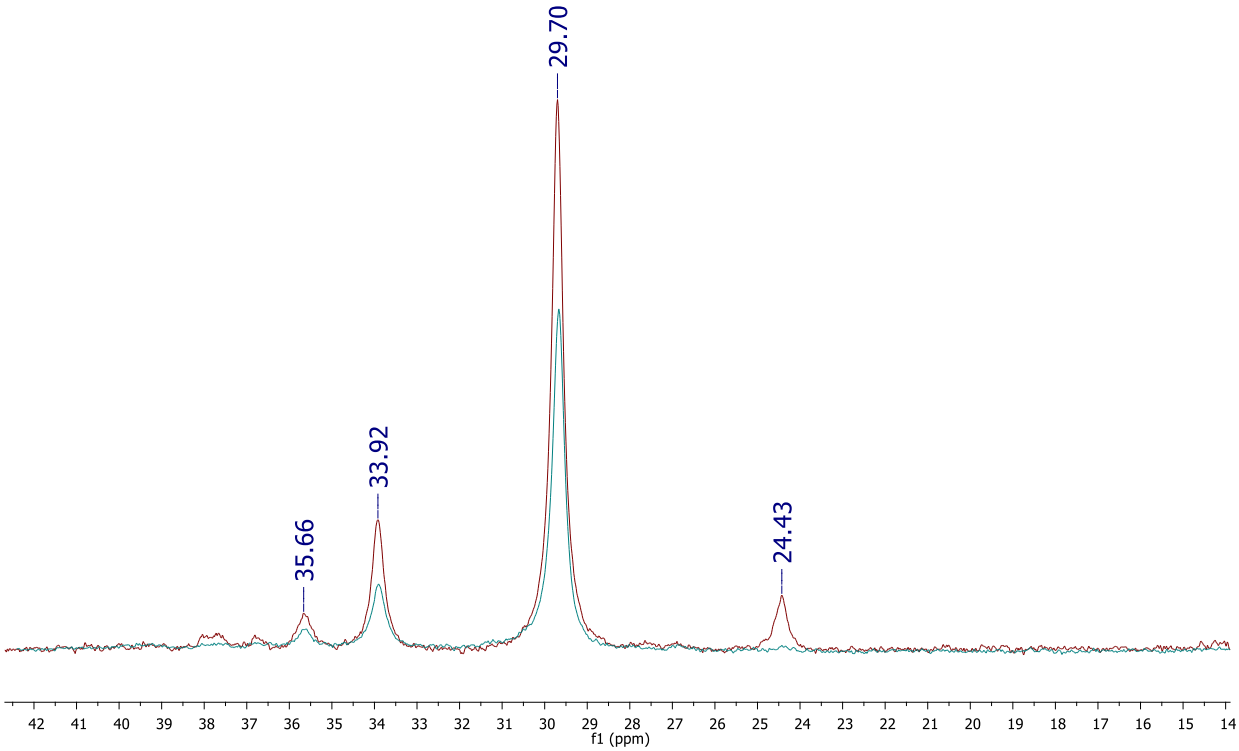

Figure S35. ^{31}P NMR (400 MHz) of Figure S34 (red trace) and Figure S28 (blue trace). Peak at 24.43 ppm is unknown but is sometimes seen during purification attempts in the reaction between **2** and excess NaI as a minor impurity.

Experimental conditions: Reaction of **4** with excess NaI

To a solution of **4** (0.0052 g, 0.0029 mmol) in THF (approximately 1-2 mL), NaI (0.0049 g, 0.032 mmol) in 1 mL of MeOH was added dropwise with stirring at room temperature. Once all the NaI solution was added, a small white precipitate (presumably NaN_3) was observed. Solution continued stirring overnight at room temperature and the resulting solution appeared to have no obvious precipitate. Solution was completed evaporated by vacuum, dissolved in CD_2Cl_2 and was pipette filtered through Celite for NMR sample.

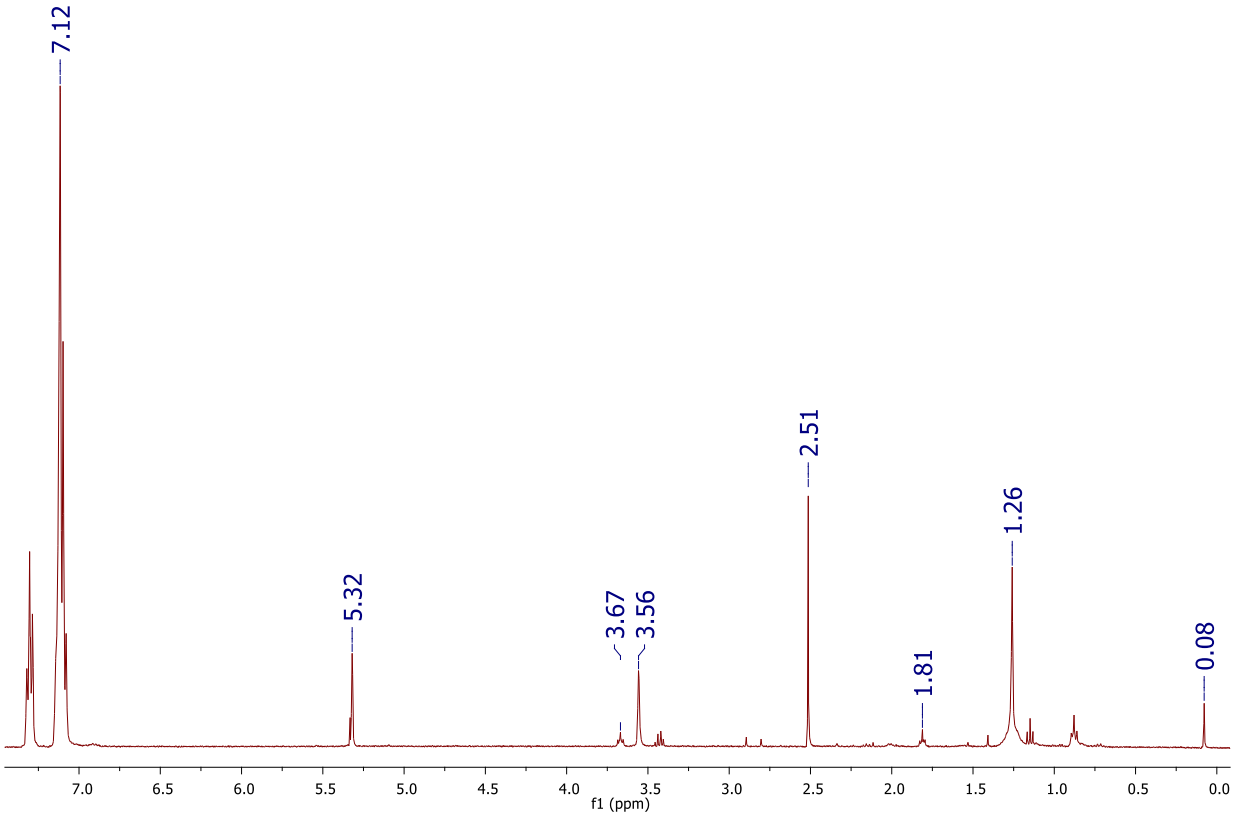

Figure S36. ^{1}H NMR (400 MHz) of resulting mixture of **4** and excess NaI in CD_2Cl_2.

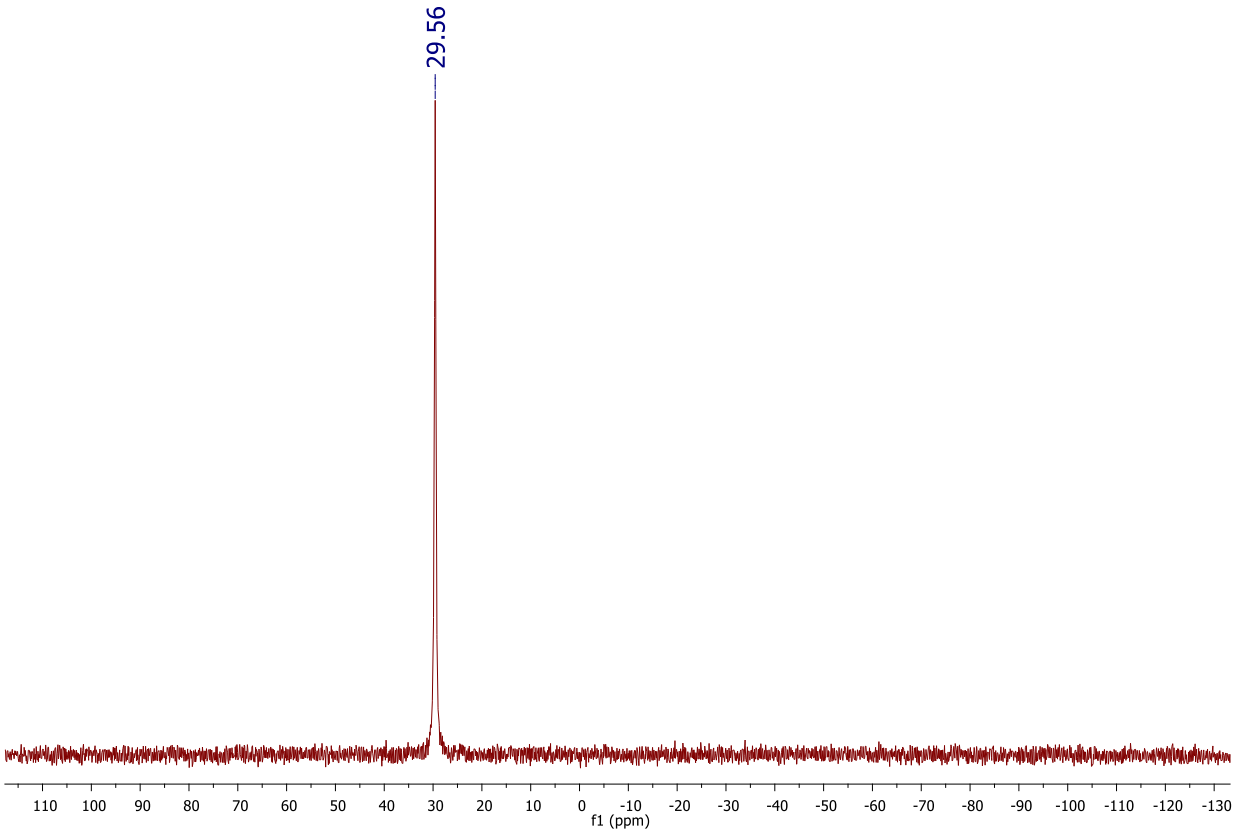

Figure S37. ^{31}P NMR (400 MHz) of resulting mixture of **4** and excess NaI in CD_2Cl_2. Anion (PF_6^-) at -146.1 ppm omitted from spectra.

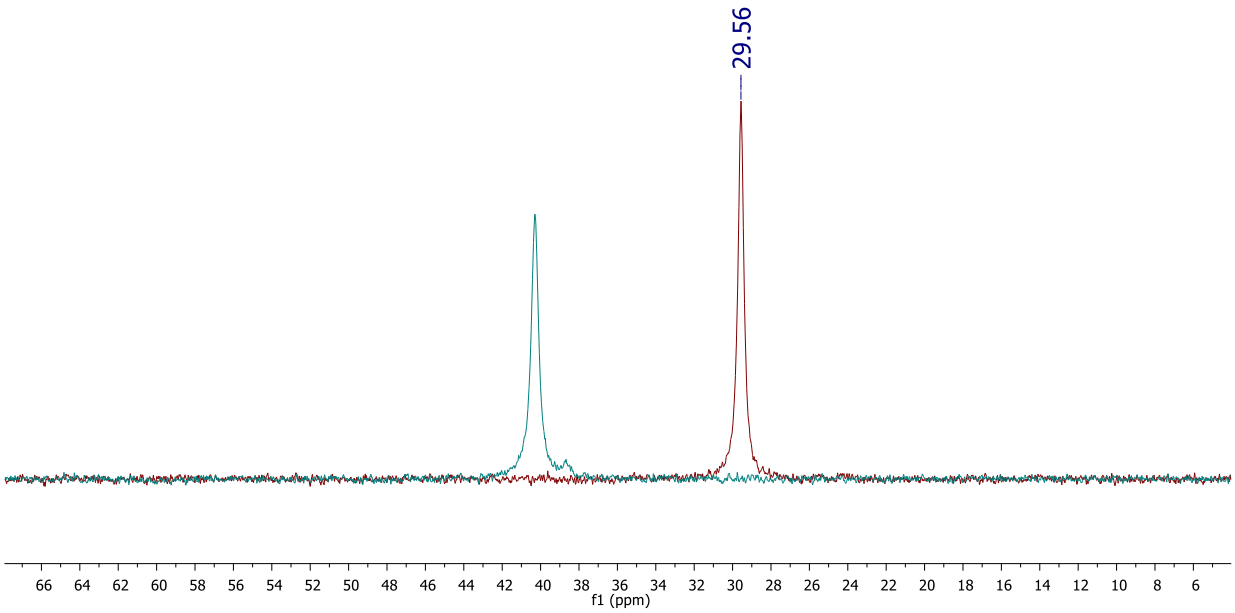

Figure S38. ^{31}P NMR (400 MHz) comparison of resulting mixture of **4** and excess NaI (red trace) and **4** starting material (blue trace, at 40.31 ppm) in CD_2Cl_2.

Experimental conditions: Reaction of **5** and **6** with excess NaN_3

The crude reaction mixture of **5** and **6** (0.054 g, 0.029 mmol based on MW of **6**) was dissolved in THF (approximately 2 mL) and pipette filtered through Celite. A solution of NaN_3 (0.0201 g, 0.309 mmol) in MeOH (approximately 1 mL) was added dropwise with stirring at room temperature. Solution continued stirring overnight at room temperature and the resulting solution appeared as the same color, pale yellow and cloudy. Solution was pipette filtered through Celite and completely evaporated.

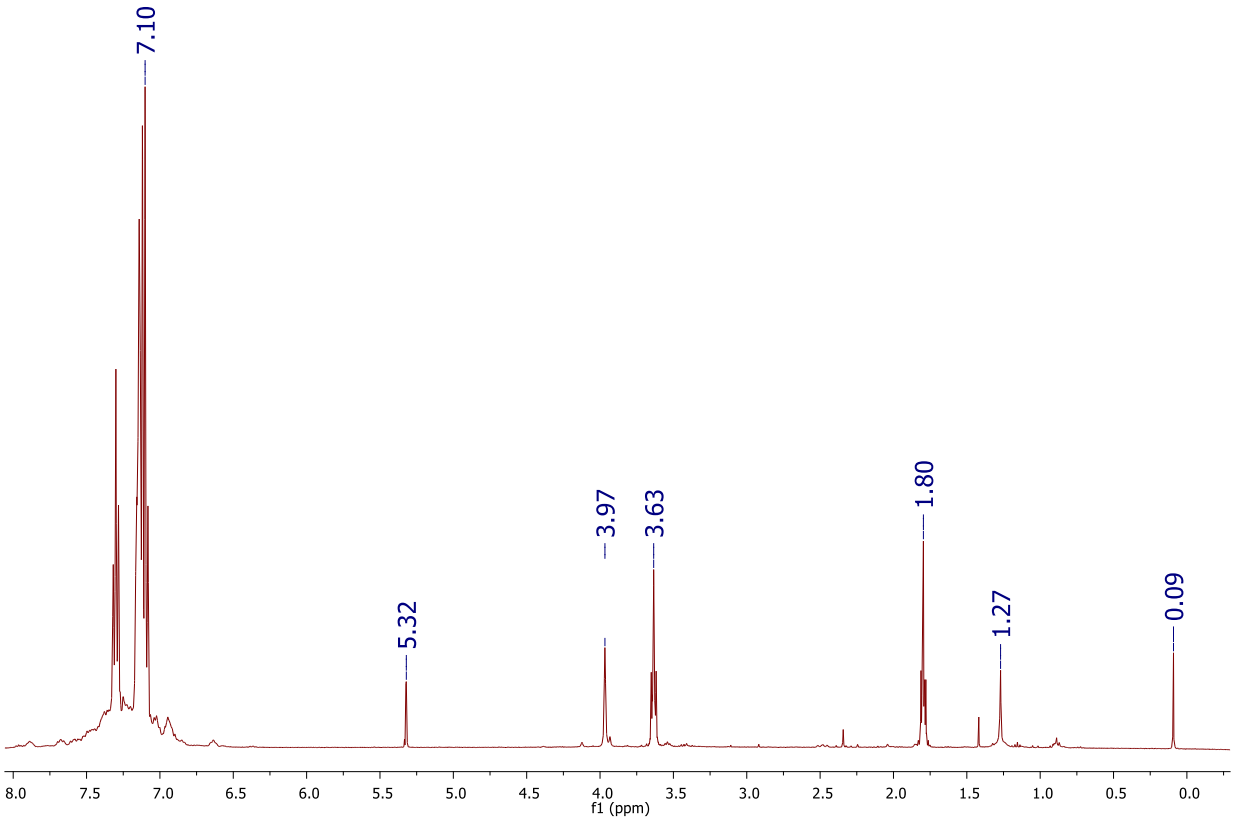

Figure S39. ^{1}H NMR (400 MHz) of resulting mixture of **5** and **6** with excess NaN_3 in CD_2Cl_2.

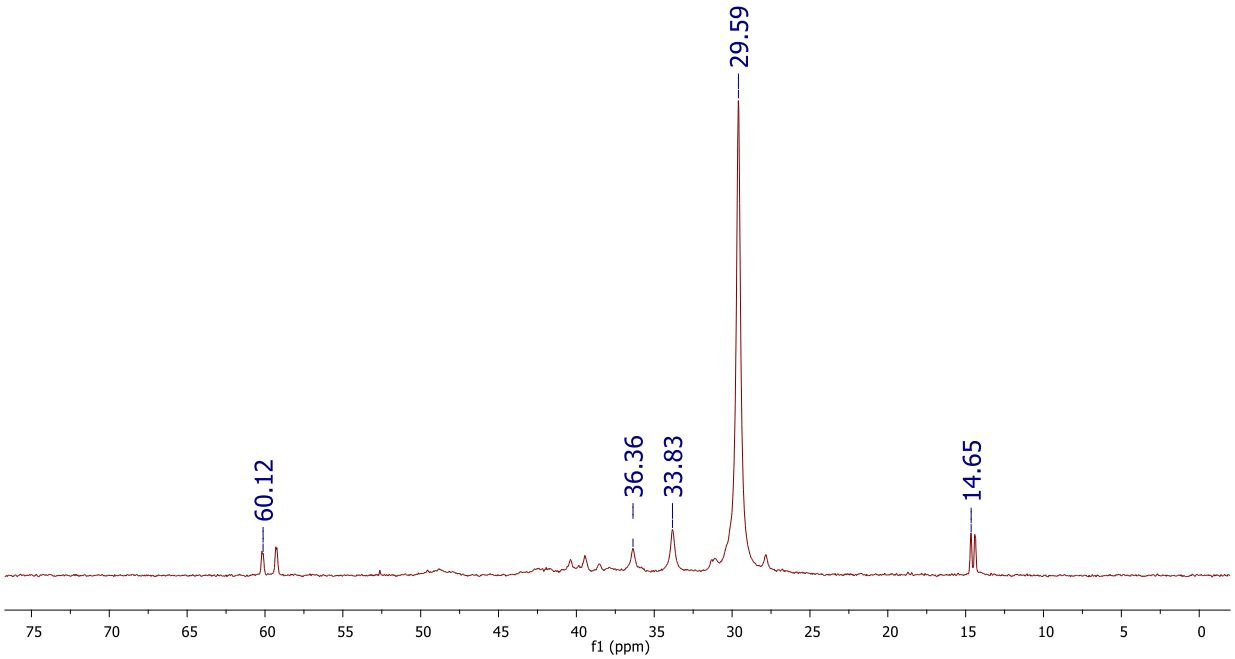

Figure S40. ^{31}P NMR (400 MHz) of resulting mixture of **5** and **6** with excess NaN_3 in CD_2Cl_2. Anion (PF_6^-) at -146.1 ppm omitted from spectra.

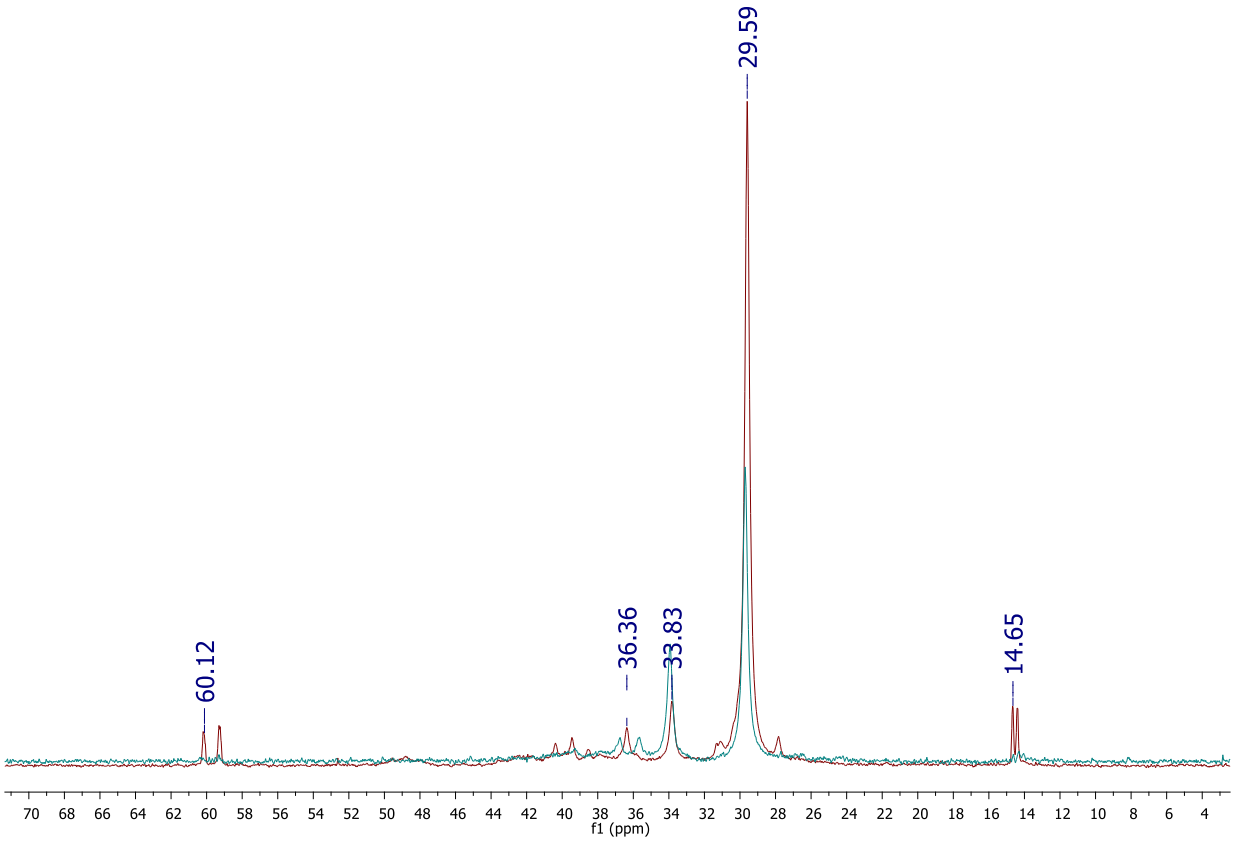

Figure S41. ^{31}P NMR (400 MHz) comparison of resulting mixture of **5** and **6** with excess NaN_3 (red trace) and **5** and **6** starting material (blue trace) in CD_2Cl_2.

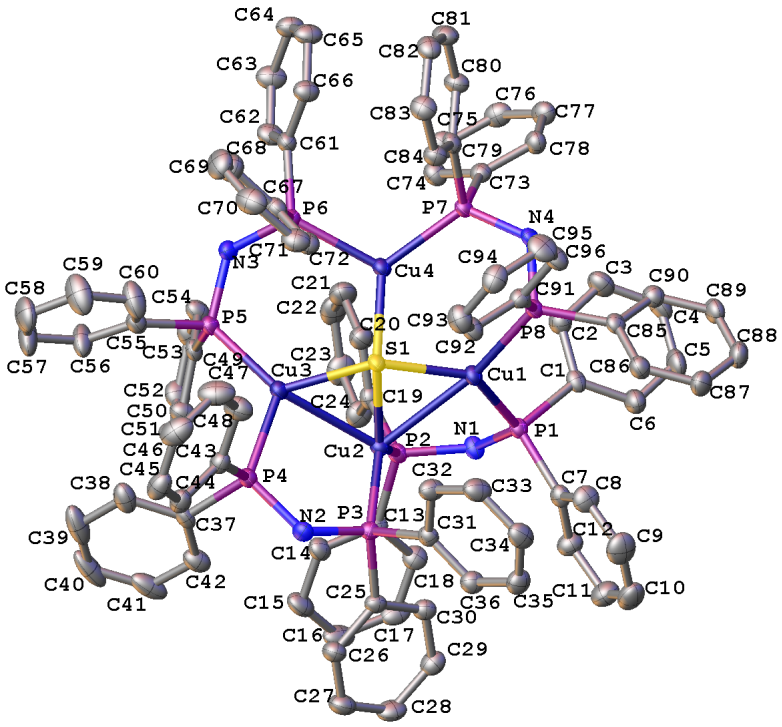

Figure S42. Fully labeled ORTEP of the dicationic unit in complex **2** (50% probability ellipsoids). Solvents, anions, and hydrogen atoms omitted.

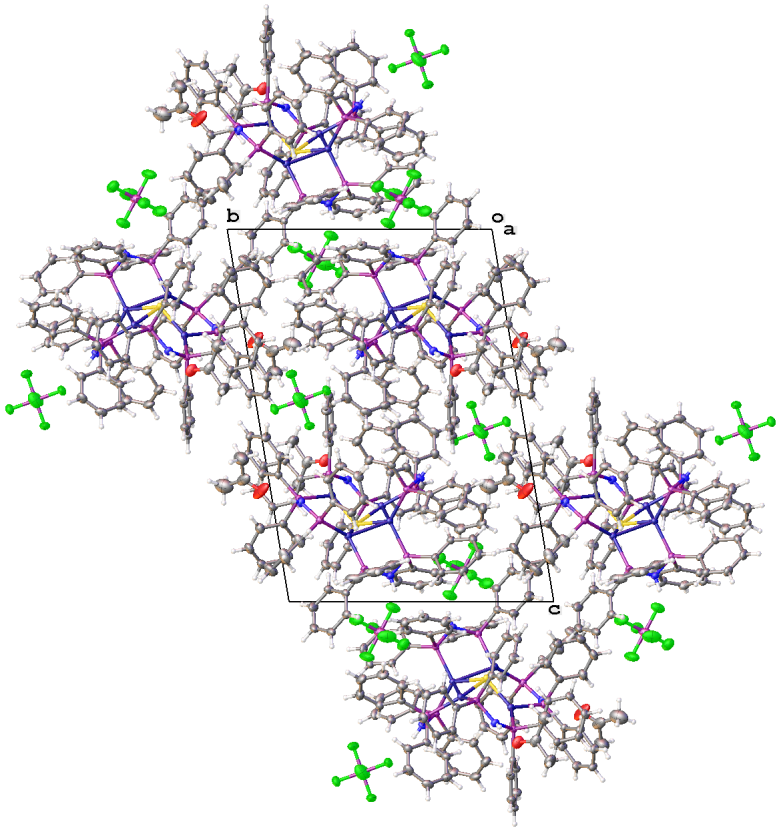

Figure S43. Crystal packing diagram for **2** (50% probability ellipsoids).

Table S6 Crystal data and structure refinement for 2.

Empirical formula	$C_{102}H_{96}Cu_4F_{12}N_4O_2P_{10}S$
Formula weight	2233.75
Temperature/K	99.8(5)
Crystal system	triclinic
Space group	P-1
a/Å	14.9822(4)
b/Å	16.5538(5)
c/Å	21.8707(4)
α/°	96.934(2)
β/°	94.5451(18)
γ/°	112.432(3)
Volume/Å^3	4930.5(2)
Z	2
ρ_{calc}mg/mm^3	1.505
m/mm^{-1}	3.333
F(000)	2284.0
Crystal size/mm^3	0.1933 × 0.0776 × 0.0241
Radiation	CuKα (λ = 1.54184)
2Θ range for data collection	5.86 to 147.48°
Index ranges	$-18 \le h \le 17$, $-20 \le k \le 20$, $-27 \le l \le 19$
Reflections collected	46350
Independent reflections	19350 [R_{int} = 0.0339, R_{sigma} = 0.0383]
Data/restraints/parameters	19350/0/1236
Goodness-of-fit on F^2	1.026
Final R indexes [I>=2σ (I)]	R_1 = 0.0404, wR_2 = 0.1028
Final R indexes [all data]	R_1 = 0.0488, wR_2 = 0.1096
Largest diff. peak/hole / e Å^{-3}	1.02/-0.67

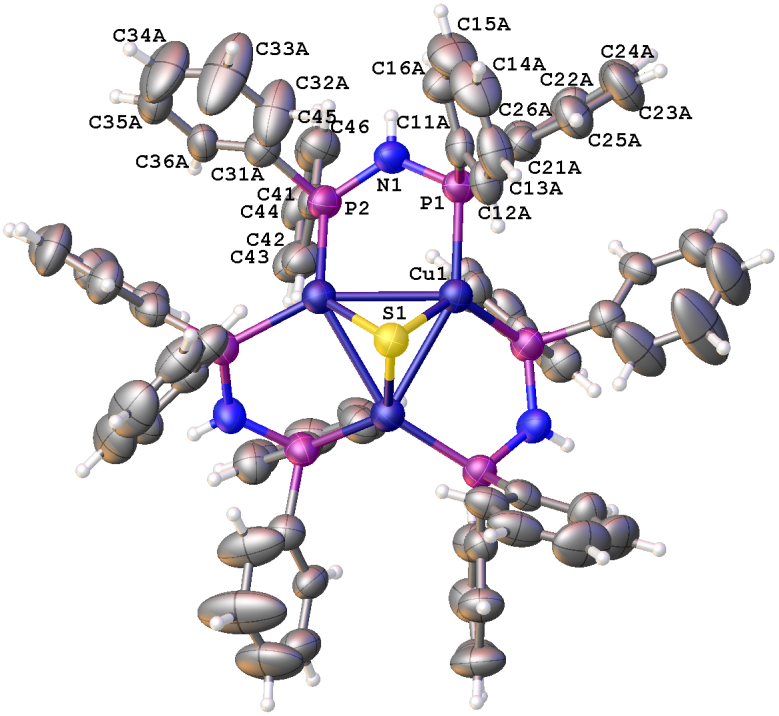

Figure S44. Fully labeled ORTEP of the cationic unit in complex **2'** (50% probability ellipsoids). The cation is positioned on a crystallographic 3-fold axis of symmetry. The solvent/anion region was extremely disordered and was modeled using a solvent-mask procedure to account for its contribution to structural factors.

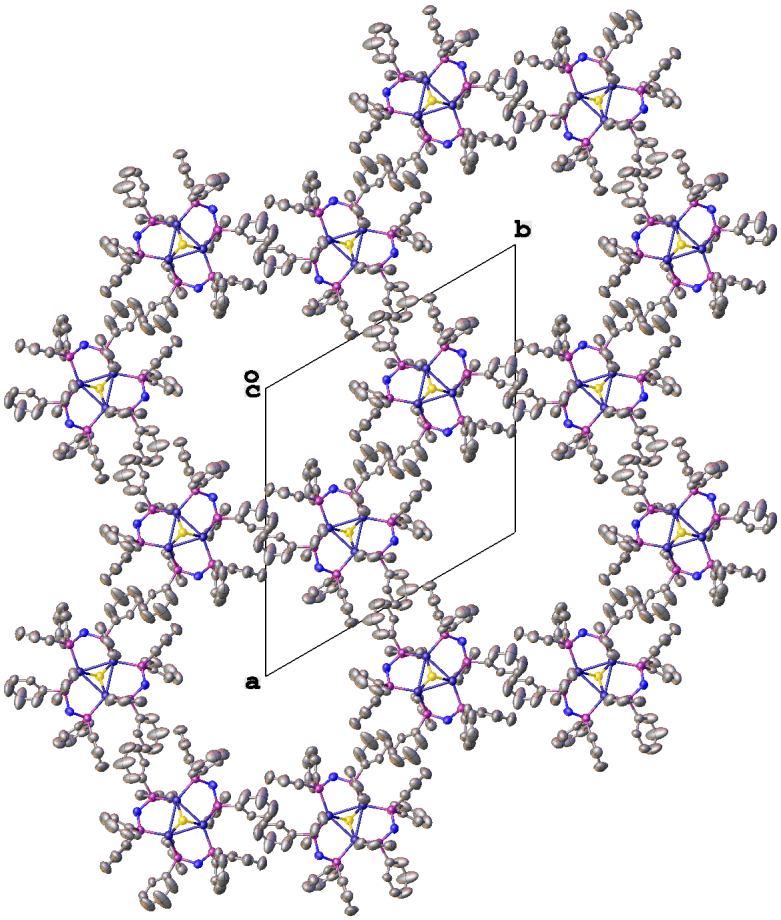

Figure S45. Crystal packing diagram for **2'** (50% probability ellipsoids). The spacious channels along the 3-fold axis contain solvent/anion electron density modeled using a solvent-mask procedure.

Table S7 Crystal data and structure refinement for 2'

Empirical formula	$C_{72}H_{63}Cu_3N_3P_6S$
Formula weight	1378.75
Temperature/K	100.00(10)
Crystal system	trigonal
Space group	P-3
a/Å	22.6945(7)
b/Å	22.6945(7)
c/Å	9.9881(5)
α/°	90.00
β/°	90.00
γ/°	120.00
Volume/Å^3	4455.1(3)
Z	2
ρ_{calc}mg/mm^3	1.028
m/mm^{-1}	2.321
F(000)	1418.0
Crystal size/mm^3	0.7300 × 0.0498 × 0.0379
Radiation	Cu Kα (λ = 1.5418)
2Θ range for data collection	7.8 to 147.22°
Index ranges	$-27 \leq h \leq 28$, $-27 \leq k \leq 28$, $-10 \leq l \leq 11$
Reflections collected	28120
Independent reflections	5901[R(int) = 0.0556]
Data/restraints/parameters	5901/270/310
Goodness-of-fit on F^2	1.055
Final R indexes [I>=2σ (I)]	R_1 = 0.0773, wR_2 = 0.2178
Final R indexes [all data]	R_1 = 0.0876, wR_2 = 0.2253
Largest diff. peak/hole / e Å^{-3}	0.75/-0.70

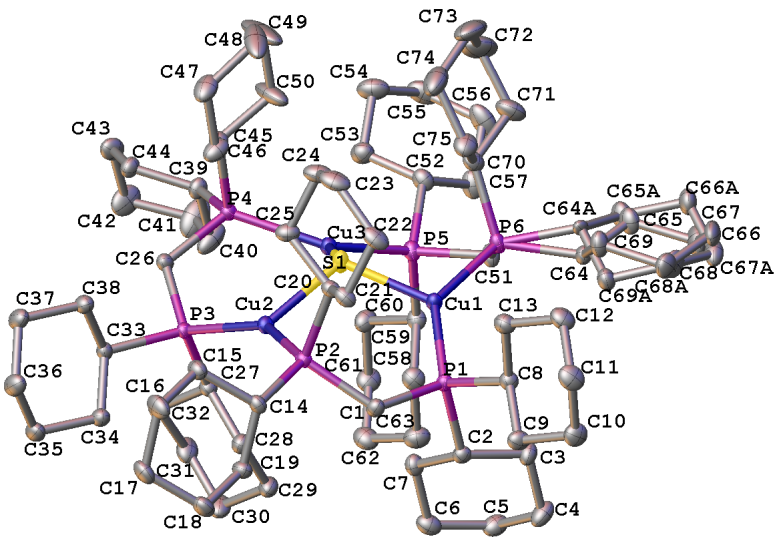

Figure S46. Fully labeled ORTEP of the cationic unit in complex **3** (50% probability ellipsoids). Solvents, anions, and hydrogen atoms omitted. One of the cyclohexyl groups is disordered in a 3:1 ratio.

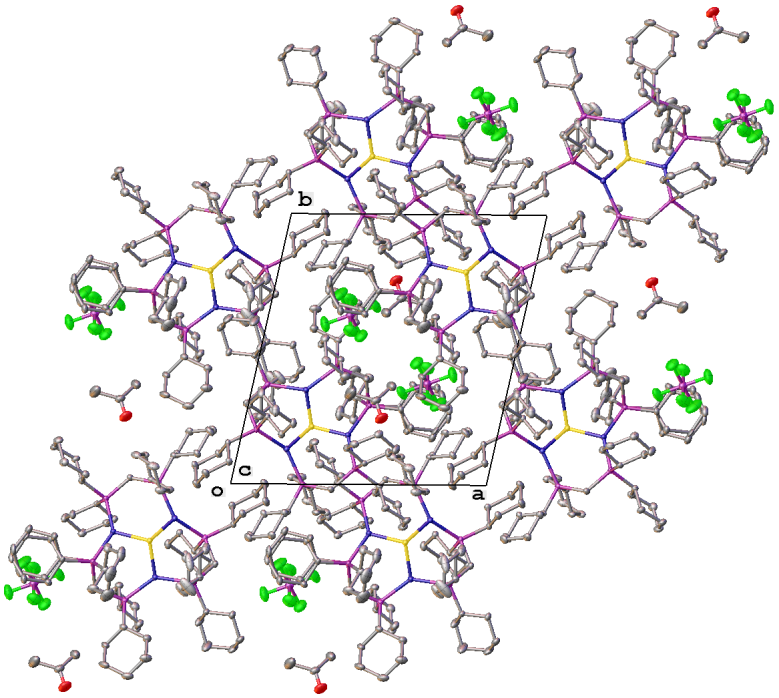

Figure S47. Crystal packing diagram for **3** (50% probability ellipsoids). Whereas the PF_6^- anion and one equivalent of acetone were localized, the structure contains relatively small (261.5 $Å^3$) centrosymmetric cavities apparently containing disordered Et_2O molecules. However, the complex distribution of electron density suggests a presence of some other solvents. Therefore, a solvent-mask procedure was applied to account for the contributions of this relatively minor but highly disordered and mixed area into the structural factors.

Table S8 Crystal data and structure refinement for 3.

Empirical formula	$C_{78}H_{144}Cu_3F_6OP_7S$
Formula weight	1651.40
Temperature/K	100.00(10)
Crystal system	triclinic
Space group	P-1
a/Å	14.7920(3)
b/Å	16.0721(4)
c/Å	18.7434(4)
α/°	83.8839(17)
β/°	86.2996(15)
γ/°	77.4184(17)
Volume/Å^3	4320.34(15)
Z	2
ρ_{calc}mg/mm^3	1.269
m/mm^{-1}	2.728
F(000)	1764.0
Crystal size/mm^3	0.1891 × 0.1305 × 0.1121
Radiation	CuKα (λ = 1.54184)
2Θ range for data collection	5.66 to 147.42°
Index ranges	$-18 \leq h \leq 18$, $-19 \leq k \leq 19$, $-22 \leq l \leq 23$
Reflections collected	80468
Independent reflections	17149 [R_{int} = 0.0269, R_{sigma} = 0.0169]
Data/restraints/parameters	17149/36/916
Goodness-of-fit on F^2	1.056
Final R indexes [I>=2σ (I)]	R_1 = 0.0280, wR_2 = 0.0734
Final R indexes [all data]	R_1 = 0.0302, wR_2 = 0.0750
Largest diff. peak/hole / e Å^{-3}	1.08/-0.54

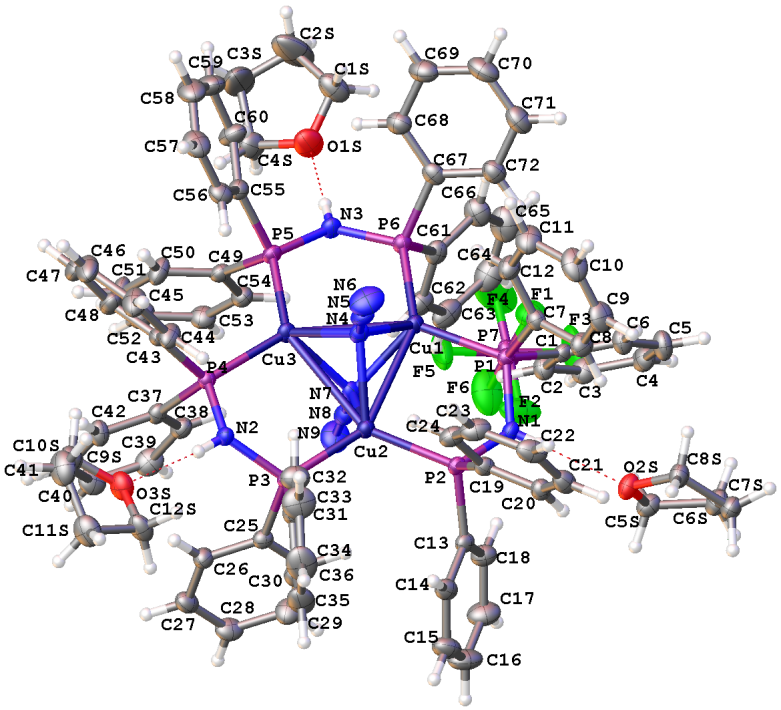

Figure S48. Fully labeled ORTEP of complex **4** (50% probability ellipsoids). There are two symmetrically independent formula units in the crystal (only one shown).

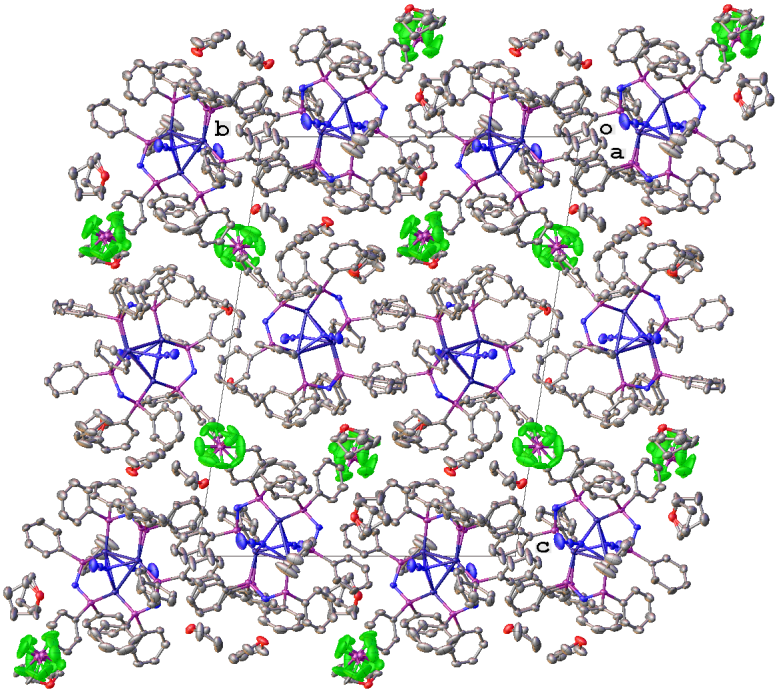

Figure S49. Crystal packing diagram for **4** (50% probability ellipsoids). There are multiple instances of disorder in the structure.

Table S9 Crystal data and structure refinement for 4.

Empirical formula	$C_{84}H_{87}Cu_3F_6N_9O_3P_7$
Formula weight	1792.04
Temperature/K	100.00(10)
Crystal system	triclinic
Space group	P-1
a/Å	13.1050(2)
b/Å	22.7156(3)
c/Å	29.5406(4)
α/°	79.6448(10)
β/°	82.6818(13)
γ/°	75.0872(13)
Volume/Å^3	8328.8(2)
Z	4
ρ_{calc}g/cm^3	1.429
μ/mm^{-1}	2.720
F(000)	3696.0
Crystal size/mm^3	0.4436 × 0.3995 × 0.1324
Radiation	CuKα (λ = 1.54184)
2Θ range for data collection/°	6.1 to 147.58
Index ranges	$-15 \le h \le 16$, $-28 \le k \le 28$, $-36 \le l \le 36$
Reflections collected	156426
Independent reflections	33081 [R_{int} = 0.0487, R_{sigma} = 0.0299]
Data/restraints/parameters	33081/513/2538
Goodness-of-fit on F^2	1.018
Final R indexes [I>=2σ (I)]	R_1 = 0.0423, wR_2 = 0.1062
Final R indexes [all data]	R_1 = 0.0499, wR_2 = 0.1131
Largest diff. peak/hole / e Å^{-3}	0.88/-0.81

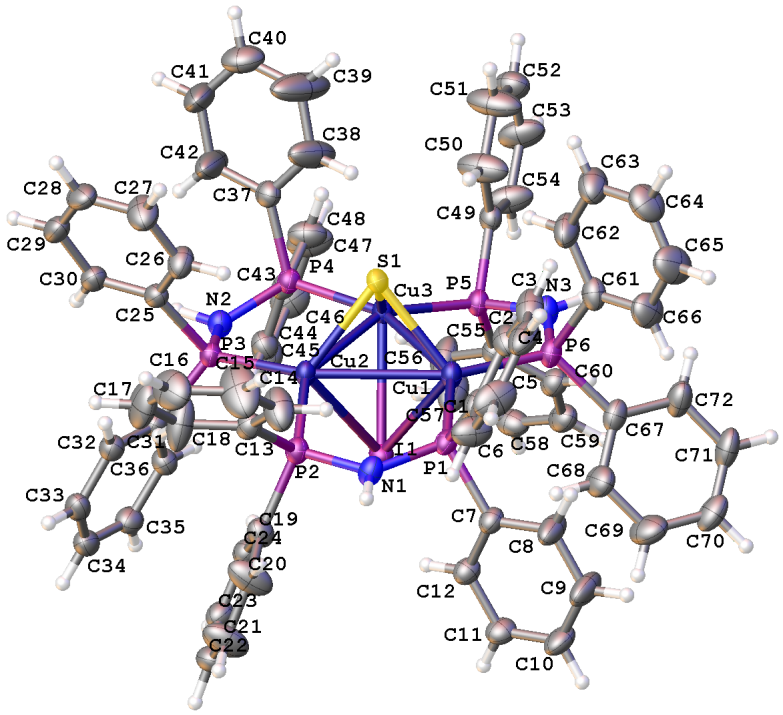

Figure S50. Fully labeled ORTEP of complex **5** (50% probability ellipsoids). It is disordered in a roughly 3:1 ratio with the outside ligand scaffold in place and I and S ligand changing places. The alternative positions of I and S practically coincide and only the Cu triangle position shifts along I…S axis.

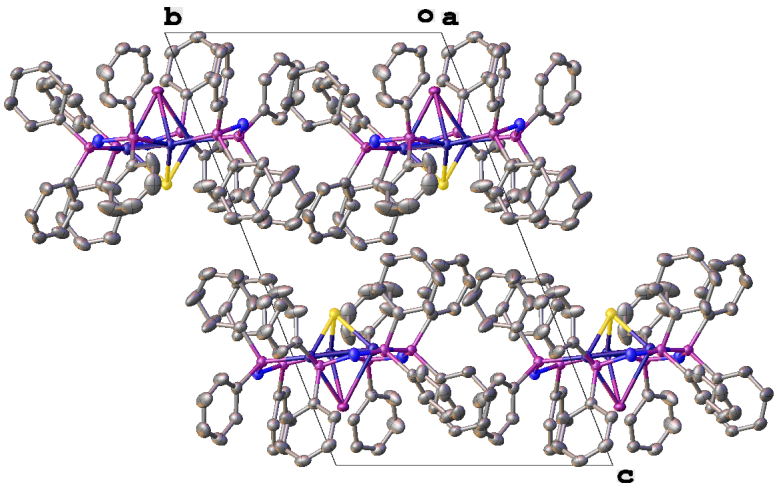

Figure S51. Crystal packing diagram for **5** (50% probability ellipsoids).

Table S10 Crystal data and structure refinement for 5.

Empirical formula	$C_{72}H_{63}Cu_3IN_3P_6S$
Formula weight	1505.65
Temperature/K	100.00(10)
Crystal system	triclinic
Space group	P-1
a/Å	13.7161(3)
b/Å	13.9702(4)
c/Å	20.5980(5)
α/°	108.460(2)
β/°	90.8367(19)
γ/°	118.571(3)
Volume/Å^3	3221.94(14)
Z	2
ρ_{calc}mg/mm^3	1.552
m/mm^{-1}	6.977
F(000)	1524.0
Crystal size/mm^3	0.5342 × 0.2676 × 0.128
Radiation	CuKα (λ = 1.54184)
2Θ range for data collection	7.42 to 147.54°
Index ranges	-16 ≤ h ≤ 16, -17 ≤ k ≤ 17, -25 ≤ l ≤ 25
Reflections collected	47311
Independent reflections	12805 [R_{int} = 0.0412, R_{sigma} = 0.0317]
Data/restraints/parameters	12805/10/816
Goodness-of-fit on F^2	1.083
Final R indexes [I>=2σ (I)]	R_1 = 0.0447, wR_2 = 0.1148
Final R indexes [all data]	R_1 = 0.0476, wR_2 = 0.1168
Largest diff. peak/hole / e Å^{-3}	1.27/-0.69

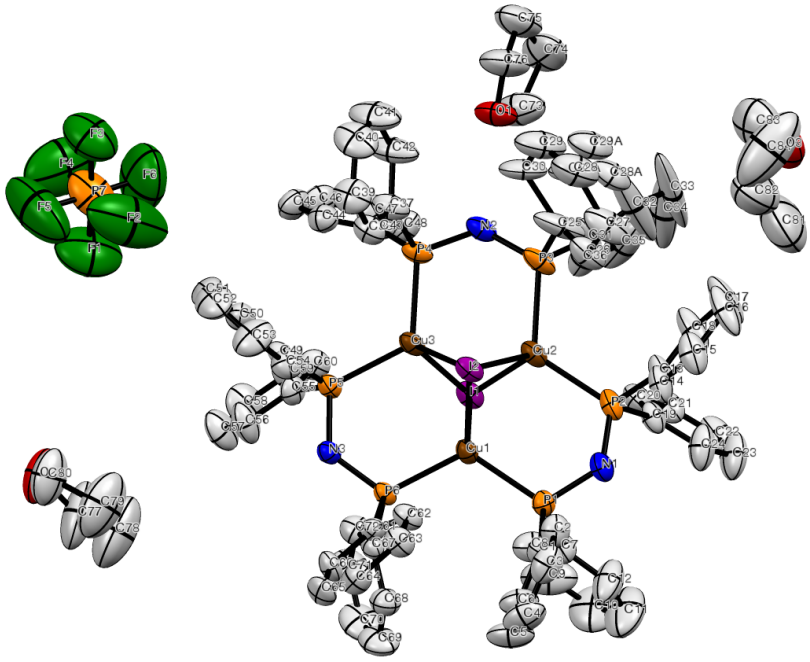

Figure S52. Fully labeled ORTEP of complex **6** (50% probability ellipsoids). Hydrogen atoms have been omitted for clarity.

Table 11. Crystal data and structure refinement for 6.

Empirical formula	C84 H82 Cu3 F6 I2 N3 O6 P7 S0	
Formula weight	2004.73 g/mol	
Temperature	200(2) K	
Wavelength	0.71073 Å	
Crystal system	Triclinic	
Space group	P -1	
Unit cell dimensions	a = 13.0898(6) Å	
	b = 18.5702(10) Å	α = 107.3385(16)°
	c = 19.7003(10) Å	β = 101.4419(15)°
Volume	4376.0(4) $Å^3$	γ = 98.1390(16)°
Z	2	
Density (calculated)	1.521 g/cm^3	
Absorption coefficient	1.620 mm^{-1}	
F(000)	2014	
Crystal size	0.07 x 0.21 x 0.51 mm^3	
Theta range for data collection	1.12 to 26.37°	
Index ranges	-16<=h<=12, -23<=k<=23, -24<=l<=24	
Reflections collected	59232	
Independent reflections	17542 [R(int) = 0.0658]	
Completeness to theta = 26.37°	97.9%	
Absorption correction	Multiscan	
Max. and min. transmission	0.8950 and 0.4920	
Refinement method	Full-matrix least-squares on F^2	
Data / restraints / parameters	17542 / 308 / 1003	
Goodness-of-fit on F^2	1.004	
Final R indices [I>2sigma(I)]	R1 = 0.0511, wR2 = 0.1359	
R indices (all data)	R1 = 0.1045, wR2 = 0.1733	
Largest diff. peak and hole	1.653 and -1.197	

References:

[1] Magennis, S. W.; Parsons, S.; Pikramenou, Z. *Chem. Eur. J.* **2002**, *8,* 5761-5771.

[2] Liu, H.; Clhorda, M. J.; Drew, M. G. B.; Felix, V.; Novosad, J.; Veiros, L. F.; de Biani, F. F.; Zanello, P. *J. Chem. Soc., Dalton Trans.* **2002,** 4365-4374.

[3] Che, C.; Mao, Z.; Miskowski, V. M.; Tse, M. C.; Chan, C. K.; Cheung, K. K.; Phillips, D. L.; Leung, K. H. *Angew. Chem. Int. Ed.* **2000**, *39,* 4084-4088.